

MULTI-SCALE SIMULATIONS OF NON-EQUILIBRIUM AND NON-LOCAL
THERMAL TRANSPORT

A Dissertation

Submitted to the Faculty

of

Purdue University

by

Zexi Lu

In Partial Fulfillment of the

Requirements for the Degree

of

Doctor of Philosophy

December 2018

Purdue University

West Lafayette, Indiana

THE PURDUE UNIVERSITY GRADUATE SCHOOL
STATEMENT OF DISSERTATION APPROVAL

Dr. Xiulin Ruan, Chair

School of Mechanical Engineering

Dr. Gerhard Klimeck

School of Electrical and Computer Engineering

Dr. Liang Pan

School of Mechanical Engineering

Dr. Ajit K. Roy

Air Force Research Laboratory

Approved by:

Dr. Jay P. Gore

Head of the School Graduate Program

ACKNOWLEDGMENTS

I would like to thank my adviser Prof. Xiulin Ruan for his guidance, advice, patience, knowledge and insight. He guides and helps me grow as a PhD student and as a researcher. He has led me into the world of thinking and helped me overcome obstacles to find my interested topic to which I can devote my efforts. Other than that, Prof. Ruan is also a life mentor. I have learned more than just research during my PhD career. Without him I can hardly imagine all that I have achieved so far.

I am very grateful to Dr. Yan Wang, who has graduated from our group and is currently an assistant professor in University of Nevada, Reno. We are both from Tsinghua University in Beijing, and also the exact same department. As a senior student to me, Yan provided advice and guidance to help me get on the right track of research when I first came here. I have also been learning a lot from him through our collaboration during these years. I also want to thank Prof. Liang Pan for the fruitful discussions we had on electron-phonon coupling, as well as the insightful advice I received when I was working as a teaching assistant for the course Heat and Mass Transfer. I also want to thank Prof. Gerhard Klimeck, Prof. Liang Pan and Dr. Ajit K. Roy for serving in my advisory committee despite busy schedule.

I came to the US in 2012, and became a member of the Nanoscale Energy Transport and Conversion Laboratory. I have been at Purdue for more than 5 years, and I am very thankful for having friends like Tianli Feng and Jingjing Shi. I have learned a lot from them from our discussions on topics such as phonon scattering and interfacial thermal transport. I am also grateful to Tianli's advice and help during my pursuing of a postdoctoral career. I also want to thank all the group members of Nanoscale Energy Transport and Conversion Laboratory. I have had useful discussions about research and received a lot of help from them. The lab is home to me here and all of them are my family.

I want to thank my dear parents. They gave life to me and have been supporting me ever since. When I was doing something within their reach, they guided me and helped me grow into a qualified student who was admitted into the best university in China. Now I am doing something they cannot give me advice anymore, and they have been giving me support, freedom and all I need to grow into an independent person. Yet they never stop giving me advice as my life-long mentors. Their wisdom has been a indispensable part of my life. I also want to thank my cousin and his family who has been providing support for me since I came to the US.

I acknowledge the Ross fellowship from Purdue University. This work is partially supported by the Air Force Office of Scientific Research (AFOSR), Defense Advanced Research Projects Agency (DARPA) and National Natural Science Foundation of China (NSFC).

TABLE OF CONTENTS

	Page
LIST OF TABLES	viii
LIST OF FIGURES	ix
ABSTRACT	xiv
1. INTRODUCTION	1
1.1 Motivation	1
1.2 A quick review of non-equilibrium and non-local thermal transport	2
1.2.1 Thermal non-equilibrium at interfaces between different materials	7
1.2.2 Electron-phonon and phonon-phonon non-equilibrium in materials under irradiation	15
1.2.3 Non-local thermal transport at metal-dielectric interfaces	17
1.3 Methodology	19
1.3.1 Molecular dynamics	19
1.3.2 Boltzmann transport equation and the gray lattice Boltzmann method	21
1.3.3 First-principles method based on density functional theory	23
1.4 Objectives and Scope of Thesis	24
2. MOLECULAR DYNAMICS STUDY OF AU-SAM INTERFACES	27
2.1 Introduction	27
2.2 Classical molecular dynamics simulation	28
2.2.1 Simulation details	28
2.2.2 Results	31
2.3 Two-temperature molecular dynamics simulation	31
3. INVESTIGATION OF THERMAL TRANSPORT IN METAL THIN FILMS BASED ON TWO-TEMPERATURE MODEL	34
3.1 Introduction	34
3.2 Theory	36
3.2.1 A general solution to two-temperature model equations for a metal thin film sandwiched between two dielectrics	38
3.2.2 The critical thickness L_c	40
3.2.3 Two-temperature lattice Boltzmann method	42
3.3 SAM-Au-SAM Case Study	43
3.3.1 Two-temperature molecular dynamics simulations	44
3.3.2 Two-temperature model Fourier calculations	46

	Page
3.3.3 Two-temperature model Boltzmann transport equation calculations	49
3.4 Discussion	51
3.4.1 Factors affecting L_c	51
3.4.2 The effective thermal conductivity of the sandwiched metal layer	53
3.4.3 Temperature discontinuity at the interface	57
3.5 Conclusions	62
4. TWO-TEMPERATURE MOLECULAR DYNAMICS SIMULATION OF METAL-DIELECTRIC INTERFACES WITH NON-LOCAL ELECTRON-PHONON COUPLING	63
4.1 Introduction	63
4.2 Theory	65
4.2.1 A preliminary model for non-local electron-phonon coupling	65
4.2.2 Implementation in two-temperature molecular dynamics	69
4.3 Cu-Si case study and results	71
4.3.1 Simulation system	71
4.3.2 Input parameter	74
4.3.3 Results	76
4.4 Thermal circuit analysis	80
4.4.1 Thermal circuit based on our models	80
4.4.2 Merits and drawbacks of the original model of Huberman and Overhauser	81
4.5 Conclusions	83
5. FIRST-PRINCIPLES CALCULATIONS OF ELECTRON-PHONON COUPLING PROPERTIES IN PURE METALS	85
5.1 Introduction	85
5.2 Theory	85
5.3 Cu case study	86
6. NON-LOCAL ELECTRON-PHONON COUPLING IN PURE METALS MANIFESTED BY SIZE EFFECT BASED ON FIRST-PRINCIPLES CALCULATIONS	90
6.1 Introduction	90
6.2 Case study of Al: size effect of electron-phonon coupling manifested	91
6.3 Theory	97
6.3.1 The partial coupling strength	98
6.4 Results: the non-local electron-phonon coupling properties in Al	99
6.5 Case study of Cu and Ag	104
6.6 Conclusions	110
7. MULTI-TEMPERATURE MODEL SIMULATION OF NON-EQUILIBRIUM THERMAL TRANSPORT	111

	Page
7.1 Introduction	111
7.2 Theory: Multi-temperature model with electron-phonon coupling . .	113
7.3 Case study: thermal transport in laser-irradiated single-layer graphene	113
7.3.1 Simulation domain and input parameters	114
7.3.2 Results: transient and steady-state temperature profile	116
7.4 Discussions	118
7.4.1 The apparent lattice temperature and degree of non-equilibrium	118
7.4.2 A comparison with the original two-temperature model	122
7.5 Conclusions	124
8. MULTI-TEMPERATURE MODEL SIMULATION OF NON-EQUILIBRIUM THERMAL TRANSPORT AT INTERFACES	127
8.1 Introduction	127
8.2 Case study: thermal transport across Si-Ge interfaces	128
8.3 Conclusions	135
9. SUMMARY	136
9.1 Conclusions	136
9.1.1 Investigation of non-equilibrium thermal transport in metal thin films based on two-temperature model	136
9.1.2 Two-temperature molecular dynamics simulation of metal-dielectric interfaces with non-local electron-phonon coupling	138
9.1.3 Non-local electron-phonon coupling in pure metals manifested by size effect based on first-principles calculations	139
9.1.4 Multi-temperature model simulation of non-equilibrium phonon transport in metals and across interfaces	141
9.2 Future works	143
REFERENCES	146
VITA	160

LIST OF TABLES

Table	Page
2.1 ITC at Au/SAM junction with different molecule lengths	31
3.1 Thermal Properties used in TTM-Fourier Calculation	46
3.2 Thermal Properties used in the TTM-BTE calculation	50
4.1 Important input thermal properties for the TTM-MD calculation	74
4.2 Results of TBR from different MD simulations	76
4.3 Results of decomposed TBR in different models (values are in unit of $\text{m}^2\text{K}/\text{W}$)	81
6.1 Details of the inputs for the DFT calculations for the bulk cases	93
6.2 Details of the inputs for the DFT calculations for the 1-layer cases	94
6.3 Reduction factor of $\alpha_{v,norm}^2$ of phonon branch 11 and 12 in Al	99
6.4 A summary of the results of e-p coupling in Al, Cu and Ag	108
6.5 Non-local e-p coupling properties of Cu and Ag	110
7.1 Thermal Properties of SLG at 297 K	115
7.2 Ratio of G_{ep}/k and k/G_{ep} of SLG at 297 K	121
8.1 Thermal Properties of Si at 297 K	131
8.2 Thermal Properties of Ge at 297 K	132
8.3 ITC from AMM calculations	132

LIST OF FIGURES

Figure	Page
1.1 Illustration of the ultrafast laser heating and hot electron cooling processes in aluminum in Ref. 6. The temperature profiles are predicted from calculations with fitted parameters matching the experimental data. The 3 different phonon branches have different temperature due to their different coupling strength to the electrons.	4
1.2 Illustration of hot electron cooling process under different laser intensity measured in experiment compared with TTM predictions in Ref. 28. Symbols represent the experimental electron temperature cooling curve while the dash line represents the TTM prediction. n_0 denotes the incoming photon density determined from laser power. It is clearly seen that the actual cooling rate is much slower than prediction at high power laser input. 6	6
1.3 Illustration of e-p non-equilibrium near a metal-dielectric interface derived from TTM in Ref. 31. Electrons are insulated from entering the non-metal therefore have a flat curve near the interface. Their energy is dumped to phonons and transferred to the other side. The e-p non-equilibrium results in an additional TBR in series with the p-p TBR.	10
1.4 Illustration of phonon thermal non-equilibrium induced by different transmission at an SLG-BN interface from Ref. 61.	12
1.5 MTM prediction of the resolved temperature profiles showing e-p and p-p non-equilibrium induced by selective e-p coupling during a Raman spectroscopy experiment Ref. 7.	18
2.1 Visualization of the Au-SAM-Au-SAM-Au unit cell used in the NEMD simulation.	29
2.2 Temperature profile of the SAM-Au-SAM sandwich system in the MD simulation. The linear part of the profiles in each material is extrapolated to the interface to calculate the temperature jump.	30
2.3 Temperature profile of the SAM-Au-SAM sandwich system in the TTM-MD simulation.	33
3.1 The schematic of a 1D metal-polymer composite, where a polymer layer is replaced with metal. Hence, the middle layer polymer conduction resistance is replaced by metal layer conduction resistance and the thermal boundary resistance at the two interfaces.	37

Figure	Page
3.2 Temperature distribution in a polymer-metal-polymer sandwich system. In the metal middle layer both electrons and phonons are considered while in the polymer substrates only phonons are considered.	39
3.3 The temperature profile of the Au-SAM-Au-SAM-Au multiplayer system zoomed at the middle layer from the TTM-MD simulation.	45
3.4 R_{intro} , $R_{poly,c}$ and ΔR as a function of the metal layer thickness in the SAM-Au-SAM sandwich system predicted by TTM-Fourier calculation. . .	47
3.5 Temperature profile of a SAM-Au (10.8nm)-SAM sandwich system predicted by TTM-Fourier calculation. A zoom in profile of the electron temperature is shown.	48
3.6 Components of the total resistance of the gold film. It is composed of three parts: 1) film conduction resistance $R_{metal,c}$ 2) resistance due to interfacial phonon coupling R_{pp} 3) resistance due to e-p non-equilibrium near the interface R_{ep} . It is revealed that $R_{metal,c}$ comprises a very small part. The majority of the resistance comes from R_{pp} and R_{ep}	49
3.7 Temperature profile of a SAM-Au (10.8 nm)-SAM sandwich system predicted by TTM-BTE calculation. Calculation is conducted to match the heat flux used in TTM-Fourier calculation. A zoom in profile of the electron temperature is shown. The resulting temperature profile matches that of TTM-Fourier calculation.	52
3.8 Two main factors that can affect the critical thickness L_c : G_{ep} and k_e . It is revealed that G_{ep} has a significant effect on L_c . L_c is sensitive to k_e as k_e is small (small r_{ep}) while it becomes insensitive as k_e becomes large. . .	54
3.9 A new thermal circuit for a sandwiched metal thin film where R_{ep} is lumped into R_{eff}	56
3.10 a) k_{eff} v.s. L for gold when L is within the e-p cooling length, which is 45 nm for gold. b) k_{eff} v.s. L for gold when L over a large range of thickness. k_{eff} eventually converges to its saturated value of $k_e + k_p$	58
3.11 Temperature distribution in a single material thin film with different thickness. The temperatures at the two thermal reservoirs are constant. At the boundaries the temperature jump can be clearly observed, which agrees with previous works [90, 124, 134].	61
4.1 The four regions defined at the metal-nonmetal interface in our analysis. Region A is the bulk metal region, while Region B and C are the interfacial regions, and Region D is the bulk nonmetal region.	66

Figure	Page	
4.2	Illustration of the non-local coupling mechanism. The system is discretized into grids using FVM. λ_{avg} is the average wavelength of phonons in the material. Each electron can couple to phonons in a region up to the length of $2\lambda_{avg}$. The upper figure also shows the coupling range of three different electrons: one in the center of the grid, and the other two near the boundary of the grid. The lower figure shows the effective coupling strength of electrons in the central grid to phonons from all the grids. G_{ep} is larger in the electrons' own grid, while smaller in the adjacent grids, and becomes zero in grids which are beyond the coupling range of any electron.	70
4.3	Illustration of the simulation system. Black parts refer to the fixed ends where atoms have no velocities. The red and blue parts are the heat source and heat sink respectively. Heat flows in the direction perpendicular to the interface which results in 1D conduction. The periodic boundary condition is applied in the other two directions.	72
4.4	a) Temperature profile from a TT-MD simulation on the Cu-Si system with non-local e-p coupling using the joint-modes model. The fitted temperature is acquired by extrapolation. It can be observed that the fitted temperature is almost identical to electrons' temperature since electrons have a much higher effective thermal conductivity. b) Temperature profile from the phonon wavelength model. Overall the result is not much different from that of the joint-modes model.	77
4.5	a) b) Qualitative temperature profile of our model and the corresponding thermal circuit. c) d) Qualitative temperature profile of Overhauser's model and the corresponding thermal circuit. $R_{ep,tot}$ is the resistance due to e-p non-equilibrium, R_{pp} is the resistance due to p-p cross-interface coupling, and R_{ei} represents the channel of cross-interface e-p coupling.	79
5.1	Eliashberg function of bulk Cu. The result agrees with previous literature.	87
5.2	The accumulation of G_{ep} with phonon frequency in bulk Cu.	88
5.3	The normalized G_{ep} over the phonon DOS. Generally the coupling is stronger as the phonon frequency gets higher.	89

Figure	Page
6.1 a) Local e-p coupling in bulk metal where $G'_{ep}(x)$ is delta functions at the positions of each overlapping electron and phonon. b) Local e-p coupling in a metal thin film where the overall G_{ep} is the same with the bulk. c) Non-local e-p coupling in bulk metal where $G'_{ep}(x)$ has a spatial distribution. d) Non-local e-p coupling in a metal thin film where $G'_{ep}(x)$ is truncated at the boundaries and the overall G_{ep} is smaller than the bulk. e) Non-local e-p coupling at a metal-dielectric interface where metal electrons can couple to dielectric nuclei within their coupling distance. Note $G'_{ep}(x)$'s curve may change in the dielectric.	93
6.2 The phonon dispersion of bulk and 1-layer Al. There are 4 atoms in one "primitive cell" so there are altogether 12 phonon branches. Most of the low frequency phonons have frequency shifts and different frequency spans in these two cases, while the high frequency branches are much more similar, especially along the Γ -X line.	95
6.3 The Eliashberg function of bulk and 1-layer Al. Due to the changes in phonon dispersion, the shapes of the function curves are significantly different. The overall coupling factors are similar while the electron DOS deviates, indicating that the actual coupling strengths are different in these two cases.	96
6.4 $\alpha_{v,norm}^2$ phonon branch 11 and 12 in bulk and 1-layer Al. The two optical phonon branches have similar frequency spans and shapes of curve. . . .	100
6.5 The actual coupling range of one electron in 1-layer Al. The distribution is cut off at the "effective boundary" of the material.	102
6.6 CSDF in Al. The standard deviation of the Gaussian function is 0.28 nm. The shaded area represents the truncated CSDF of a electron located in the center of 1-layer Al.	103
6.7 The phonon dispersion of bulk and 1-layer Ag. Different from the Al case, the phonon dispersion have changed significantly. Even the high frequency phonons don not have excellent overlap along the Γ -X line. It is also worth noting that results of the low frequency phonon branches near the [110] point is not very reliable, but this does not affect our result because we are only using the high frequency phonon branches for calculation. . . .	105
6.8 The phonon dispersion of bulk and 1-layer Cu. The physical significance is similar with the Ag case.	106
6.9 $\alpha_{v,norm}^2$ of Branch 11 and 12 in Ag and Cu. The non-local e-p coupling is less significant than in Al, and the peak value of $\alpha_{v,norm}^2$ is even higher in 1-layer case, but the overall coupling strength in 1-layer is smaller than the bulk value.	107

Figure	Page
6.10 The Eliashberg function of bulk and 1-layer Ag.	108
6.11 The Eliashberg function of bulk and 1-layer Cu	109
7.1 Illustration of the Raman experiment setup on SLG.	115
7.2 Temperature profiles of the SLG under constant laser irradiation in MTM: a) The transient temperature profile in the center of the SLG in the first 400 ps after the laser is on and b) the steady-state temperature profile of SLG along the line from the center to the mid-point of one boundary. . .	116
7.3 The transient temperature profiles in the center of the SLG under pulse laser heating in MTM.	118
7.4 The comparison between the apparent lattice temperature T_p and the scat- tering lattice reservoir temperature T_{lat}	119
7.5 The normalized deviation of all 6 phonon branches in SLG.	121
7.6 Temperature profiles of the SLG under constant laser irradiation in TTM: a) The transient temperature profile in the center of the SLG in the first 400 ps after the laser is on and b) the steady-state temperature profile of SLG along the line from the center to the mid-point of one boundary. Four representative temperatures from MTM are also included for reference.	122
7.7 The transient temperature profiles in the center of the SLG under pulse laser heating in TTM. Figure b)'s horizontal axis is on logarithmic scale, which shows the electron relaxation in two models.	125
8.1 Illustration of the simulation domain consisting of a 500 nm-Si block and a 500 nm-Ge block.	130
8.2 The steady-state temperature profile of a Si-Ge interface. The degree of non-equilibrium induced by p-p coupling is not very strong, with all phonon branches in thermal equilibrium in most parts of the system. . .	133
8.3 A zoomed-in picture of the temperature profile of the Si-Ge interface. The fitted temperature T_{fit} is acquired by extrapolating the linear equilibrium part of the temperature profile. It can be observed that $\Delta T_{LA} < \Delta T_{fit}$ and $\Delta T_{TA} > \Delta T_{fit}$	134

ABSTRACT

Lu, Zexi PhD, Purdue University, December 2018. Multi-scale Simulations of Non-equilibrium and Non-local Thermal Transport. Major Professor: Xiulin Ruan, School of Mechanical Engineering.

Metallic components and metal-dielectric interfaces appear widely in modern electronics and the thermal management is an important issue. A very important feature that has been overlooked in the conventional Fourier's equations analyses is the non-equilibrium thermal transport induced by selective electron-phonon (e-p) coupling and phonon-phonon (p-p) coupling. It significantly affects many processes such as laser heating and ignoring this phenomenon can lead to wrong or misleading predictions. On the other hand, as devices shrink into nano-scale, heat generation and dissipation at the interfaces between different components start to dominate the thermal process and present a challenge for thermal mitigations. Many unresolved issues also arise from interfaces, such as the unexpected high interfacial thermal conductance (ITC) at metal-diamond interfaces. Both of these require a deep understanding of the physics at interfaces.

Therefore in this work, I present multi-scale simulations in metals/dielectrics and interfaces based on two-temperature model (TTM) and establish the new multi-temperature model (MTM). The methods are combined with Fourier's Law, molecular dynamics (MD), Boltzmann transport equations (BTE) and implemented to predict the thermal transport in several materials and interfaces where e-p coupling and p-p coupling are important. First-principles studies based on density functional theory (DFT) are also presented as predictive approaches to acquire the properties, as well as investigating the new physical phenomenon of non-local e-p coupling in metals. This research seeks to provide general, sophisticated but also simple simulation approaches which can help people accurately predict the thermal transport process. It

also seeks to explore new physics which cannot be captured and predicted by conventional analyses based on Fourier’s Law and can advance our understanding as well as providing new insights in the current thermal analysis paradigm.

The first part of this thesis focuses on the non-equilibrium thermal transport in metals and across metal-dielectric interfaces based on TTM. First of all, non-equilibrium thermal transport in metal matrix composites (MMC) is investigated. Metal particle is usually added to polymer matrix for enhanced thermal performance. Here we apply TTM calculations and manifest a “critical particle size” above which the thermal conductivity of the composite material can be enhanced. MD simulations are performed to predict the thermal properties. TTM-Fourier and TTM-BTE calculations are conducted as comparisons. The widely used Au-SAM (self-assembly-monolayers) material pair is chosen to demonstrate our models. For a 1-D SAM-Au-SAM sandwich system, the two calculation approaches present almost identical results, and the critical particle size is 10.7 nm. A general interpretation of thermal transport in sandwiched metal thin films between two dielectric materials is also presented. It is found that when the film thickness is on the order of several nanometers, due to strong e-p non-equilibrium the thermal transport is dominated by phonons and electrons hardly contribute.

Then the e-p non-equilibrium thermal transport across metal-dielectric interfaces is investigated using TTM-MD. One possible explanation to the unexpected ITC at metal-diamond interfaces is the cross-interface e-p coupling mechanism, which is based on the hypothesis that electrons can couple to phonons within a certain distance rather than just those at the same location. Therefore we extend TTM-MD by modifying its governing equation to a non-local integral form. Two models are proposed to describe the coupling distance: the “joint-phonon-modes” model and the “phonon-wavelength” model. A case study of thermal transport across Cu-Si interfaces is presented, and both models predict similar coupling distances of 0.5 nm in Cu and 1.4 nm in Si near the interfaces. The cross-interface e-p coupling can increase the ITC by 20% based on our models. Based on the results, we construct a

new mixed series-parallel thermal circuit. It is shown that such a thermal circuit is essential for understanding metal-nonmetal interfacial transport, while calculating a single resistance without solving temperature profiles as done in most previous studies is generally incomplete.

Inspired by the previous work, we investigate further into the physics of non-local e-p coupling. First-principles calculations based on DFT is used due to their predictive feature without assumptions or adjustable parameters. By calculating the e-p coupling in metal films of different sizes, we find that e-p coupling has size effect which can only be explained by a non-local coupling picture. Results show that in Al, electrons and phonons can couple to each other in a range of up to 2 lattice-constants, or 0.8 nm. The coupling strength between electrons and phonons in adjacent atomic layers still has 75% of that in the same layer. Comparative studies are also performed on Cu and Ag. Results show that their non-local e-p coupling is not as significant as in Al, with coupling distances of 0.37 nm for Cu and 0.49 nm for Ag. Similar results in Cu and Ag also indicate that materials with similar electronic structures have similar non-local e-p coupling properties.

In TTM, it is assumed that phonons are in thermal equilibrium and have a common temperature. In the second part of this thesis we go beyond TTM to investigate the non-equilibrium between phonons as well. TTM is extended to a general MTM with e-p coupling strength for each phonon branch. An averaged scattering lattice reservoir is defined to represent p-p scattering. The thermal transport process in single-layer graphene under constant and pulse laser irradiation is investigated. Results show that the phonon branches are in strong non-equilibrium. A comparison with TTM reveals that MTM can increase the thermal conductivity prediction by 50% and the hot electron relaxation time by 60 times. We also perform MTM simulations on Si-Ge interfaces to investigate the effect of non-equilibrium thermal transport on ITC. Results show that thermal non-equilibrium between phonons will introduce additional resistance at the interfaces, which is similar with e-p non-equilibrium's impact on ITC at metal-dielectric interfaces.

1. INTRODUCTION

1.1 Motivation

Nowadays as electronics shrink into nano-scale and operate with increasing volumetric power consumption, thermal management in devices becomes an important issue in advancing the technology. The thermal transport process in metallic systems draws researchers' attention as metal components and metal-dielectric interfaces appear widely in modern electronics, such as central processing unit in computers, hard drives, heat-assisted magnetic recording (HAMR) devices and laser diodes [1–5]. A very important feature in such systems is the coupled thermal transport between electrons and phonons. For many applications, such as laser-matter interaction, electrons and phonons can be driven into strong non-equilibrium due to selective electron-phonon (e-p) coupling and phonon-phonon (p-p) coupling, and their respective temperature profiles significantly deviate from each other [6–8]. While this phenomenon significantly affects processes such as hot electron relaxation and thermal measurements in experiments, it has been largely overlooked in classical theoretical analysis and previous studies. Therefore a fundamental understanding of the non-equilibrium thermal transport is necessary for accurately predicting the physics and performance of devices, thus providing guidance in designing such nano-structures. Providing access to sophisticated but simple simulation tools which can capture the non-equilibrium thermal transport feature will be beneficial for experimentalists and engineers in a wide range of applications.

On the other hand, heat generation and dissipation at interfaces becomes dominating at nano-scales. While the research into phonon thermal transport physics has received extensive efforts and its physics has been well understood, the electron counter part remains relatively ambiguous and there is plenty of space to research in

depth. Many long-time unsolved debates are related to metal-dielectric interfaces, e.g. the unexpected high thermal conductance at metal-diamond interfaces [9, 10]. The experimentally measured interfacial thermal conductances (ITC) at interfaces such as Pb-diamond and Au-diamond are significantly higher than their upper limits predicted by classical phonon transport theory. There have been two debating opinions for such large interfacial conductance: 1) inelastic phonon scattering which is not accounted for in the classical theory [10–15] or 2) cross-interface e-p coupling [9, 16–20], but no consensus has been reached. On top of that, the effect of the aforementioned non-equilibrium thermal transport has not been demonstrated while an investigation can potentially provide insights to understanding these issues. Therefore an investigation into the interfacial thermal transport, which includes thermal non-equilibrium feature and non-local e-p coupling, is important in gaining a deeper understanding of the physics as well as shredding light upon the unsolved debates.

The major focus of this thesis is investigating the non-equilibrium and non-local thermal transport in metals and at interfaces as well as developing simulation tools accordingly.

1.2 A quick review of non-equilibrium and non-local thermal transport

In the area of thermodynamics, temperature is defined at locations which are in local thermal equilibrium. Phonons, which are bosons and the particle representation of lattice vibration, follow the Bose-Einstein distribution [21]:

$$n(\hbar\omega) = \frac{1}{e^{(\hbar\omega)/k_B T} - 1}, \quad (1.1)$$

where ω is the phonon frequency, k_B is the Boltzmann constant and T is the temperature. Electrons, which are fermions, follow the Fermi-Dirac distribution:

$$f(\epsilon) = \frac{1}{e^{(\epsilon-\mu)/k_B T} + 1}, \quad (1.2)$$

where ϵ is the electron energy state. A local thermal equilibrium means there is a common temperature T that can be applied to Eqs. (1.1) & (1.2), which is also the

apparent temperature we can observe through measurements. Many classical thermal theories and techniques, such as the acoustic mismatch model (AMM), diffuse mismatch model (DMM) and heat diffusion equations, are based on the assumption of local thermal equilibrium, and have been successful in analyzing and predicting the thermal transport process in many materials [22]. Non-equilibrium thermal transport, on the other hand, involves thermal states not in local equilibrium, which cannot be described by Eq. (1.1) or (1.2). All materials have multiple phonon branches. Most metals with a face-centered cubic (FCC) unit cell have 3 phonon branches, while many semiconductors such as Si, Ge and semi-metals such as graphene and graphite have 6 phonon branches, and composites can have 9 or more phonon branches. Phonons belonging to different branches have different vibration patterns and physical properties. As a result different phonon modes and electrons in the material can be driven into non-equilibrium under certain conditions. It has been shown that in many applications, such as laser-matter interactions, heat transfer across metal-dielectric interfaces, high-energy irradiation in nuclear reactors or space and hot electron relaxation in solar cells, local thermal non-equilibrium is observed to dominate the physical process [7, 23–30]. For example, due to the different e-p coupling strength of different branches, during an ultrafast laser heating process, the amounts of energy received by different phonons from the electrons vary and they will not have a common temperature, as is shown in Fig. 1.1 [6]. When heat transfers across a metal-dielectric interface, electrons and phonons have different transmission coefficients which will induce an e-p non-equilibrium near the interface [24, 31]. Under such conditions, electrons and different phonon branches have different temperatures and Eqs. (1.2) & (1.1) have to be applied to them separately. If an analysis based on local thermal equilibrium is still applied, one may get wrong or misleading results. For example, in a device under non-equilibrium thermal transport, some of the phonons can be much hotter than the others, leading to non-thermal failure although the average lattice temperature is still within the damage threshold [25, 32]. Therefore a fundamental understanding of the non-equilibrium thermal transport is necessary for accurately

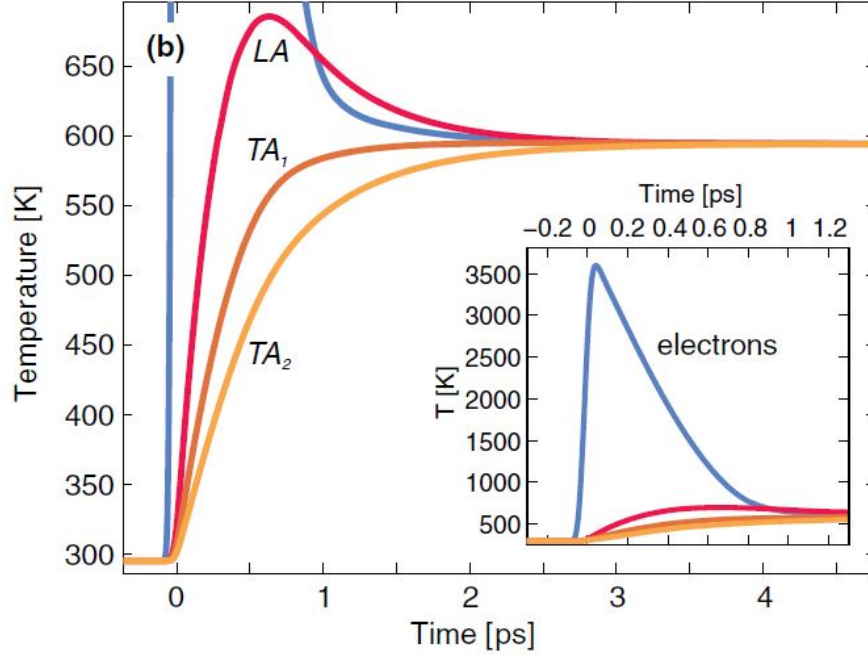


Figure 1.1. Illustration of the ultrafast laser heating and hot electron cooling processes in aluminum in Ref. 6. The temperature profiles are predicted from calculations with fitted parameters matching the experimental data. The 3 different phonon branches have different temperature due to their different coupling strength to the electrons.

predicting the physics and performance of devices, thus providing guidance in designing such nano-structures.

The observation of thermal local non-equilibrium dates back to as early as during the laser experiments decades ago where electrons and phonons were found to be at different temperatures and couple to each other [33–36]. Since then local thermal non-equilibrium is known to appear in a wide range of thermal processes. While so far it is not possible to directly measure the temperatures of electrons and different phonon modes, the thermal non-equilibrium is often confirmed through their effect on the observations. For example, it is reported that in metal thin films sandwiched between dielectrics, the measured thermal conductivity is almost identical to that of the lattice while electrons hardly contribute [37]. This is due to the e-p non-

equilibrium at the metal-dielectric interfaces. The observation of the “hot phonon bottleneck”, which causes the hot electron cooling rate in solar cells to be much smaller than predictions based on local equilibrium assumption, is caused by p-p non-equilibrium induced by selective e-p coupling [14,28], as is shown in Fig 1.2. Similar phenomena have also been observed in laser experiments such as the pump-probe measurements, as well as materials under multiple forms of irradiation in nuclear reactors and space [7,8,29,30,38–46]. However, despite being well-acknowledged about its existence, the significance of non-equilibrium thermal transport is not well understood. A quantitative understanding of the effect of local thermal non-equilibrium on the heat transfer process cannot be achieved by experiments alone due to the absence of techniques to acquire the resolved temperature profiles. For example, the reported values of the thermal conductivity of single-layer graphene (SLG) range from 600 W/mK to as high as 5800 W/mK [47–51]. While non-equilibrium thermal transport is supposed to exist in Raman spectroscopy measurements which involves laser heating, experimental result cannot tell how much it causes the measured value to deviate from the intrinsic one, nor its relative contribution compared with other proposed mechanisms [52–55]. Therefore theoretical works are needed to compensate the limitations of current experiments.

To complement the study of non-equilibrium thermal transport, numerical simulations are actively getting developed. The spectral Boltzmann transport equation (BTE) is always a choice for rigorous solutions, but the high computation cost hinders its possible wide application. Simplified BTE approaches based on approximations have been applied to low dimension structures to predict the thermal transport process including the resolved lattice temperature profiles [56–58]. To describe the e-p non-equilibrium in metals, two-temperature model (TTM) which separates the electron’s and phonon’s temperatures is developed [31,59]. TTM is later extended to multi-temperature model (MTM) which also accounts for the p-p non-equilibrium [6,7]. Classical simulation approaches such as molecular dynamics, have also been combined with models such as TTM or post-processing techniques such as modal analysis

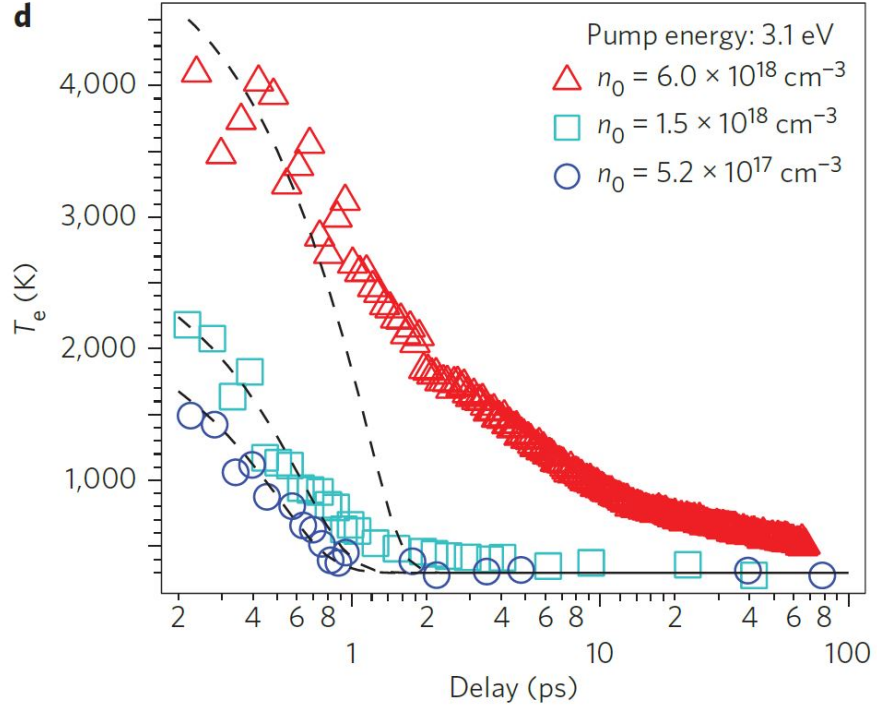


Figure 1.2. Illustration of hot electron cooling process under different laser intensity measured in experiment compared with TTM predictions in Ref. 28. Symbols represent the experimental electron temperature cooling curve while the dash line represents the TTM prediction. n_0 denotes the incoming photon density determined from laser power. It is clearly seen that the actual cooling rate is much slower than prediction at high power laser input.

to manifest the non-equilibrium thermal transport [18, 24, 60, 61]. These simulation approaches, along with the resolved temperature profiles they calculated, all demonstrated the significance of local thermal non-equilibrium and its effect on heat transfer in different applications. They have provided support for engineering analysis and experimental interpretations, as well as predicting physical processes which have yet to be realized in real applications.

1.2.1 Thermal non-equilibrium at interfaces between different materials

Thermal transport across interfaces between different materials has become a popular topic among the research community nowadays, especially when the system dimension is very small such as the nano-size electronic devices and multi-layer structures. At such scale, interfacial thermal transport dominates over the conduction inside each material, and the prediction of interfacial thermal conductance is crucial for the design and evaluation of these nano-structures.

When heat goes across the interface between two different materials, it will experience temperature discontinuity due to the lattice mismatch between the two materials as well as surface conditions, etc. The ITC h_B is defined as the ratio of the heat flux J over the temperature jump ΔT , and the thermal boundary resistance (TBR) R_B is defined as the inverse of h_B :

$$h_B = \frac{J}{\Delta T}, R_B = \frac{1}{h_B} \quad (1.3)$$

R_B is determined by many factors as mentioned above. If we consider an ideal interface while isolating the surface conditions and external forces, then R_B is only determined by the lattice and electronic properties of the two materials.

Traditional AMM and DMM approaches have been widely used due to their simplicity, and have proved to be successful in the prediction of ITC at low temperatures (<100 K) [22]. However, usually they are applied while assuming local thermal equilibrium with a single temperature profile, which can lead to potential inaccuracy as have been demonstrated by several studies investigating the discrepancy between ex-

perimental measurements and theoretical predictions [9–14, 62]. Efforts have since been put into studies focused on the non-equilibrium thermal transport across interfaces. Therefore in this section, we will review the works done on this topic.

Electron-phonon non-equilibrium at metal-dielectric interfaces

Metal-dielectric interfaces appear widely in modern devices. While the thermal transport in dielectric is mostly through lattice vibration, or the phonons, the thermal transport in metals is complicated by the coupled transport between electrons and phonons. At these interfaces, usually electrons are considered as not transmittable to the dielectric while phonons can transfer energy between the two materials. This will cause e-p non-equilibrium near the interface even if the system is in steady state, which has been demonstrated to have a strong impact on the interfacial thermal transport [18, 24, 59, 63, 64].

The effect of e-p non-equilibrium has been explored in experiments at 1 K more than 30 years ago [65]. In principle, the theoretical prediction could be achieved through rigorously solving BTE, but the cumbersome calculations hinder its applications. Practical prediction methods had been absent until the introduction of the Fourier TTM by Majumdar and Reddy [31].

In metals, electrons contribute to most of the thermal transport while phonons also play a non-negligible part. The two types of energy carriers can easily be driven into non-equilibrium through their different interaction with external excitations or different boundary conditions. Usually this e-p non-equilibrium has significant effect on the thermal transport process. In TTM, electrons and phonons are described as two interacting subsystems with their own temperatures [31]. The governing equations are:

$$\begin{aligned} C_e \frac{\partial T_e}{\partial t} &= \nabla(k_e \nabla T_e) - G_{ep}(T_e - T_p), \\ C_p \frac{\partial T_p}{\partial t} &= \nabla(k_p \nabla T_p) + G_{ep}(T_e - T_p). \end{aligned} \tag{1.4}$$

Eq. (1.4) describes the two channel-coupled energy transfer process in metals, where their interaction is determined by the coupling factor G_{ep} and their temperature difference. Here e and p refer to electron and phonon respectively. T is the temperature while t is time. k and C refer to the thermal conductivity and volumetric heat capacity of the energy carriers respectively. Eq. (1.4) allows us to calculate the analytic solution for the temperature profiles. At a 1D metal-dielectric interface, usually electrons are considered as insulated while phonons can transfer energy between the two materials. The different boundary conditions are as follows:

$$\begin{aligned} -k_{nonmetal} \frac{\partial T_{nonmetal}}{\partial x} \Big|_{x=0} &= -k_{p,metal} \frac{\partial T_{p,metal}}{\partial x} \Big|_{x=0} = J, \\ -k_{e,metal} \frac{\partial T_{e,metal}}{\partial x} \Big|_{x=-\frac{L}{2}+0} &= 0. \end{aligned} \quad (1.5)$$

$x = 0$ denotes the position of the interface. The different boundary conditions will cause the two temperature profiles to deviate from each other near the interface, resulting in the so-called e-p non-equilibrium, as is shown in Fig. 1.3. This presents an extra temperature jump in addition to the one introduced by the p-p coupling R_{Bd} , and can be conceived as an additional TBR R_{ep} in series with the phonon coupling resistance. Wang et al has derived an expression for R_{ep} by solving Eq. (1.4) while taking the extreme limit when the film is infinite large so that electrons and phonons are in thermal equilibrium away from the interface [24]:

$$R_{ep} = \frac{1}{(G_{ep}k_p)^{\frac{1}{2}}} \left(\frac{k_e}{k_e + k_p} \right)^{\frac{3}{2}}. \quad (1.6)$$

TTM has since been widely applied in both experimental and modeling studies of metal-dielectric interfaces. Generally the studies have consistent results with the theoretical TTM prediction, that the e-p non-equilibrium introduces thermal resistance at metal-dielectric interfaces. Li et. al. applied TTM to interpret their experimental results of thermal conduction in Mo-Si multilayers with period below 10 nm [37]. The e-p non-equilibrium is reported to be responsible for the low thermal conductivities k measured, which is almost identical to the materials' lattice portion k_p . A later

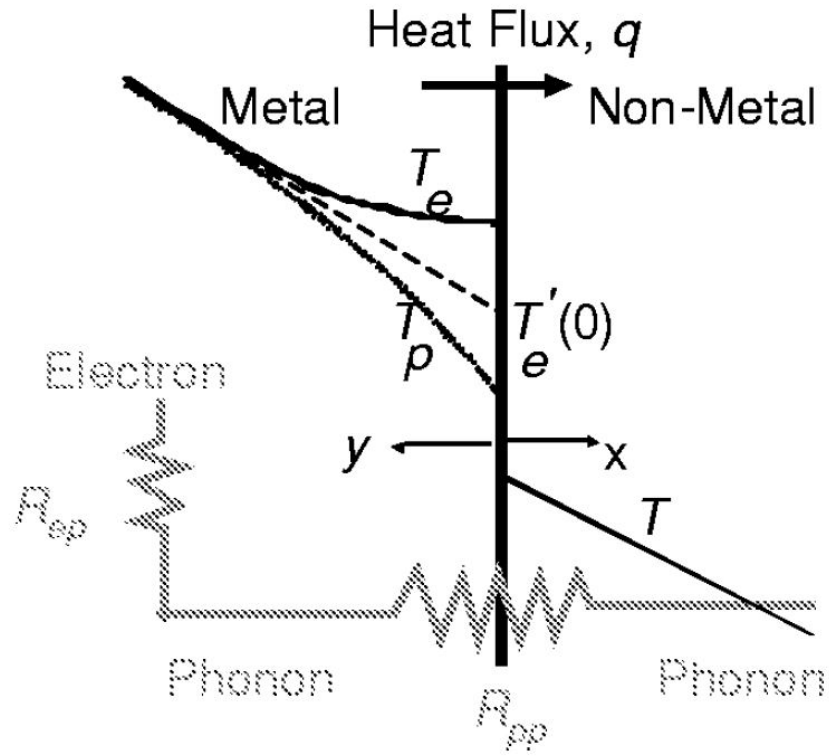


Figure 1.3. Illustration of e-p non-equilibrium near a metal-dielectric interface derived from TTM in Ref. 31. Electrons are insulated from entering the non-metal therefore have a flat curve near the interface. Their energy is dumped to phonons and transferred to the other side. The e-p non-equilibrium results in an additional TBR in series with the p-p TBR.

study of Lu et. al. applied TTM in metal nanoparticle-polymer matrix, and derived a more general form of R_{ep} [59]. Their analysis shows that due to e-p non-equilibrium the thermal conduction in metal thin films sandwiched between dielectrics is dominated by phonons, which is consistent with Li's work. TTM has also been combined with effective medium theory (EMA) in modeling random size-metal nanoparticle-composite materials in higher dimensions [66–69]. Consistently the addition of e-p non-equilibrium to the original p-p TBR will further reduce the prediction of the effective k of the composite material. In a series of their works, Wang and Lu implemented TTM in molecular dynamics, adding the electronic participation in the classical atomic simulation tool while keeping its advantage in modeling complicated lattice vibrations [18, 24]. By modifying the model of Duffy and Rutherford [60], they enabled TTM-MD simulations in non-periodic systems. The simulation results of ITC at Cu-Si and Cu-graphene interfaces show that R_{ep} usually have comparable value with the p-p TBR, accounting for 30% to 70% of the total TBR. Simplified TTM-BTE in 1D has also been solved practically using the equation of phonon radiative transport (EPRT) and lattice Boltzmann methods [63, 64]. In addition, TTM is also extended to “three temperature model” with fitted parameters from experiments to describe the cross-interface e-p coupling at Au-Si and Au-glass interfaces in the studies of Hopkins et. al. [16, 70]. Recently models extended from TTM which not only separates the electrons' temperature from phonons, but also resolves the temperatures of different phonon branches, have also been developed. This will be discussed in more details in the later sections.

Phonon-phonon non-equilibrium at dielectric-dielectric interfaces

Besides e-p non-equilibrium at metal-dielectric interfaces, p-p non-equilibrium also exists. When heat transfers across the interface between two different materials, different phonon modes have different transmission coefficients, which will result in a thermal non-equilibrium similar to the e-p non-equilibrium at metal-dielectric inter-

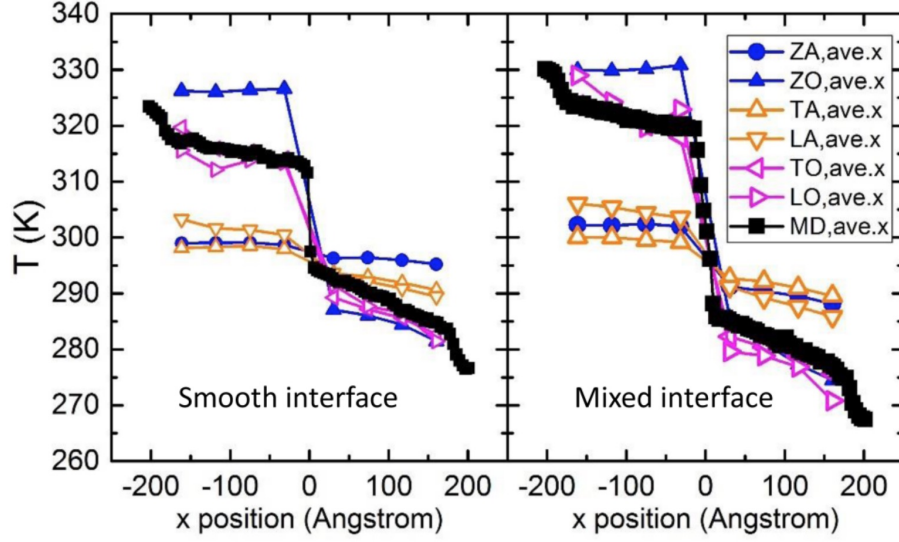


Figure 1.4. Illustration of phonon thermal non-equilibrium induced by different transmission at an SLG-BN interface from Ref. 61.

faces. This phenomenon has been manifested in Ref. 61. As is shown in Fig. 1.4, the temperatures of different phonon branches deviate significantly from each other at an SLG-BN interface.

Conventional analysis of ITC between two dielectric materials is based on AMM and DMM. In this study we will mainly introduce the DMM because it is more applicable to interfaces between two dissimilar materials with significant lattice mismatch. In DMM, only elastic phonon scattering is taken into consideration, which means phonon frequency will not change during the interfacial scattering, and phonons lose information of their original incident angle when they transport across the interface, and the transmission and reflection rates have the following relationship:

$$\begin{aligned} t_{12} &= 1 - r_{12}, \\ t_{12} + t_{21} &= 1. \end{aligned} \tag{1.7}$$

The detailed balance has to be satisfied to ensure energy conservation:

$$\Sigma D_1(\omega) v_{g1} n(\omega, T) \hbar \omega t_{12}(\omega) = \Sigma D_2(\omega) v_{g2} n(\omega, T) \hbar \omega t_{21}(\omega), \tag{1.8}$$

where D is the phonon density of states (DOS), n is the Bose-Einstein distribution, ω is the phonon frequency, v_g is the phonon group velocity. The summation is over all the phonon branches in the entire frequency range. If we take the infinitesimal temperature difference limit at the interface, then h_{Bd} can be expressed as follows [22, 71]:

$$h_B = \frac{\partial \Sigma D_1(\omega) v_{g1} n(\omega, T) \hbar \omega t_{12}(\omega)}{\partial T} \quad (1.9)$$

Eq. (1.9) is also known as the Landauer approach, which will be introduced in Chapter 8. There is also a term defined as the radiation limit h_R , which is the ITC derived from DMM with the transmission set to unity:

$$h_R = \frac{\partial \Sigma D_1(\omega) v_{g1} n(\omega, T) \hbar \omega}{\partial T} \quad (1.10)$$

The physical significance of h_R is the conductance when all the phonons incident from one materials enters the other material without being reflected. It is also the theoretical upper limit of h_B when only elastic phonon scattering is considered.

DMM has been successful in predicting the ITC between materials, especially the pairs with large lattice mismatch. In addition to dielectric interfaces, it is also applied to metal-dielectric interfaces because conventionally metal electrons are considered as insulated from entering the dielectric side, therefore only cross-interface phonon scattering exists. However, local thermal equilibrium for phonons is assumed through the entire analysis, which ignores some physics and can potentially lead to wrong results. Therefore it is necessary to investigate the significance of phonon thermal non-equilibrium at dielectric interfaces and accordingly develop a simple and general simulation tool.

Simplified BTE based on relaxation time approximation (RTA), which greatly reduces the calculation needed, has been applied in 1D Si-Ge superlattice [72]. The p-p transmission at the interfaces are calculated by phonon branch-resolved DMM. Their results clearly demonstrate the p-p non-equilibrium at Si-Ge interfaces induced by different phonon transmission. Similar with e-p non-equilibrium, the p-p non-equilibrium also introduces thermal resistance. Incorporating p-p non-equilibrium will

predict a lower ITC than a simple DMM or AMM result based on local equilibrium assumption.

MD has also been applied to investigate p-p non-equilibrium at dielectric interfaces. However, despite MD's advantage in practically modeling complicated lattice vibration physics, acquiring the resolved temperature profiles needs additional post-processing of simulation data. In the study of Feng et. al., MD simulation are performed on several systems made of different materials including an SLG-BN interface [61]. Spectral analysis is then performed to calculate the temperature of each phonon branch [73, 74], as is shown in Fig. 1.4. The optical phonon modes have significantly larger interfacial temperature jump than the acoustic phonons, especially the ZO phonons whose band overlap in the phonon dispersions of SLG and BN is negligible. The results are consistent with the expectation that p-p non-equilibrium can be induced by their different transmission at the interface. In a later MD study conducted by An et. al., simulation is performed across an SLG-SLG interface [75]. Phonons are divided into two groups: in-plane (IP) phonons (LA, TA, LO and TO phonons) and out-of-plane (OP) phonons (ZA and ZO phonons), and in one SLG only in-plane vibration is allowed thus removing ZA and ZO phonons in that side. A spectral analysis revealed similar IP-OP non-equilibrium with the e-p non-equilibrium at metal-dielectric interfaces, which is as expected since an analogy of IP-OP coupling to e-p coupling can be made with similar boundary conditions. Their results also showed that IP and OP phonons have weak coupling, so that their distributions will not be significantly affected by the scattering and the application of RTA is validated in SLG.

While all these previous works have manifested the p-p non-equilibrium at dielectric interfaces, a quantitative analysis of its significance, i.e. how much percentage error of TBR will occur without considering the local thermal non-equilibrium, is still absent.

1.2.2 Electron-phonon and phonon-phonon non-equilibrium in materials under irradiation

In addition to local thermal non-equilibrium induced by difference transmission at interfaces, it also exists in single materials. For example, in metallic materials under laser irradiation, electrons are heated up first which subsequently heat up the phonons through e-p coupling. It has been demonstrated that different phonon modes have different coupling strength to the electrons, and this selective e-p coupling can cause significant non-equilibrium among phonons. Similar phenomena have also been observed in metals under other forms of irradiation, e.g. ion irradiation in nuclear reactors and space. TTM has been successful in resolving the electron's temperature, but phonons are still assumed to be in local equilibrium. The fact that the hot electron cooling rate measured by experiments is significantly slower than TTM prediction indicates that more elaborate analysis is needed [6, 28].

Similar with the calculation of e-p non-equilibrium, spectral BTE can provide rigorous solutions, but is hindered from practical application by its cumbersome mathematical calculations. A work-around of this issue is the application of RTA, which assumes the scattering between particles does not affect their distributions. Based on RTA, Chen et. al. developed the spectral BTE in dielectric materials which greatly simplifies the phonon scattering calculation and can resolve the steady-state temperature profiles of different phonon modes in thin films with fixed boundary temperatures [56, 57]. A more recent work by Sadasivam et. al. utilized first-principles BTE to model the hot electron cooling process in several semiconductors [58]. Their results showed that the hot electron cooling time is 1-15 ps longer than the simple TTM prediction, which is consistent with experimental observations. A generalized TTM was proposed to take into account the phonon thermalization.

Besides BTE, models beyond TTM have also been developed. By extending TTM to also include p-p coupling, Waldecker et. al. proposed a model similar with RTA BTE but has the same calculation simplicity as TTM. Symmetric p-p cou-

pling strength is assumed for all phonons and the parameter is acquired by fitting the temperature cooling curve to their experimental data. Though based on hypotheses, their model is successful in manifesting the local non-equilibrium among acoustic phonons in metal, which matches their corresponding pulse laser heating experiment. A contemporary work by Vallabhaneni et. al. implemented RTA in a similar model, and extended TTM to a general MTM, which can model non-equilibrium thermal transport with thermal properties acquired from first-principles calculations [7]. The governing equations of MTM are:

$$\begin{aligned} C_e \frac{\partial T_e}{\partial t} &= \nabla(k_e \nabla T_e) - \sum G_{ep,i}(T_e - T_{p,i}), \\ C_{p,i} \frac{\partial T_{p,i}}{\partial t} &= \nabla(k_p \nabla T_p) + G_{ep,i}(T_e - T_{p,i}) + G_{pp,i}(T_{lat} - T_{p,i}), \end{aligned} \quad (1.11)$$

i is the index of phonon branches.

Compared with Eq. (1.4), the e-p coupling term is modified to a branch-resolved form and a p-p coupling term is added for each phonon branch. Here i is the index for phonon branches, and $G_{ep,i}$ is the coupling factor between electrons and phonon branch i . The summation of $G_{ep,i}$ over all the phonon branches will lead to the e-p coupling factor G_{ep} in TTM:

$$\sum G_{ep,i} = G_{ep}. \quad (1.12)$$

The p-p scattering is represented by the coupling between each phonon branch and the “scattering lattice reservoir” which is represented by an averaged T_{lat} . It is an analogy of the e-p coupling using RTA based on the assumption that the p-p scattering has negligible effect on phonon distribution and phase space. $G_{pp,i}$ is the p-p coupling factor between phonon branch i and the scattering lattice reservoir, which is calculated using RTA from the following equation [76–79]:

$$G_{pp,i} = \frac{C_{p,i}}{\tau_i}, \quad (1.13)$$

where τ_i is the relaxation time of phonon branch i , and the scattering lattice reservoir’s temperature T_{lat} is defined to ensure the energy transfer among phonon branches is conserved:

$$\sum G_{pp,i}(T_{lat} - T_{p,i}) = 0. \quad (1.14)$$

Then by solving Eq. (1.11) numerically, we can obtain the transient and steady state temperature profiles of the system with resolved electron and phonon branch temperatures. It can be seen that MTM in Eq. (1.11) is essentially a spectral treatment of e-p coupling rather than the gray treatment in TTM in Eq. (1.4). A constant laser heating process of SLG which represents the Raman Spectroscopy measurement was simulated. Results showed great p-p non-equilibrium due to selective e-p coupling. The predicted k in MTM is almost 2 times as large as that of a simple TTM [7]. Besides, TTM-MD can also be applied as the complicated atomic vibrations are automatically included without ignorance of any phonon physics. During irradiation-metal interactions, ions with high kinetic energy or electromagnetic waves come into the material and get absorbed. The kinetic energy of the ions will be transferred to the system through collision with lattice atoms and electronic stopping effects, or the electromagnetic waves will be absorbed and excite the electrons, and either will generate significant e-p and p-p non-equilibrium. These processes appear widely in space and nuclear reactors where materials are exposed to intensive irradiation, and a clear picture of the non-equilibrium thermal transport process is necessary for researching the damage endurance and reliability of the materials. TTM-MD has often been used to simulate this process, and it has been shown the thermal non-equilibrium can considerably reduce the damage production in these irradiated-metals [30, 40, 42–45, 80].

1.2.3 Non-local thermal transport at metal-dielectric interfaces

In addition to the aforementioned potential inaccuracy caused by the assumption of local thermal equilibrium, DMM also fails in predicting h_{Bd} at several metal-diamond interfaces [9, 10], where the measured h_R is significantly larger than h_R , indicating that elastic phonon scattering alone cannot explain the energy transport. Generally two opinions emerge to provide explanations for this phenomenon. One of the ideas is that this high h_{Bd} is caused by inelastic scattering where phonons can split and combine and change their frequencies, which is not included in the

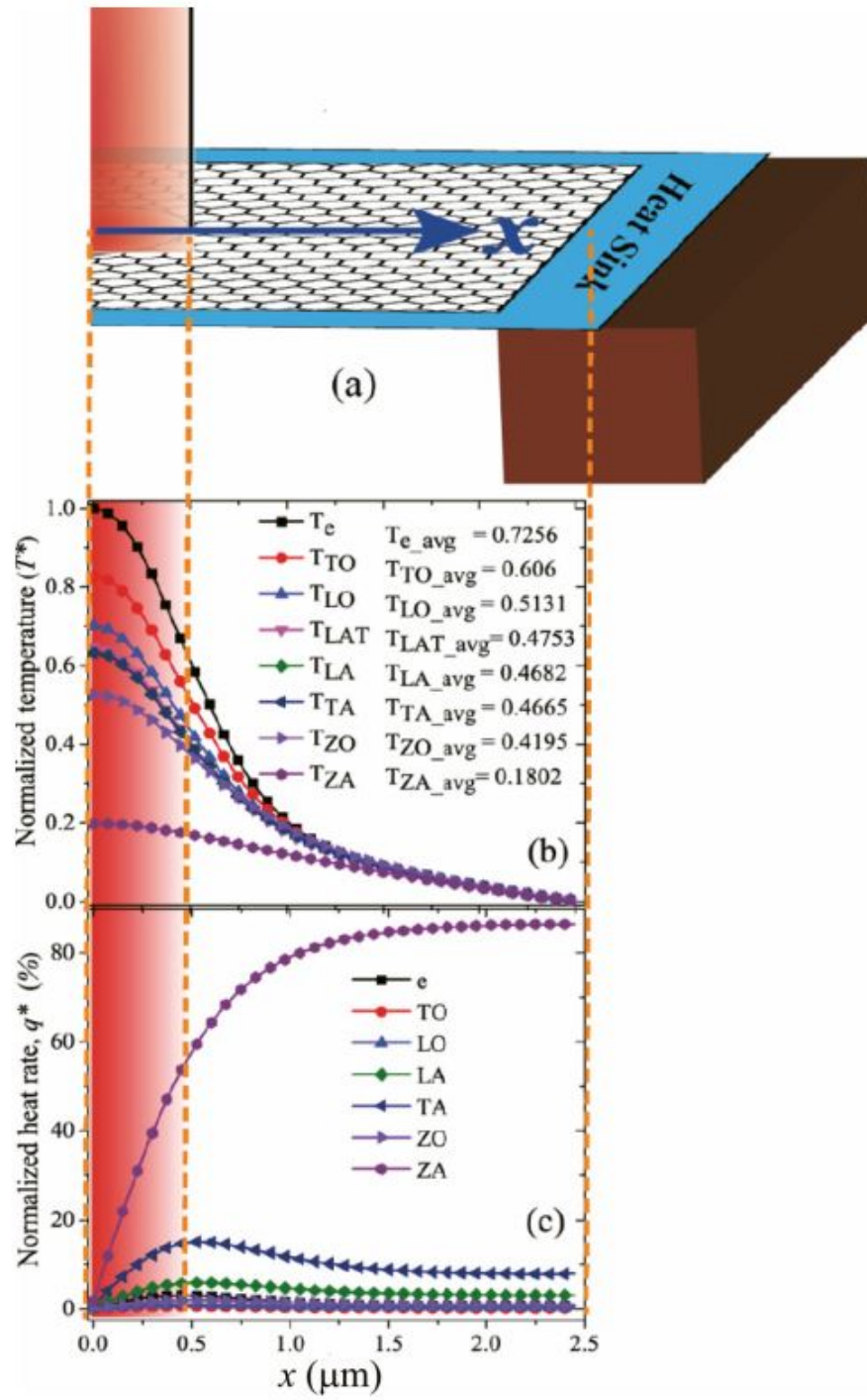


Figure 1.5. MTM prediction of the resolved temperature profiles showing e-p and p-p non-equilibrium induced by selective e-p coupling during a Raman spectroscopy experiment Ref. 7.

DMM model. An extended DMM approach has been proposed to include the inelastic scattering portion of ITC and has been favored by many experimentalists [10–14]. Atomistic Green’s function has also been applied and suggests similar results [15]. On the other hand, because all these material pairs are metal-diamond interfaces, it is proposed that metal electrons are able to couple to dielectric phonons across the interface and introduced extra conductance, which is contrary to conventional views. Several approaches, including extended lattice dynamics with electronic deformation potential, first-principles calculations based on DFT, non-equilibrium Green’s function (NEGF) and TTM-MD with non-local e-p coupling have been proposed to describe this cross-interface e-p coupling [9, 16–20]. However, no consensus has been reached as none of these hypotheses has been confirmed. Therefore in this thesis, I will also present several studies focused on developing simulation tools as well as manifesting the physics.

1.3 Methodology

1.3.1 Molecular dynamics

MD simulations provides atomic scale calculations that can be used to investigate the properties of materials [81–84]. Using interatomic potentials and the lattice structure as inputs, the simulation provides a classical prediction of the atom behaviors. MD is advantageous in that by simulating the movements of all atoms in the system, it automatically includes many sophisticated physics such as inelastic phonon scattering, etc. Many properties including physical, mechanical and chemical properties can be directly acquired or derived from the simulation results. However, despite the multiple advantages MD also has its limitations. First and foremost is that MD simulation does not include electronic effects, therefore the electrical properties, including electrical thermal conductivity and e-p coupling etc. cannot be modeled. Moreover, a valid prediction of the material properties requires accurate interatomic potentials, but developing potentials, especially for materials with complex lattice structures, is

very difficult and the accuracy of the result is still limited by the approximated form of the potential expressions. The first-principles MD can bypass this issue, but comes with the cost of high computation demand [85]. Last but not least, the classical simulation with no quantum effects also makes the result deviate from reality, e.g. phonons in thermal equilibrium do not follow Bose-Einstein distribution. Nevertheless, MD still proves to be a useful tool in many cases and has drawn a lot of attention among researchers.

Two-temperature model molecular dynamics

The original MD provides simulation for atoms, or phonons, while electrons are not included. Therefore it is not fitted in performing simulation for a metallic system. By combining MD with TTM, one is able to include the effect of electrons while keeping MD's advantages in simulating phonons. Originally developed by Duffy and Rutherford [60, 86], the basic idea of TTM-MD is to represent electrons' scattering with phonons as an "friction force" added to the atoms in the simulation domain. The system is first discretized into finite volume grids. And electron "gas" is added to each grid with proper electronic properties. The electronic gas has its own thermal diffusion, and atoms will interact with the gas in the same grid. The motion equation for atom i becomes:

$$m_i \frac{\partial \mathbf{v}_i}{\partial t} = \mathbf{F}_i(t) - \gamma_i \mathbf{v}_i + \tilde{\mathbf{F}}_i(t), \quad (1.15)$$

where m and v are the atomic mass and velocity, \mathbf{F}_i is the total force exerted on atom i . γ is a friction factor representing the electron-phonon interaction, and it is related to G_{ep} as follows:

$$\gamma_i = \frac{m_i G_{ep}}{3n_i k_B}, \quad (1.16)$$

where n is the atom density. $\tilde{\mathbf{F}}_i$ is a random force term commonly seen in Langevin dynamics and has the following expression:

$$\tilde{\mathbf{F}}_i(t) = \sqrt{\frac{24k_B T_e \gamma_i}{\Delta t}} \tilde{\mathbf{R}}_i, \quad (1.17)$$

where Δt is the time step in the MD simulation and \mathbf{R} is a random vector $[R_1, R_2, R_3]$ with each element ranging from -0.5 to 0.5. Then the coupling term in Eq. (1.4) can be expressed as:

$$\tilde{E}_{ep} = G_{ep}(T_e - T_p) = [-\gamma_i \mathbf{v}_i + \tilde{\mathbf{F}}_i(t)] \mathbf{v}_i \Delta t. \quad (1.18)$$

Then the electronic thermal diffusion and EPC mechanism has been successfully added to MD simulations. TTM-MD has proved to be successful in predicting the thermal transport in metallic systems [18, 24, 41, 43, 46].

1.3.2 Boltzmann transport equation and the gray lattice Boltzmann method

BTE provides a semi-classical approach to describe the statistical behavior of thermodynamic systems [87, 88]. A general form of the governing equation describes how the energy carrier's population changes with the scattering, its momentum and external forces. For example the governing equation for phonons is:

$$\frac{\partial n_i}{\partial t} + \mathbf{v} \cdot \nabla_{\mathbf{r}} n_i + \mathbf{F} \cdot \nabla_{\mathbf{p}} n_i = \left(\frac{dn_i}{dt} \right)_{scatter}, \quad (1.19)$$

where n denotes the Bose-Einstein distribution function and i is the index for modes, \mathbf{F} is external force, \mathbf{r} and \mathbf{p} are the trajectory and momentum vector respectively. The rigorous solution of Eq. (1.19) is very cumbersome, therefore for more practical applications several simplification are often made and corresponding models are developed. RTA is commonly used to simplify the calculation of the scattering term on the right side [56, 77]

$$\left(\frac{dn_i}{dt} \right)_{scatter} = \frac{n_{0,i} - n_i}{\tau_i}, \quad (1.20)$$

where n_0 is the equilibrium distribution, and τ is the relaxation time of the particle. Then Eq. (1.19) can be integrated over the frequency range to get its energy density form:

$$\frac{\partial e_i}{\partial t} + \mathbf{v} \cdot \nabla_{\mathbf{r}} e_i = \frac{e_{0,i} - e_i}{\tau}. \quad (1.21)$$

Eq. (1.21) is the more commonly-used form of BTE, which focuses on a physical quantity that is more straightforward to acquiring the heat fluxes and temperatures

in the calculation domain. Based on RTA and an analogy between phonon and photon radiative transport, EPRT has been developed which expressed the phonon energy flow in terms of radiation intensity [88,89]. The temperature profile calculated from EPRT is usually non-linear, which deviates from Fourier's Law prediction [90]. These simplified BTE approaches have since been widely applied in investigating the phononic heat transport. It has proved to be successful in predicting the size effect of thermal conductivity in thin films which the classical methods such as Fourier's Law fails to capture.

The Lattice Boltzmann method (LBM) is a discrete development of BTE, in which the system is discretized into meshes [91–93]. The particles can only propagate to the adjacent meshes in the allowed directions and the transport equation is solved in these adjacent grids. While its computation cost grows exponentially with the size of the simulation domain, and its accuracy also depends on the dimensions and quality of discretion, LBM is still a practical approach in predicting the thermal transport in thin films of low dimension. In a gray model under the Debye approximation, all phonon branches are collapsed into one single dispersion with a constant propagation speed, which makes it exceptionally suitable to apply the LBM. Under the gray model assumption, Eq. (1.21) can be transformed into a single-mode form:

$$\frac{\partial e}{\partial t} + \mathbf{v} \cdot \nabla_{\mathbf{r}} e = \frac{e_0 - e}{\tau}, \quad (1.22)$$

In a 1D system, phonons can only propagate in two directions. They will be generated in one grid and propagate to one of the two adjacent grids and collide with the phonons generated there. If the grid size is set to be Δx , then the time step of the calculation should be $\Delta t = \Delta x/v_x$ to ensure that phonons can only travel to the adjacent grids. Then the discretized LBM equation can be written as:

$$e_i(x + \Delta x, t + \Delta t) = (1 - W_i)e_i(x, t) + W_ie_{0,i}(x, t), \quad (1.23)$$

where i denotes the propagation direction, $W_i = \Delta t/\tau$ is a weight factor that sets the contribution of ballistic and diffusive transport. The equilibrium energy density e_0 can be calculated as follows under isotropic assumption:

$$e_{0,i}(x, t) = \frac{\sum_i^d e_i(x, t)}{d}. \quad (1.24)$$

So far the basics of LBM for phonons has been introduced. It can also be extended to include electron effect similar with TTM-MD, which will be covered in the later specific section.

1.3.3 First-principles method based on density functional theory

Density functional theory (DFT) is a computational quantum mechanical modeling method used to investigate the electronic structure of many-body systems. Many first-principles calculations based on DFT has been developed to predict material properties of interest, and among them is the e-p coupling factor G_{ep} . The e-p coupling strength originates from electron-phonon scattering, which can be described by the Fermi's golden rule (FGR) [94]

$$P_{i \rightarrow f} = \frac{2\pi}{\hbar} |\langle f | H' | i \rangle|^2 \rho. \quad (1.25)$$

Eq. (1.25) describes the transition probability P from the initial state i to the final state f , where H' is the perturbation matrix and ρ is the density of final states. Based on FGR, the electron-phonon scattering rate can be calculated as:

$$\gamma_q = \frac{2\pi}{\hbar} \sum_{k,k'} |M_{kk'}|^2 \times f_k(1 - f_{k'}) [n_q \delta(\varepsilon_k - \varepsilon_{k'} + \hbar\Omega_q) - (n_q + 1) \delta(\varepsilon_k - \varepsilon_{k'} - \hbar\Omega_q)], \quad (1.26)$$

Here k and q refer to the electron and phonon wave vector respectively, f and n refer to the Fermi-Dirac and Bose-Einstein distribution respectively, ε is the electron energy and Ω is the phonon frequency. $M_{kk'}$ is the electron-phonon scattering matrix element derived from the FGR:

$$M_{kk'} = \sqrt{\frac{\hbar}{2\omega_q}} \langle \psi_k | \partial U | \psi_{k'} \rangle, \quad (1.27)$$

where U is the self-consistent Kohn-Sham potential exerted on electrons. From Eq. (1.26), the change rate of electron and phonon's populations can be calculated:

$$\begin{aligned} \left(\frac{\partial f_k}{\partial t}\right)_{ep} &= -\frac{2\pi}{\hbar} \sum_q |M_{kk'}|^2 \times \{f_k(1-f_{k'})[(n_q+1)\delta(\varepsilon_k - \varepsilon_{k'} - \hbar\Omega_q) + n_q\delta(\varepsilon_k - \varepsilon_{k'} + \hbar\Omega_q)] \\ &\quad - (1-f_k)f_{k'}[(n_q+1)\delta(\varepsilon_k - \varepsilon_{k'} + \hbar\Omega_q) + n_q\delta(\varepsilon_k - \varepsilon_{k'} - \hbar\Omega_q)], \\ \left(\frac{\partial n_q}{\partial t}\right)_{ep} &= -\frac{4\pi}{\hbar} \sum_{k,k'} |M_{kk'}|^2 \times f_k(1-f_{k'})[n_q\delta(\varepsilon_k - \varepsilon_{k'} + \hbar\Omega_q) - (n_q+1)\delta(\varepsilon_k - \varepsilon_{k'} - \hbar\Omega_q)]. \end{aligned} \quad (1.28)$$

The factor 2 in Eq. (1.28) accounts for electron spin degeneracy. Then the energy transfer rate can be calculated as:

$$\frac{\partial E_{ep}}{\partial t} = \frac{4\pi}{\hbar} \sum_{k,k'} \hbar\Omega_q |M_{kk'}|^2 S(k, k') \delta(\varepsilon_k - \varepsilon_{k'} + \hbar\Omega_q). \quad (1.29)$$

Here $S(k, k') = (f_k - f_{k'})n_q - (1 - f_k)f_{k'}$ is the thermal factor. This $\partial E_{ep}/\partial t$ corresponds to the coupling term $G_{ep}(T_e - T_p)$ in Eq. (1.4), and can be used to derive expressions for many e-p coupling parameters. More details will be given in the later sections.

1.4 Objectives and Scope of Thesis

The major objective of this thesis is to uncover significant new physics associated with non-equilibrium and non-local heat transfer in materials and across interfaces. Meanwhile it also seeks to develop simulation tools which includes the correct physics and is easily accessed by other researchers.

Chapter 2 represents an MD simulation of metal-polymer interfaces. The Au-SAM (self-assembly-monolayer) is used as the case for study. The temperature profiles at different temperatures are calculated, from which the ITC, thermal conductivity are derived. We also changed the molecule length to observe the change of the interfacial thermal properties with this factor. Then a TTM-MD simulation is conducted for comparison. This work serves as a start work for the major work in Chapter 3.

Chapter 3 focuses on investigating the e-p non-equilibrium thermal transport in a metal thin film sandwiched between two dielectric materials from a 1-D view. Clas-

sical Fourier calculations and semi-classical BTE simulations are performed for comparison. The previous LBM is extended to include TTM. The results show that the two methods present no difference in describing the thermal transport at such interfaces despite the fact that BTE can capture the finite size effect at system boundaries with thermal reservoirs while Fourier's Law cannot. It is also confirmed that in metallic films that is thin enough, electrons contribute very little to the thermal transport compared with phonons regardless of their bulk thermal conductivities. The critical thickness for metal films embedded in polymer matrix is also derived and its value is on the scale of several tens of nanometers.

Chapter 4 focuses on extending the previous TTM-MD tool developed by our group to include new physics at the metal-dielectric interfaces. A preliminary model for non-local e-p coupling is proposed and implemented. As a result electrons can couple to phonons within a certain distance, and metal electrons can interact with dielectric phonons near the interface. Results show that the non-local coupling has trivial effect on the thermal transport process in bulk metal, but the interfacial thermal transport has obvious change because of the additional thermal transport channel.

Chapter 5 features work on first-principles calculations of the e-p coupling properties in bulk Cu. The Eliashberg theory is introduced in this part which serves as the basis for the later works. The e-p coupling factor, e-p coupling spectrum and normalized coupling strength are calculated and presented. The e-p scattering rate is also calculated and is part of another work cited. Similar to Chapter 2, this chapter also serves as a start work and is the foundation for the major work in Chapter 6.

Chapter 6 focuses on investigating the non-local e-p coupling in metals. This is also the first study to present a first-principles calibration of this new physics based on solid theory foundations. Based on the DFT and Eliashberg theory mentioned above, new terms are defined and calculated to determine and describe the non-local e-p coupling phenomenon in Al, Cu and Ag. Results show that the non-local e-p coupling in Al is quite significant while weaker in Cu and Ag. And the effective distance of non-local e-p coupling is typically on the range of 1-2 lattice constants

(within 1 nm). This study also serves as a foundation for future investigation of non-local e-p coupling at metal-dielectric interfaces. The results are promising because the effective non-local coupling range is larger than the distance between surface atoms at typical metal-dielectric interfaces.

Chapter 7 aims at investigating the effect of phonon non-equilibrium thermal transport in metallic systems. TTM is extended to MTM with phonon-branch resolved e-p coupling strength, and p-p scattering is represented by each phonon branch's coupling to an averaged scattering lattice reservoir. A case study of thermal transport in laser-irradiated single-layer graphene demonstrates the significance of our model, as the non-equilibrium between phonons is strong and the predictions are significantly different from TTM. Our model is expected to be generally useful for predictions and simulations on many materials in a wide range.

Chapter 8 follows Chapter 7 and applies MTM to investigate the impact of phonon non-equilibrium thermal transport at interfaces. A case study of thermal transport across Si-Ge interfaces reveals that phonon thermal non-equilibrium will reduce the prediction of ITC, similar with the effect of e-p non-equilibrium at metal-dielectric interfaces.

Chapter 9 summarizes the work done during my PhD study and proposes the future work that can be oriented.

2. MOLECULAR DYNAMICS STUDY OF AU-SAM INTERFACES

2.1 Introduction

Recent developments in heat transfer area directs researcher's attention to metal-polymer interfaces. Among the wide variety of applications of metallic materials in electronic devices, metal thin films and small metal particles are playing an important role in multiple fields concerning heat transfer. The idea of adding a metal interlayer at the interface between two materials has been well recognized and developed in many studies, either to enhance or reduce energy transfer efficiency across the interface [14,64]. Similarly, inserting polymer between substrate surfaces as a "filler" material is also becoming more and more common to help adjust interfacial thermal properties. On the other hand, there have also been studies focused on metallic systems, or the metal matrix composites (MMC), which are used as thermal interface materials (TIM) to enhance interfacial thermal transport. In MMC, metal is often combined with another, often nonmetallic material, to create a novel composite material with desired properties [95]. For instance, it has been reported that polymer or dielectric matrix thermal conductivity can be significantly enhanced with metal particle inclusions [96]. In metal heat transfer process, not only phonons are involved, but also electrons [21]. Several works on formulating the two-temperature model (TTM) [31] BTE have already been carried out [63,64]. Combining their previous work with TTM, Miranda et al. [67] derived an analysis for the effective thermal conductivity of particulate composites with oriented spheroidal metallic particles embedded in a dielectric matrix. In their following study, extended models which can account for composites in the non-dilute limit were also derived later by means of crowding factor [69] and effective medium approximation (EMA) [68].

Both in MMC and systems with metal-polymer interlayers involve metal-polymer interfaces. Therefore it is important for us to obtain a clear understanding of the interfacial thermal physics and properties, which is necessary for providing us with guidance in system and device design. In this study an 1-D non-equilibrium molecular dynamics (NEMD) simulation is performed to predict the interfacial thermal conductance (ITC) of Au-SAM (self-assembly-monolayer) junction at low and high temperatures. The thermal conductivities are also derived from the temperature profiles. It serves as a foundation for the works in the next chapter.

2.2 Classical molecular dynamics simulation

2.2.1 Simulation details

Conventional MD simulation has been done on Au-SAM junction by previous studies, which provide reference for the structures and interatomic potentials. The details can be found in Ref. [97–99]. The simulation domain, as is shown in Fig. 2.1, features a “unit cell” of Au-SAM-Au-SAM-Au sandwich system, which has 32 SAM chains of $\text{S}-(\text{CH}_2)_8\text{-S}$ and contains 2624 atoms in the entire simulation domain. The cross section area of the unit cell is $17.304 \times 20.0 \text{ \AA}^2$, and the length is 134.25 \AA . The length is along the z axis, along which heat flow will be applied. For Au, its [111] direction is along z axis and SAM molecule chains grow along it as well. Periodic boundary conditions are applied in all three dimensions. The system is first relaxed under zero external pressure condition at 100 K for 0.3 ns, and then heat flux is added to perform nonequilibrium MD simulation. Two heat flows of $3.2 \times 10^{-8} \text{ W}$ are injected at the two ends of the unit cell and $6.4 \times 10^{-8} \text{ W}$ is subtracted from the center ensure energy conservation. The simulation runs for another 0.6 ns to get to a steady state, and the temperature profile is sampled from which we can calculate the thermal conductivity and ITC.

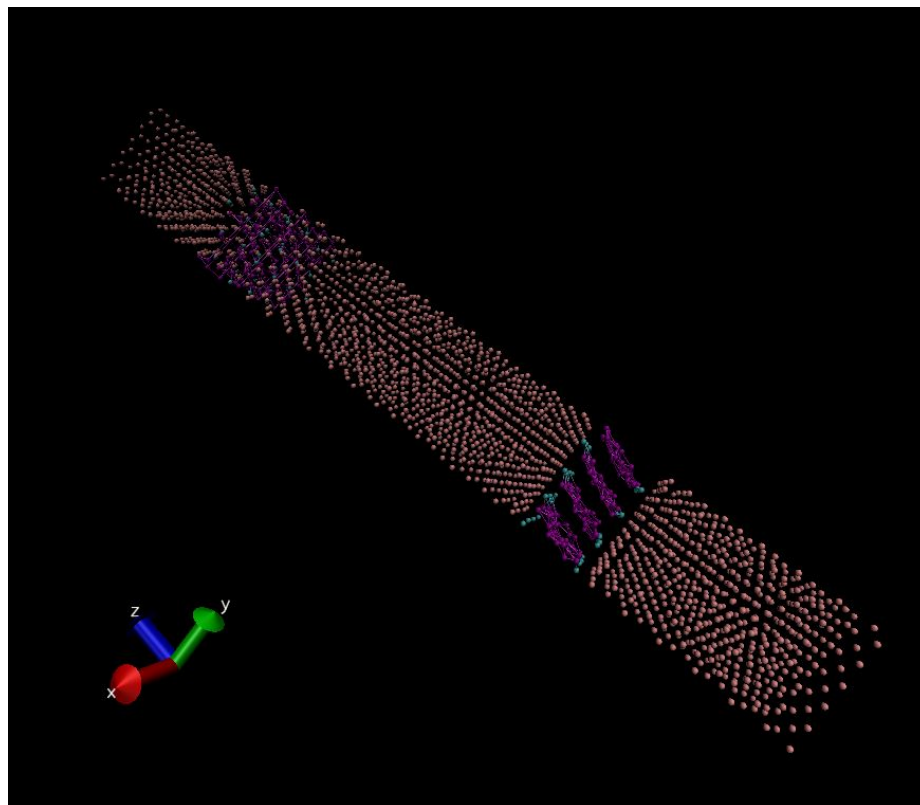


Figure 2.1. Visualization of the Au-SAM-Au-SAM-Au unit cell used in the NEMD simulation.

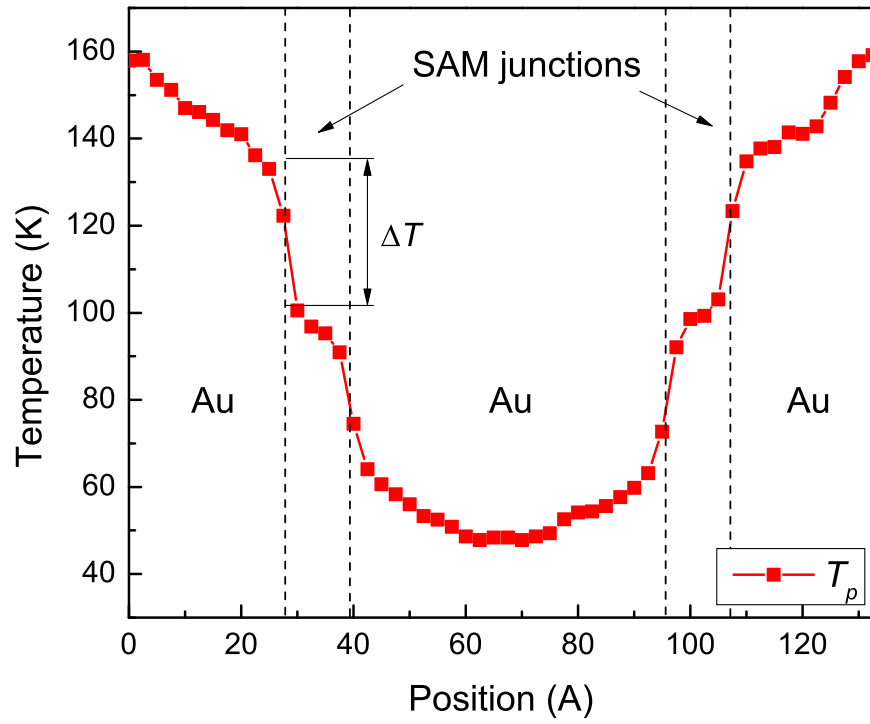


Figure 2.2. Temperature profile of the SAM-Au-SAM sandwich system in the MD simulation. The linear part of the profiles in each material is extrapolated to the interface to calculate the temperature jump.

Table 2.1.
ITC at Au/SAM junction with different molecule lengths

SAM molecule structure	ITC
S-(CH ₂) ₂ -S	253.81 \pm 41.93 MW/m ² K
S-(CH ₂) ₃ -S	377.35 \pm 31.48 MW/m ² K
S-(CH ₂) ₄ -S	310.50 \pm 39.26 MW/m ² K
S-(CH ₂) ₈ -S	292.28 \pm 17.71 MW/m ² K

2.2.2 Results

The temperature profile of the simulation domain is shown in Fig. 2.2. The ITC is defined as the ratio of the temperature jump ΔT at a single Au-SAM interface over the cross-interface heat flux J . Results show that the ITC of Au-SAM junction is 292.28 ± 17.71 MW/m²K, which agrees with previous works [99–101].

The length of the molecule is also modified to observe the how the ITC will change. Results are shown in Table. 2.1. It seems ITC changes with the length of SAM when it is short while it converges to a relatively steady value after the chains have more than 4 carbon atoms. The peak is at S-(CH₂)₃-S. The reason for this is that modifying the molecule length changes the vibration modes in the molecule, and S-(CH₂)₃-S has the best overlap with the phonon dispersion of Au, resulting in a relatively high ITC [102].

2.3 Two-temperature molecular dynamics simulation

In addition to conventional NEMD simulation, a comparative TTM-NEMD simulation is also conducted at room temperature. All the lattice properties are set to be the same with the previous simulation, while the electronic properties are set to ensure the electrical thermal conductivity is 313 W/mK. To make it more feasible to apply the TTM-MD code the simulation domain is also changed. The atoms in the

two ends of the unit cell are fixed to zero force and velocity so that the PBC is broken in the z direction, and heat flows in a monotonous direction in each unit cell. The new unit cell is set to have a length around 20 nm, with 4064 atoms inside it.

The temperature profile of the middle Au layer is shown in Fig. 2.3. At 300 K, the measured phonon ITC 349.3 ± 40.3 MW/m²K is higher than the previous result at 100 K, which again agrees with the results in Luo's work [99, 101]. This is because as temperature increases, the population of phonons available for interfacial thermal transport also increases. More phonons' participation result in a higher ITC. The electron-phonon (e-p) nonequilibrium introduces an additional temperature jump at the interface. The TBR R_{ep} due to e-p nonequilibrium is measured to be 1.1×10^{-9} m²K/W, which is comparable to the phonon coupling resistance R_{pp} of 2.9×10^{-9} m²K/W and should not be ignored. Therefore it justifies the necessity to use TTM-MD for a more accurate prediction in future works. The lattice thermal conductivity of Au is measured to be 6.37 W/mK while that of SAM molecule chain is 1.48 W/mK. It is noteworthy that this value is a little bit higher than that of common polymer materials. The reason is that these SAM molecule chains in the system are well aligned. The neat structure ensures that the phonon propagation is smooth and results in a reasonably high thermal conductivity. These results will be cited in the later chapters.

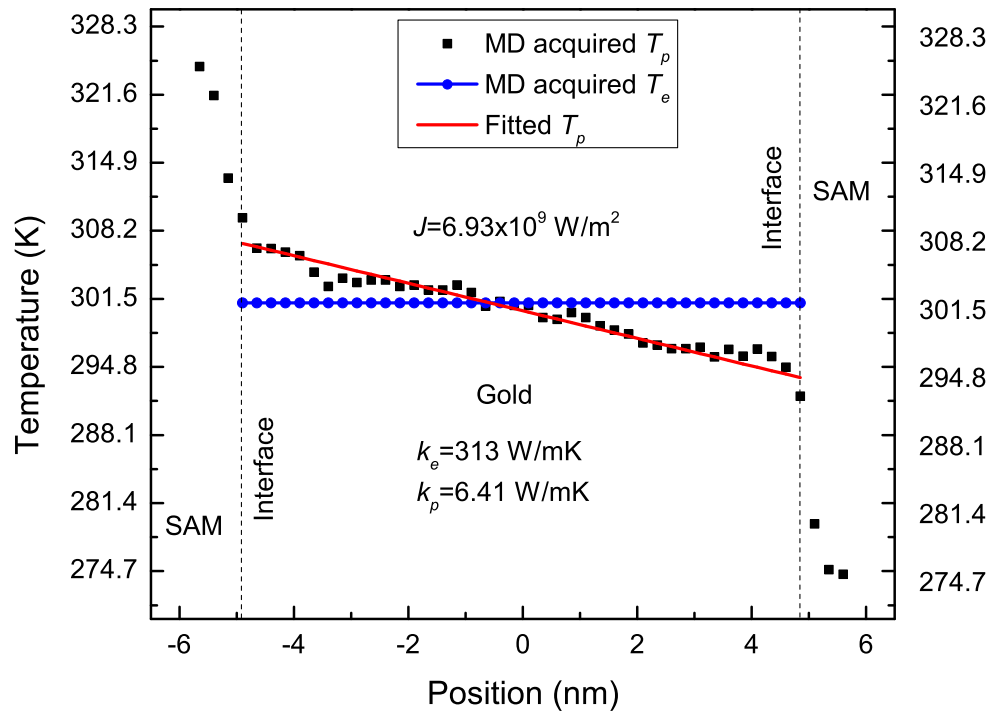


Figure 2.3. Temperature profile of the SAM-Au-SAM sandwich system in the TTM-MD simulation.

3. INVESTIGATION OF THERMAL TRANSPORT IN METAL THIN FILMS BASED ON TWO-TEMPERATURE MODEL

3.1 Introduction

Nanocomposite materials are widely used nowadays due to their outstanding properties which cannot be achieved by single-phase materials. They can be implemented in conditions where a high thermal conductivity is desired for heat dissipation, or where a low thermal conductivity is desired for large thermoelectric figure of merit ZT [103–106]. Besides, they play important roles in constructing controllable nanostructures, such as nanowires, nanotubes, and nanoparticles [107]. Many practical applications require us to optimize conflicting properties of materials to meet the demands. This could often be achieved by combining materials of different properties or adding one to another. Thus predicting the property of the composites and understanding the physics and mechanism become important. More than one hundred years ago, Maxwell already presented theoretical method for calculating the effective properties of particulate composites [108]. His pioneer work has served as basis for many following studies through these years.

There have been a series of theoretical studies on the effective properties of composite materials. The effective medium approximation (EMA) has been most widely applied [109–112]. Hasselman and Johnson developed a Maxwell-Garnett model based analysis for composites with different types of particle inclusions [113]. It was discovered that the particle size could affect the effective thermal conductivity. Benveniste [111] developed two methods to investigate particulate nanocomposites and obtained consistent results. Every et al. compared Maxwell-Garnett model and Bruggeman model and discussed the effect of particle size in the form of a length-unit parameter: Kapitza radius [114]. By combining EMA with their multiple scattering

theory, Nan et al. developed a model for arbitrary composites where they considered thermal boundary resistance (TBR) in the form of a coated layer [115]. Duan et al. derived an explicit expression for the effective thermal conductivity of heterogeneous media containing ellipsoidal inclusions. More recently they extended their previous study to include the effect of imperfect bond between the inclusions and the matrix as well [116, 117]. Yang and Chen [104] established the phonon Boltzmann transport equation (BTE) to investigate the phonon thermal conductivity of aligned nanowires embedded in a host semiconductor material. In this study the ballistic effect at nanoscale was emphasized. In following studies Yang et al. [118–120] implemented BTE and Monte Carlo (MC) simulation to analyze the thermal property of nanowire composites. Ravi [121] developed an analytical model for thermal conductivity in the longitudinal direction of two-dimensional nanocomposites made from aligned nanowires based on BTE, and obtained results in excellent agreement with Yang’s. Besides BTE studies, Minnich and Chen [122] included the size effect on thermal conductivity of nanoparticles by introducing a modified effective medium theory for nanocomposites with particle inclusions whose size is on the order or smaller than the phonon mean free path (MFP). And based on Minnich and Chen’s work, Miranda et al. [66] extended their theory for spheroidal inclusion and the results matched well with BTE numerical simulations.

However, in these models only phonons are considered, so they are not expected to work well for the metal-matrix composites (MMC) where electrons can make a significant difference [95]. It has been reported that polymer or dielectric matrix thermal conductivity can be significantly enhanced with metal particle inclusions [96]. In more recent studies, new methods and modified approaches are developed to take into account these effects. In metal heat transfer process, not only phonons are involved, but also electrons [21]. Several works on formulating the two-temperature model (TTM) [31] Boltzmann transport equations (BTE) have already been presented [63, 64]. Combining their previous work with TTM, Miranda et al. [67] derived an analysis for the effective thermal conductivity of particulate composites with oriented

spheroidal metallic particles embedded in a dielectric matrix. In their following study, extended models which can account for composites in the non-dilute limit were also derived later by means of crowding factor [69] and EMA [68].

The effect of particle sizes on the effective thermal conductivity has been investigated by several studies above [67, 114], but an explicit analytic solution considering electrons' effect has not been given. The critical radius has a significant effect on the effective thermal property, therefore developing a useful model for predicting r_c is practical for guiding us in choosing the materials and sizes of particles when synthesizing a composite material. Also, modern time domain thermal reflectance (TDTR) experiments often involve metal-dielectric multilayers, and it will be beneficial to develop analytical relations that are easy to use. In this study we combine molecular dynamics (MD) with TTM-Fourier calculations to predict the critical thickness L_c in 1D for metal particles embedded in polymer matrix. A general solution to TTM that is applicable regardless of the size of the system is derived. SAM-Au-SAM case study is presented as an example and TTM-MD simulation is performed to predict the thermal properties for the inputs of the calculation. Based on the mathematical equations and thermal circuit analysis, we propose a new approach to analyze the thermal conduction in metal thin films sandwiched between dielectric layers, which is more intuitive in explaining experimental and simulation results than previous models under certain conditions [24]. Finally, several factors including the thermal conductivity, TBR and electron-phonon (e-p) coupling that can affect L_c are discussed.

3.2 Theory

Generally, metals have higher thermal conductivity than polymers. Therefore when metal particles are added to polymer matrix, the thermal conductivity of the replaced part is expected to be enhanced. However TBR is also introduced at the same time. A 1D representation of this process is illustrated in Fig. 3.1. The total resistance of the new composite is determined by the competition of the high

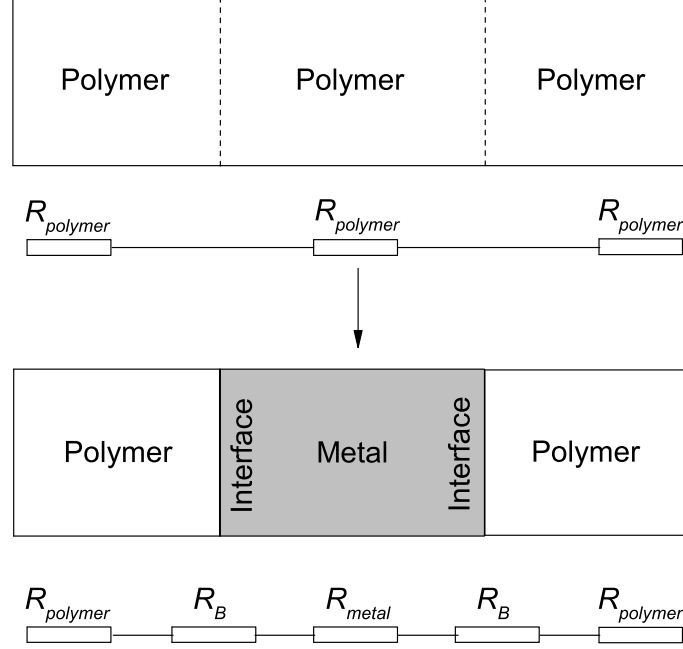


Figure 3.1. The schematic of a 1D metal-polymer composite, where a polymer layer is replaced with metal. Hence, the middle layer polymer conduction resistance is replaced by metal layer conduction resistance and the thermal boundary resistance at the two interfaces.

thermal conductivity of the replaced layer and the introduced TBR. Defining the total resistance introduced by the metal middle layer as $R_{intro} = R_{metal,c} + 2R_B$, the resistance change in Fig. 3.1 can be expressed as:

$$\Delta R = R_{intro} - R_{poly,c}. \quad (3.1)$$

Here R_B is the TBR which is related to the material properties such as lattice mismatch, etc. $R_{metal,c}$ and $R_{poly,c}$ refer to the conduction resistance of metal and polymer respectively, which depend on the middle layer thickness and their thermal conductivities. Therefore ΔR also varies with these factors. In order to obtain a quantitative analysis of the relationship between ΔR and the middle layer thickness, expressions for the resistances in Eq. (3.1) need to be derived.

3.2.1 A general solution to two-temperature model equations for a metal thin film sandwiched between two dielectrics

The interfaces in Fig. 3.1 are the metal/nonmetal interfaces. In metals, thermal transport involves both phonons and electrons. We apply the two-temperature model [24, 31] for analysis, where electrons and phonons are depicted as two interacting subsystems with their own temperatures. Their interaction strength is described by the coupling factor G_{ep} . If we ignore all the external factors such as laser heating, etc., the steady-state governing equations are:

$$\begin{aligned} k_e \frac{\partial^2 T_e}{\partial x^2} - G_{ep}(T_e - T_p) &= 0, \\ k_p \frac{\partial^2 T_p}{\partial x^2} + G_{ep}(T_e - T_p) &= 0. \end{aligned} \quad (3.2)$$

Here T , k denote the temperature and thermal conductivity respectively, e and p are index for electron and phonon respectively. In dielectric materials, usually the electrons' effect can be neglected compared with phonons' effect [24]. At the interface, the cross-interface e-p interaction may also be ignored if the temperature difference is not large (< 1000 K) [70]. Based on the above assumptions, only phonons can transfer energy across the interface while electrons cannot. In a polymer/metal/polymer sandwich system as illustrated in Fig. 3.2, the boundary conditions are:

$$\begin{aligned} -k_{poly} \frac{\partial T_{poly}}{\partial x} \Big|_{x=-\frac{L}{2}^-} &= -k_p \frac{\partial T_p}{\partial x} \Big|_{x=-\frac{L}{2}^+} = J, \\ -k_{poly} \frac{\partial T_{poly}}{\partial x} \Big|_{x=\frac{L}{2}^+} &= -k_p \frac{\partial T_p}{\partial x} \Big|_{x=\frac{L}{2}^-} = J, \\ -k_e \frac{\partial T_e}{\partial x} \Big|_{x=-\frac{L}{2}^+} &= -k_e \frac{\partial T_e}{\partial x} \Big|_{x=\frac{L}{2}^-} = 0, \end{aligned} \quad (3.3)$$

where J is the heat flux, k_{poly} is the thermal conductivity of polymer. Different boundary conditions cause non-equilibrium between the two energy carriers in the metal. As is illustrated in Fig. 3.2, electrons and phonons have strong non-equilibrium near the interface where their temperatures deviate from each other. This will render an extra interfacial resistance in addition to the phonon-phonon coupling resistance. As a result the total TBR consists of two parts: $R_B = R_{pp} + R_{ep}$.

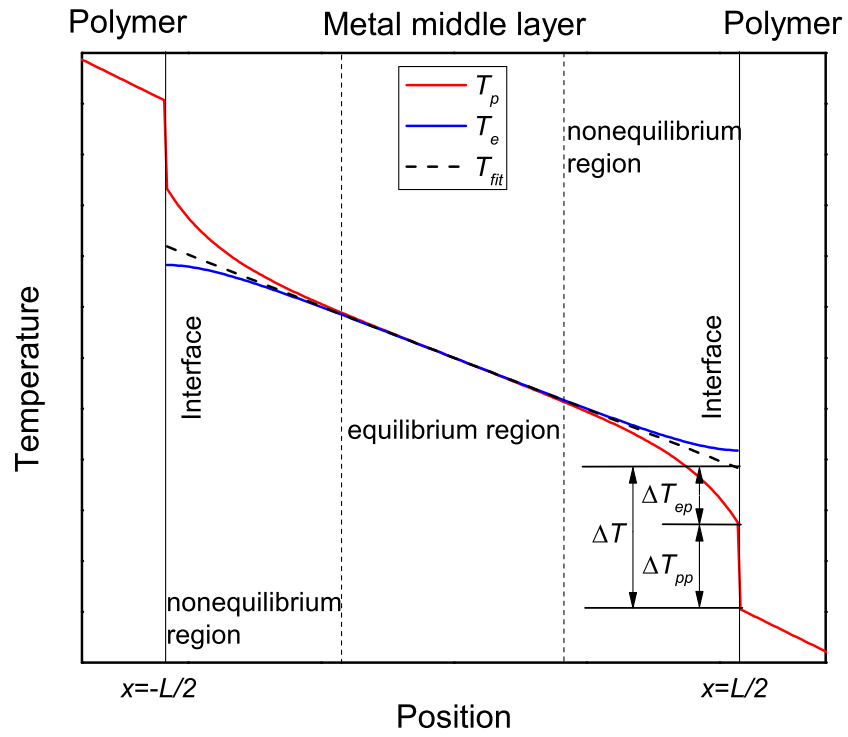


Figure 3.2. Temperature distribution in a polymer-metal-polymer sandwich system. In the metal middle layer both electrons and phonons are considered while in the polymer substrates only phonons are considered.

R_{pp} can be acquired by the several approaches such as acoustic mismatch model (AMM), diffuse mismatch model (DMM) and MD simulations [22, 83, 123]. It can be treated as a relatively constant value at a specific temperature. Therefore only R_{ep} needs to be derived. Combining Eq. (3.2) and (3.3), we can obtain an expression for the temperature profile in the metal:

$$\begin{aligned} T_e &= T_{mid} - \frac{J}{k_p + k_e}x + \frac{k_p}{k_p + k_e} \frac{Jd \sinh(\frac{L}{2d})}{k_p \sinh(\frac{L}{d})} \cdot 2 \sinh(\frac{x}{d}), \\ T_p &= T_{mid} - \frac{J}{k_p + k_e}x - \frac{k_e}{k_p + k_e} \frac{Jd \sinh(\frac{L}{2d})}{k_p \sinh(\frac{L}{d})} \cdot 2 \sinh(\frac{x}{d}), \end{aligned} \quad (3.4)$$

where

$$d = \frac{1}{\sqrt{G_{ep}(\frac{1}{k_e} + \frac{1}{k_p})}} \quad (3.5)$$

is the e-p coupling length. And T_{mid} is the temperature at $x = 0$, which is also the center point of the metal middle layer where electrons and phonons reach thermal equilibrium. The total resistance from $x = 0$ to $x = \frac{L}{2}^+$ can then be expressed as:

$$\frac{T_{mid} - T_R}{J} = \frac{\frac{L}{2}}{k_e + k_p} + \frac{T_p|_{x=\frac{L}{2}^-} - T_{poly}|_{x=\frac{L}{2}^+}}{J} + \frac{k_e}{k_p + k_e} \frac{d}{k_p} \tanh(\frac{L}{2d}). \quad (3.6)$$

Here T_R is the temperature of the polymer at $x = \frac{L}{2}$. Eq. (3.6) has the form of a serial thermal circuit. Observing the right side of Eq. (3.6), the first term is the definition of the metal conduction resistance from $x = 0$ to $x = \frac{L}{2}$, while the second and third term together is the TBR $R_B = R_{pp} + R_{ep}$. By noticing the fact that the second term is exactly the definition of $R_{pp} = \Delta T_p/J$, we can obtain an expression for R_{ep} :

$$R_{ep} = \frac{1}{(G_{ep}k_p)^{\frac{1}{2}}} \left(\frac{k_e}{k_e + k_p} \right)^{\frac{3}{2}} \tanh\left(\frac{L}{2d}\right). \quad (3.7)$$

Eq. (3.7) is generally applicable regardless of the metal film thickness. If we apply the infinite large-system limit, R_{ep} recovers the expression in Wang's work [24].

3.2.2 The critical thickness L_c

With expressions for all the resistances in Eq. (3.1), ΔR can be expressed as:

$$\Delta R = \frac{2}{(G_{ep}k_p)^{\frac{1}{2}}} \left(\frac{k_e}{k_e + k_p} \right)^{\frac{3}{2}} \tanh\left(\frac{L}{2d}\right) + \frac{2}{h_{pp}} + \frac{L}{k_e + k_p} - \frac{L}{k_{poly}}, \quad (3.8)$$

where h_{pp} is the phonon thermal boundary conductance (TBC) which is the inverse of R_{pp} .

If we want to improve the heat conduction in the new composite material, ΔR must be negative so that the total resistance decreases. Observing the first-order derivative of ΔR , it can be shown that:

$$\frac{d \Delta R}{dL} < \frac{2}{(G_{ep}k_p)^{\frac{1}{2}}} \left(\frac{k_e}{k_e + k_p} \right)^{\frac{3}{2}} + \frac{1}{k_e + k_p} - \frac{1}{k_{poly}}. \quad (3.9)$$

For most metals, the value of $k_e + k_p$ is usually greater than 100 W/mK, and G_{ep} is on the order of 1×10^{16} W/m³K, while k_{poly} for most common polymer materials is smaller than 10 W/mK. As a result the right side of Eq. (3.9) is always negative, which means ΔR decreases monotonically as L increases, from its maximum value of $2/h_{pp}$ at $L = 0$. The critical thickness L_c is defined as the value where ΔR crosses zero, and L has to be larger than L_c to result in a negative ΔR . Therefore:

$$\frac{2}{(G_{ep}k_p)^{\frac{1}{2}}} \left(\frac{k_e}{k_e + k_p} \right)^{\frac{3}{2}} \tanh\left(\frac{L_c}{2d}\right) + \frac{2}{h_{pp}} + \frac{L_c}{k_e + k_p} - \frac{L_c}{k_{poly}} = 0. \quad (3.10)$$

It is noteworthy that L_c only exists when $k_{poly} < k_e + k_p$, which is true for most materials. The first term in Eq. (3.10) makes it difficult to get an explicit analytic solution for L_c . However, we can simplify the equation by taking two extreme limits: 1) If G_{ep} is very small, which is the case electrons and phonons have very weak coupling:

$$\begin{aligned} d &= \frac{1}{\sqrt{G_{ep}(\frac{1}{k_e} + \frac{1}{k_p})}} \rightarrow \infty, \frac{L_c}{2d} \rightarrow 0, \\ \tanh\left(\frac{L_c}{2d}\right) &\rightarrow \frac{L_c}{2d}. \end{aligned} \quad (3.11)$$

The first term in Eq. (3.10) evolves as:

$$\frac{2}{(G_{ep}k_p)^{\frac{1}{2}}} \left(\frac{k_e}{k_e + k_p} \right)^{\frac{3}{2}} \tanh\left(\frac{L_c}{2d}\right) = 2d \frac{k_e}{k_p(k_e + k_p)} \frac{L_c}{2d} = \frac{k_e L_c}{k_p(k_e + k_p)}. \quad (3.12)$$

From Eq. (3.10) & (3.12), L_c is expressed as:

$$L_c = \frac{\frac{2}{h_{pp}}}{\frac{1}{k_{poly}} - \frac{1}{k_p}}. \quad (3.13)$$

It is the same result when electrons are not involved. In fact, if $L_c/d < 1$, which is usually the case for metals with weak e-p coupling like gold ($L_c/d = 0.5$), the above expression is still approximately valid, with an error within 10%.

2) If G_{ep} is very large, which is the case that electrons and phonons have very strong coupling:

$$d = \frac{1}{\sqrt{G_{ep}(\frac{1}{k_e} + \frac{1}{k_p})}} \rightarrow 0, \frac{L_c}{2d} \rightarrow \infty, \quad (3.14)$$

$$\tanh(\frac{L_c}{2d}) \rightarrow 1.$$

The first term in Eq. (3.10) evolves as:

$$\frac{2}{(G_{ep}k_p)^{\frac{1}{2}}} \left(\frac{k_e}{k_e + k_p}\right)^{\frac{3}{2}} \tanh(\frac{L_c}{2d}) = 2d \frac{k_e}{k_p(k_e + k_p)} = 0. \quad (3.15)$$

Then:

$$L_c = \frac{\frac{2}{h_{pp}}}{\frac{1}{k_{poly}} - \frac{1}{k_p} \frac{1}{1+r_{ep}}}, r_{ep} = \frac{k_e}{k_p}. \quad (3.16)$$

This is the case when electrons and phonons are in perfect equilibrium, indicating electrons fully contribute to thermal transport. In fact, if $L_c/d > 3$, which is usually the case for metals with strong e-p coupling like nickel ($L_c/d = 4.1$), the above expression is still approximately valid, with an error of 10%.

3) When L_c/d is between 1 and 3, the above two simplifications can no longer give accurate results, and we will need to numerically solve Eq. (3.10) to get an accurate solution. For a specific pair of materials, one can choose one from the above equations with h_{pp} , k_p and k_{poly} to estimate L_c first, and then check if L_c/d falls in the corresponding range. If so then the approximation is valid, otherwise a more accurate calculation is required.

3.2.3 Two-temperature lattice Boltzmann method

Based on the TTM governing equations, Eq. (1.22) is extended to its TTM form:

$$\begin{aligned} \frac{\partial e_p}{\partial t} + \mathbf{v} \cdot \Delta e_p &= \frac{e_p^0 - e_p}{\tau} + Q_{ep}, \\ \frac{\partial e_e}{\partial t} + \mathbf{v} \cdot \Delta e_e &= \frac{e_e^0 - e_e}{\tau} - Q_{ep}, \end{aligned} \quad (3.17)$$

The discretized governing equations are:

$$\begin{aligned} e_{p,i}(x + \Delta x, t + \Delta t) &= (1 - W_i)e_{p,i}(x, t) + W_i e_p^0(x, t) + Q_{ep}, \\ e_{e,i}(x + \Delta x, t + \Delta t) &= (1 - W_i)e_{e,i}(x, t) + W_i e_e^0(x, t) - Q_{ep}, \end{aligned} \quad (3.18)$$

here i is the index for energy propagation directions. $W_i = \Delta t/\tau$ is a weight factor determining the contribution of ballistic and diffusive heat transport. e^0 equals $\sum e_i/d$. d is the dimension. The boundary conditions at the interface are described by phonon transmission rate based on DMM theory [124], and electrons are as well insulated:

$$\begin{aligned} e_{pf,2}(x_0 + \frac{\Delta x_2}{2}, t) &= t_{12}e_{pf,1}(x_0 + \frac{\Delta x_1}{2}, t) + r_{21}e_{pb,2}(x_0 - \frac{\Delta x_2}{2}, t) + Q_{ep}(x_0 + \frac{\Delta x_2}{2}, t), \\ e_{pb,1}(x_0 - \frac{\Delta x_1}{2}, t) &= t_{21}e_{pb,2}(x_0 - \frac{\Delta x_2}{2}, t) + r_{12}e_{pf,1}(x_0 + \frac{\Delta x_1}{2}, t) + Q_{ep}(x_0 - \frac{\Delta x_1}{2}, t), \end{aligned} \quad (3.19)$$

where t_{12} and r_{12} are the transmission and reflection rate from material 1 to material 2 respectively, Δx_1 and Δx_2 are the unit cell lengths in material 1 and 2 respectively, e_{pf} and e_{pb} refer to the phonon energy density flowing along and opposite to the direction of heat flux respectively, and x_0 is the position where the interface between material 1 and 2 is located at. Therefore the original LBM is extended to become the TTM-LBM which includes the electron energy transfer channel.

3.3 SAM-Au-SAM Case Study

In this section, we will present a case study of a gold thin film sandwiched between aligned SAM chains. The Au-SAM interface has been investigated by several recent studies which could provide benchmarks for our calculations [97–99]. A TTM-MD simulation is performed first to predict the necessary thermal properties, and then a TTM-Fourier calculation is presented based on the equations introduced in the previous section, with a comparative study based on TTM-BTE using consistent input properties.

3.3.1 Two-temperature molecular dynamics simulations

The TTM-Fourier and TTM-BTE calculations require the following thermal properties as known inputs: the phonon TBC h_{pp} , the thermal conductivity k and the e-p coupling factor G_{ep} . A TTM-MD simulation of a Au-SAM-Au-SAM-Au multilayer system is performed to predict these values [18,24]. The total length of the simulation domain is 134.25 Å, with a cross-section area of 17.304×20.0 Å² or 12 gold atoms in the (111) plane of the face-centered cubic (FCC) unit cell. 16 SAM molecules form the junction between each 2 adjacent gold layers. As a result, there are 2624 atoms in the domain. Reference of the structure and interatomic potentials used can be found in Ref. 97–99. The electronic properties of gold are taken as the common values at room temperature. The system is first relaxed under zero external pressure condition at 300 K for 0.3 ns, and then a heat flow of 3.2×10^{-8} W is imposed in the direction which is perpendicular to the interfaces. The non-equilibrium MD simulation runs for another 0.6 ns to let the system get to a steady state. The final temperature profile zoomed at the middle gold layer is shown in Fig. 3.3. From the results, h_{pp} is 349.3 ± 40.3 MW/m²K. Although our h_{pp} agrees reasonably well with previous theoretical predictions [99], they are significantly higher than reported experimental data such as Refs. 125 and 126. This is probably because, for example, in simulations the hydrogen atoms are incorporated into their carbon or sulfur backbones and are not simulated explicitly; also the interfaces in simulations are perfectly bonded. Here we present our results using the theoretical h_{pp} , while the impact of lower h_{pp} (or higher R_{pp}) from experiments on L_c is discussed in Section IV.B. The lattice thermal conductivity of Au is found to be 6.41 W/mK while that of SAM molecule chain ranges from 0.9 W/mK to 2.4 W/mK, which also agree with previous literatures [127,128]. It is noteworthy that this value is a little bit higher than that of common polymer matrix. The reason is that these SAM molecule chains in the system are well aligned. The neat structure ensures that the phonon propagation is smooth and results in a reasonably high thermal conductivity.

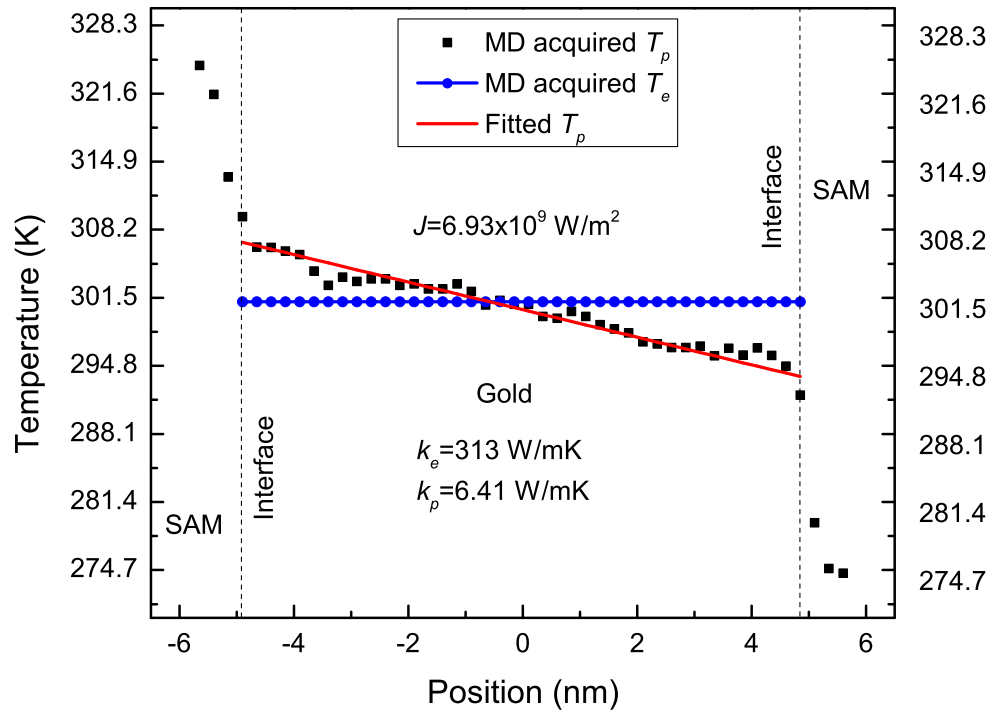


Figure 3.3. The temperature profile of the Au-SAM-Au-SAM-Au multi-layer system zoomed at the middle layer from the TTM-MD simulation.

Table 3.1.
Thermal Properties used in TTM-Fourier Calculation

Thermal Property	Value
h_{pp}	350 MW/m ² K
$k_{polymer}$	1.48 W/mK
k_e	313 W/mK
k_p	6.41 W/mK
G_{ep}	2.8×10^{16} W/m ³ K

3.3.2 Two-temperature model Fourier calculations

We have developed equations for estimating L_c in the previous section. However, usually a more accurate result without approximations is desired. Then we need to go back to Eq. (3.10) and acquire the solution through numerical methods. The detailed parameters used for the Au-SAM-Au calculation are listed in Table 3.1. Based on the TTM-MD simulation results, we assign h_{pp} as 350 W/m²K for convenience. For the thermal conductivity of polymer, we use our own averaged value of 1.48 W/mK, which is reasonable compared with Chen's result of 2.081 W/mK [128]. $k_e=313$ W/mK and $k_p=6.41$ W/mK are the bulk thermal conductivities of gold. $G_{ep}=2.8 \times 10^{16}$ W/m³K is a commonly used value for gold [129]. The trend of ΔR v.s. metal film thickness is illustrated in Fig. 3.4. ΔR decreases monotonically with the film thickness. And when $\Delta R = 0$, which means the systems resistance is unchanged, we obtain the critical thickness $L_c = 10.8$ nm. By comparing with the result $L_c=10.96$ nm given by Eq. (3.13), we can see that Eq. (3.13) provides an excellent approximation for metals with weak e-p coupling like gold.

The TTM-Fourier method's prediction of the temperature profile of the entire system is illustrated in Fig. 3.5. The metal film thickness is chosen as the critical thickness for SAM-Au-SAM system. The electrons and phonons are in non-equilibrium

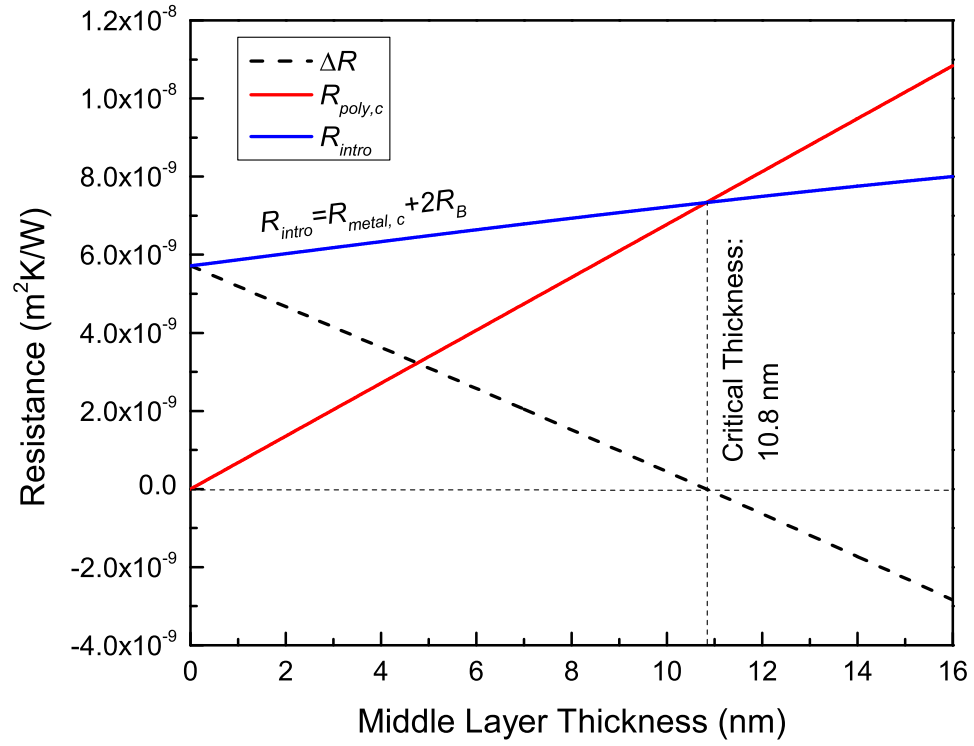


Figure 3.4. R_{intro} , $R_{poly,c}$ and ΔR as a function of the metal layer thickness in the SAM-Au-SAM sandwich system predicted by TTM-Fourier calculation.

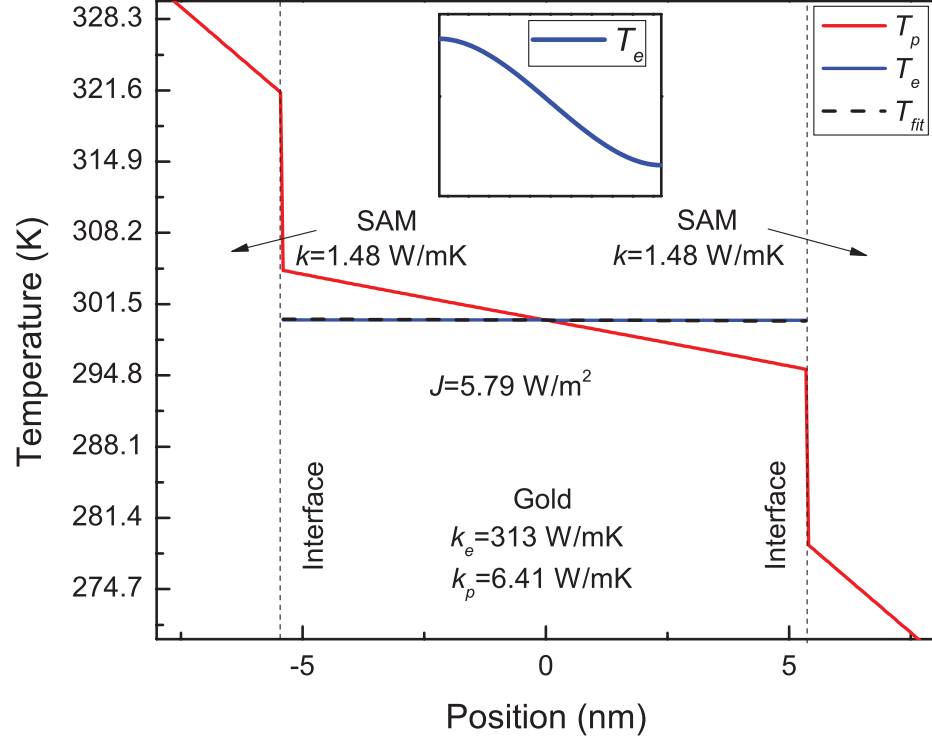


Figure 3.5. Temperature profile of a SAM-Au (10.8nm)-SAM sandwich system predicted by TTM-Fourier calculation. A zoom in profile of the electron temperature is shown.

except at the middle point. Therefore it justifies the necessity to use our more general Eq. (3.7) for R_{ep} . The fitted temperature is almost identical to electrons' temperature, which has a very flat profile, indicating a small electronic contribution to the overall thermal conduction. This agrees with Li's result which shows that in very thin metal films phonons dominate the energy transport process [37].

A closer observation of R_{intro} v.s. L also reveals the fact that electrons hardly contribute to the thermal conduction in a thin gold film. As is illustrated in Fig. 3.6, at a thickness smaller than 20 nm R_{intro} mainly comes from R_{pp} , while its increasing trend is mainly determined by R_{ep} 's increase with L . The gradient of R_{intro} is very close to $1/k_p$. This indicates the R_{intro} curve is almost identical to the straight line with the expression of $R(L) = 2R_{pp} + L/k_p$, which means the effective thermal

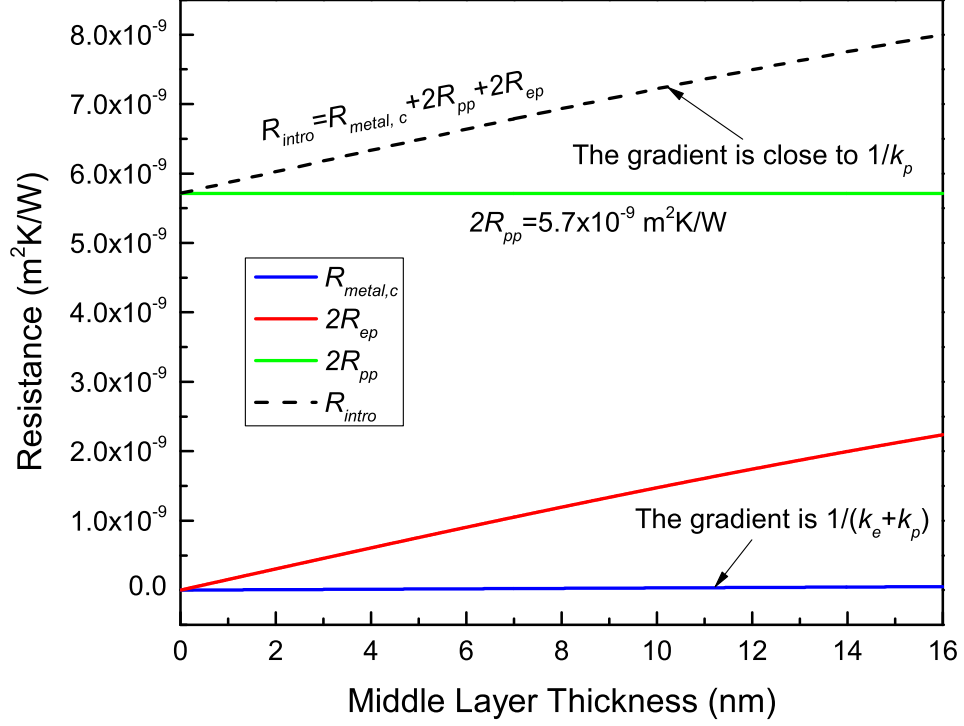


Figure 3.6. Components of the total resistance of the gold film. It is composed of three parts: 1) film conduction resistance $R_{metal,c}$ 2) resistance due to interfacial phonon coupling R_{pp} 3) resistance due to e-p non-equilibrium near the interface R_{ep} . It is revealed that $R_{metal,c}$ comprises a very small part. The majority of the resistance comes from R_{pp} and R_{ep} .

transport process is the same as if there is only phonon participation. This stimulates our proposal for a new analytic approach for thermal conduction in sandwiched metal thin films, which will be discussed in the following section.

3.3.3 Two-temperature model Boltzmann transport equation calculations

We also conducted a comparative TTM-BTE calculation for comparison. The input parameters for LBM simulation are listed in Table. 3.2. The phonon group velocity for SAM is originally chosen as 2300 m/s, which is the phonon group velocity of polythene [130]. We modified it a bit to 2620 m/s, which is twice as large as phonon

Table 3.2.
Thermal Properties used in the TTM-BTE calculation

Thermal Property	Value
$v_{g,gold}$	1310 m/s
$v_{f,gold}$	1.4×10^6 m/s
$v_{g,SAM}$	2620 m/s
$C_{p,gold}$	2.4897×10^6 J/m ³ K
$C_{e,gold}$	0.0203×10^6 J/m ³ K
$C_{p,SAM}$	0.3755×10^6 J/m ³ K
$\tau_{p,gold}$	6.0 ps
$\tau_{e,gold}$	0.03 ps
$\tau_{p,polymer}$	2.3 ps

group velocity of gold, to simplify LBM calculation. In actual calculation, $v_{g,gold}$, $v_{g,SAM}$ and $v_{f,gold}$ are corrected by a factor of 0.5 due to the dimension reduction from 3D to 1D [131]. $C_{e,gold}$ is approximated using $C_e = 67.6 \times T$, where T is the temperature [129]. And $C_{p,SAM}$ is acquired from Ref. 130. The relaxation times are acquired from common material properties and are adjusted to match the properties used in TTM-Fourier calculation according to the thermal conductivity kinetic theory:

$$k = \frac{1}{d} v_g \Lambda C, \quad (3.20)$$

where d is the dimension and $\Lambda = v_g \tau$ is the phonon MFP. The simulation is conducted controlling the heat flux going through the system: the heat flux is set to the same used in the TTM-Fourier calculations.

The temperature profiles for TTM-BTE is shown in Fig. 3.7. The temperature profiles are almost identical with that of TTM-Fourier calculations with differences smaller than 1% in the entire simulation domain. As a result, the critical thicknesses calculated are also approximately the same. For a SAM-Au-SAM system with the input parameters as listed above, the critical thickness is approximately 10.6-10.8 nm.

3.4 Discussion

3.4.1 Factors affecting L_c

In this section we discuss several factors that can affect L_c based on Eq. (3.10):

1) R_{pp} , 2) G_{ep} , 3) k_p , 4) k_{poly} , and 5) r_{ep} .

1) R_{pp} comprises the most part of TBR when the metal film is as thin as ~ 10 nm. A larger R_{pp} will increase TBR thus increasing the critical thickness. For example, if one uses the experimentally determined R_{pp} [125, 126] which is much higher than the one we used in our previous calculations, the resulting L_c will be larger than 10.8 nm, but the general trend is the same and our conclusions are still valid.

2) G_{ep} measures the e-p coupling strength and is directly related to R_{ep} . A larger

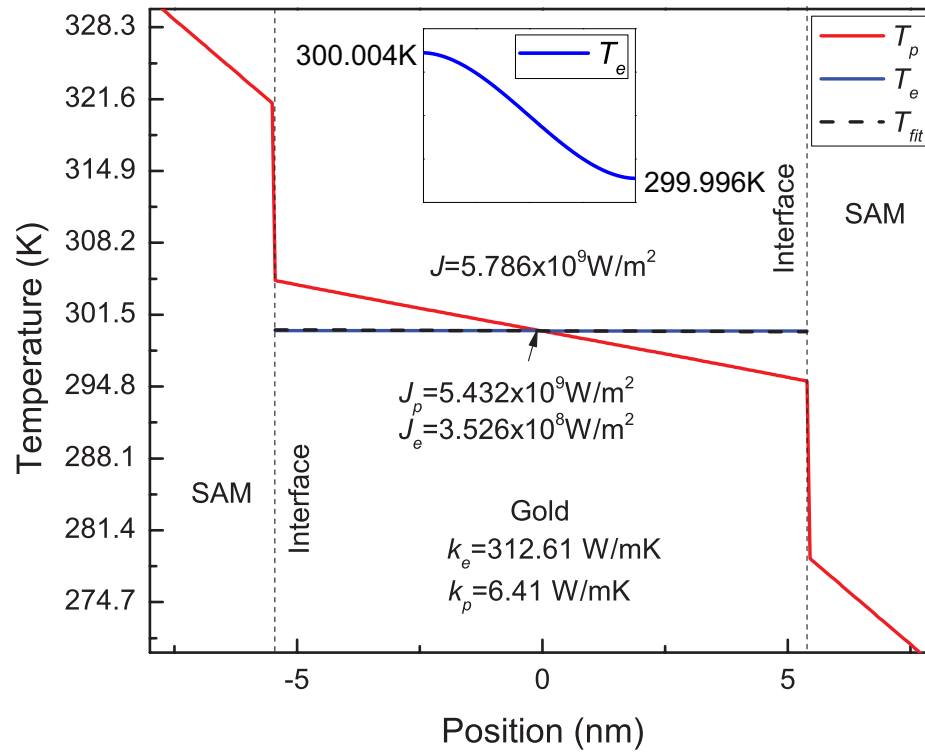


Figure 3.7. Temperature profile of a SAM-Au (10.8 nm)-SAM sandwich system predicted by TTM-BTE calculation. Calculation is conducted to match the heat flux used in TTM-Fourier calculation. A zoom in profile of the electron temperature is shown. The resulting temperature profile matches that of TTM-Fourier calculation.

G_{ep} will render a smaller R_{ep} and thus a smaller TBR, resulting in a smaller critical thickness.

3) k_p dominates the thermal transport process in thin films as mentioned above. As a result it is almost identical to the effective thermal conductivity k_{eff} . When k_p increases, k_{eff} increases, R_{ep} will decrease according to Eq. (3.7), hence the critical thickness will be smaller.

4) k_{poly} is the thermal conductivity of the polymer matrix. A larger k_{poly} will increase the difficulty for the metal film to compensate for the resistance increase due to introduced TBR after the replacement. Therefore larger k_{poly} will result in larger L_c .

5) r_{ep} , which is the ratio of k_e over k_p , can affect R_{ep} as well as the thermal conductivity of the metal film. If we keep k_p as fixed, larger r_{ep} will increase $k_e + k_p$ and also change R_{ep} (whether it will increase or decrease depends). Generally a larger k_e is beneficial and will result in a smaller L_c . The effect is more significant if the values of k_e and k_p are comparable which means r_{ep} is around 1, especially for large G_{ep} .

When we choose the filler material to add in the polymer matrix, two characteristic properties are G_{ep} and k_e . Here we plot G_{ep} and k_e 's effect on L_c in Fig. 3.8 on an arbitrary SAM-Au-SAM system to gain a more straight-forward insight. k_p is fixed at the value of gold's lattice thermal conductivity, and k_e is represented by the normalized parameter r_{ep} . L_c decreases with larger G_{ep} and larger k_e . However k_e 's effect is only significant when k_e is small and the impact vanishes as k_e increases. However metals usually have much larger k_e than k_p , so r_{ep} is not so significant in controlling L_c .

3.4.2 The effective thermal conductivity of the sandwiched metal layer

So far we have assumed the thermal conductivity of the metal layer is still $k_e + k_p$, while we lump R_{ep} into the interface resistance. This is commonly done for a single interface between semi-infinite metal and dielectric [24, 31], since electrons and phonons are in equilibrium in nearly the entire metal except for the short cooling

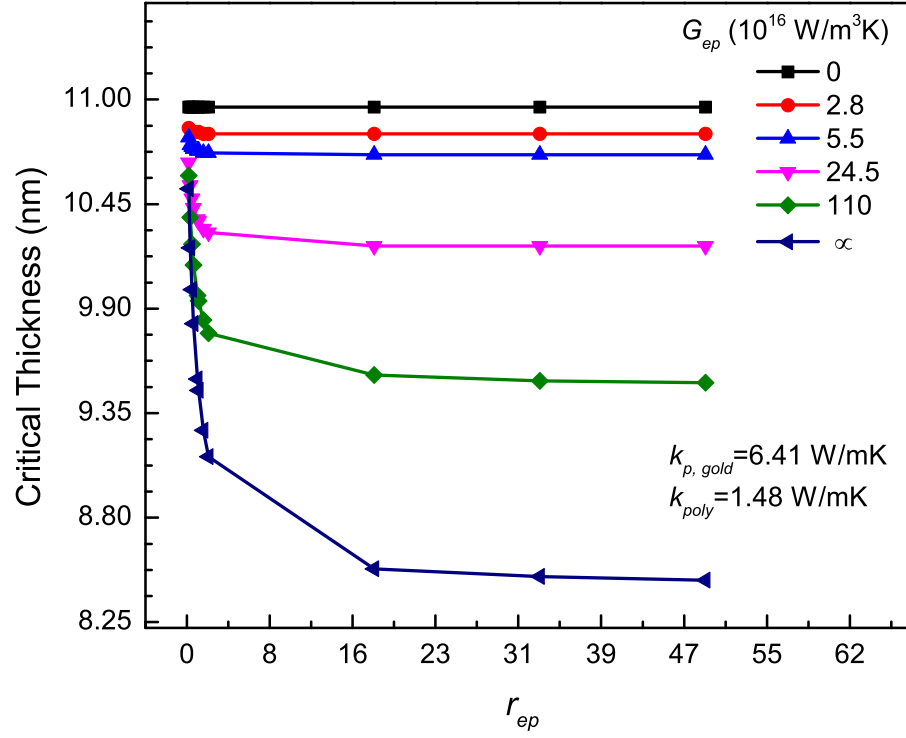


Figure 3.8. Two main factors that can affect the critical thickness L_c : G_{ep} and k_e . It is revealed that G_{ep} has a significant effect on L_c . L_c is sensitive to k_e as k_e is small (small r_{ep}) while it becomes insensitive as k_e becomes large.

region near the interface. However, it is not so intuitive for the sandwiched thin film here since electrons and phonons are in strong non-equilibrium except for the mid-plane, and the thermal conduction is dominated by phonons. Therefore, it is more intuitive to start the metal layer as a phonon-only system, and investigate what effects the electrons will bring. Therefore here we present an alternative analysis where we define a new effective thermal conductivity of the metal layer while not assuming it to be $k_e + k_p$ anymore.

From Eq. (3.7), we can express R_{intro} as follows:

$$R_{intro} = 2R_{ep} + R_{metal,c} + 2R_{pp} = \frac{2}{(G_{ep}k_p)^{\frac{1}{2}}} \left(\frac{k_e}{k_e + k_p} \right)^{\frac{3}{2}} \tanh\left(\frac{L}{2d}\right) + \frac{L}{k_e + k_p} + 2R_{pp}. \quad (3.21)$$

Previously we have treated R_{ep} as part of R_B . Here, we view the metal layer primarily as a phonon system, so we only include R_{pp} in R_B , while lump R_{ep} into the conduction resistance of the metal layer R_{eff} . Therefore:

$$R_{eff} = 2R_{ep} + R_{metal} = \frac{2}{(G_{ep}k_p)^{\frac{1}{2}}} \left(\frac{k_e}{k_e + k_p} \right)^{\frac{3}{2}} \tanh\left(\frac{L}{2d}\right) + \frac{L}{k_e + k_p}, \quad (3.22)$$

and then define the effective thermal conductivity of the metal film as:

$$k_{eff} = \frac{L}{R_{eff}} = \frac{k_e + k_p}{1 + \frac{2k_e}{L} \left[\frac{k_e}{G_{ep}k_p(k_e + k_p)} \right]^{\frac{1}{2}} \tanh\left(\frac{L}{2d}\right)}. \quad (3.23)$$

The corresponding thermal circuit is shown in Fig. 3.9. And we can easily find that:

$$\begin{aligned} k_{eff} &\rightarrow k_p, \text{ when } L \rightarrow 0 \text{ or } G_{ep} \rightarrow 0, \\ k_{eff} &\rightarrow k_e + k_p, \text{ when } L \rightarrow \infty \text{ or } G_{ep} \rightarrow \infty. \end{aligned} \quad (3.24)$$

This indicates that: 1) in a sandwiched metal film that is very thin (or has very weak e-p coupling), the effective thermal conductivity is identical to its lattice portion and electrons are as if not involved at all. We call this the “thin limit”. And 2) when the metal is thick (or has strong e-p coupling), the effective thermal conductivity recovers the bulk value, and we call it the “thick limit”.

We expect that this interpretation, especially the thin limit, to be very useful for experimentalists. In experiments R_{pp} is often treated as the only TBR [132]. It is

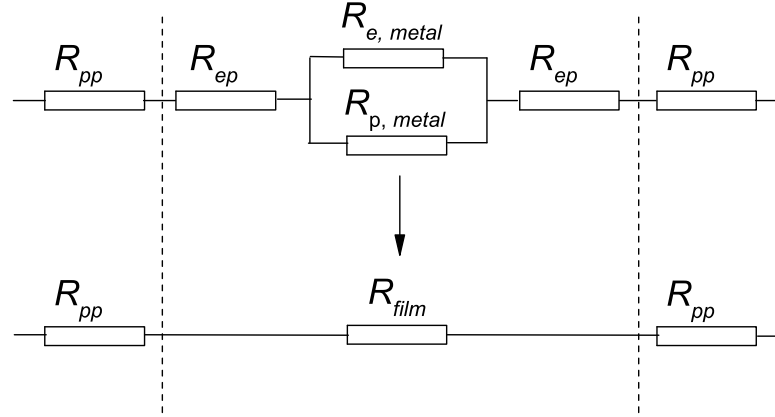


Figure 3.9. A new thermal circuit for a sandwiched metal thin film where R_{ep} is lumped into R_{eff} .

then straightforward to match the measured values with components of the thermal circuit in Fig. 3.9. If the thin limit applies, k_{eff} should become the lattice thermal conductivity while not the bulk metal conductivity $k_e + k_p$. This provides an intuitive way to check and interpret experiments.

A more detailed dependence of k_{eff} on the film thickness is illustrated in Fig. 3.10. Gold is still taken as the example here. It can be observed that the thin limit is valid when the thickness is much smaller than the e-p cooling length of 45 nm [24], as k_{eff} remains below 110% k_p when L is below 16.2 nm. In this range, which is usually the

case for a metal thin film sandwiched between dielectric materials, our new approach where R_{ep} is included as part of the film conduction resistance is more intuitive. Our model bypasses electrons' effect and only requires lattice temperature measurements for analysis, and the measured effective thermal conductivity k_{eff} is simply k_p . As L increases, k_{eff} starts to deviate from k_p and eventually converges to $k_e + k_p$. For a thickness larger than $10.2\text{ }\mu\text{m}$, which is more than 200 times larger than the cooling length, k_{eff} can be approximated as $k_e + k_p$ with an error smaller than 10%. In this range, which is usually the case when investigating an interface between two semi-infinite blocks, the original thermal circuit where R_{ep} is part of the TBR works better. The experimentally measured k_{eff} can no longer be interpreted by k_p . When L falls in the transition region marked in Fig. 3.10, an accurate analysis requires utilization of the exact form of Eq. (3.22) and investigation of the corresponding serial thermal circuit.

3.4.3 Temperature discontinuity at the interface

Finally, we want to discuss the phenomenon that our BTE calculation at such scale does not give result with size effect at the interface. Our calculations are all conducted at the length scale of $\sim 10\text{ nm}$. It is generally expected that the result of BTE method would be different from that of Fourier method because BTE calculation is able to predict the size effect at such length which is smaller than energy carriers MFP. This is usually observed as an extra TBR at the boundaries in addition to R_{pp} and R_{ep} mentioned above. It has been suggested by multiple previous works, mostly the EMA studies [122] and also some recent BTE works which compares equation of phonon radiative transport (EPRT) and Fourier calculations [90]. However our results show that the TTM-Fourier method and the TTM-BTE method match well with each other.

From our BTE simulation results, for an SAM-Au-SAM system of 12 nm length, the lattice temperature jump at the interface is 16.12 K and the heat flux is 6.08×10^{10}

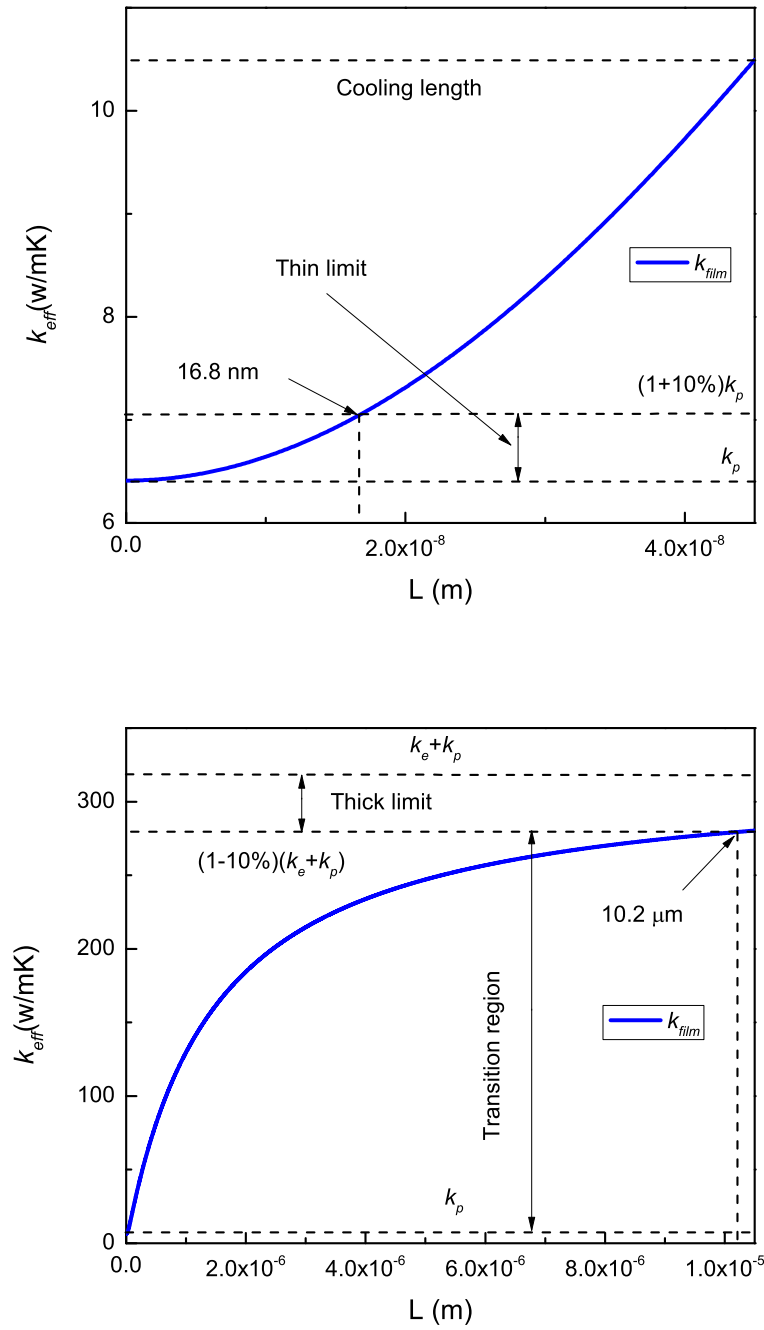


Figure 3.10. a) k_{eff} v.s. L for gold when L is within the e-p cooling length, which is 45 nm for gold. b) k_{eff} v.s. L for gold when L over a large range of thickness. k_{eff} eventually converges to its saturated value of $k_e + k_p$.

W/m², rendering a TBC of 377.18 MW/m²K. We also change the thickness of the gold film from 2 nm to 30 nm under transmission boundary condition. The results show that the TBC is a fixed value.

Now we want to compare our results from BTE method with DMM predictions. From Eq. (1.8), we can obtain an explicit expression of the ITC in gray model:

$$\begin{aligned} h_{pp} &= \frac{\frac{1}{2}D_1(\omega)n(\omega, T_{e1})v_{g1}\hbar\omega t_{12} - \frac{1}{2}D_2(\omega)n(\omega, T_{e2})v_{g2}\hbar\omega t_{21}}{T_1 - T_2} \\ &= \frac{1}{2}v_{g1}\hbar\omega t_{12}D_1(\omega)\frac{n(\omega, T_{e1}) - n(\omega, T_{e2})}{T_1 - T_2}. \end{aligned} \quad (3.25)$$

Note here two new temperatures are introduced: T_{e1} and T_{e2} . They are the temperature of the two phonon fluxes moving towards the interface. A factor of 0.5 is added to the phonon DOS since only half of the phonon population is moving in each direction. This is different from the conventional Landauer approach because we are using the temperature of each individual phonon flux, while the conventional approach only uses the equilibrium temperatures, i.e. T_1 and T_2 . This modified Landauer approach has been described by Chen and presented in their related BTE works [133]. In 1D gray model, T_{e1} and T_{e2} have the following expressions:

$$\begin{aligned} T_{e1} &= T_1 + \frac{1}{2}(T_{e1} - T_{e2})t_{12}, \\ T_{e2} &= T_2 - \frac{1}{2}(T_{e1} - T_{e2})t_{21}, \end{aligned} \quad (3.26)$$

Combined with Eq. (1.7), we can get:

$$T_{e1} - T_{e2} = 2(T_1 - T_2). \quad (3.27)$$

If the difference between T_{e1} and T_{e2} is infinite small, it is easy to see Eq. (3.25) collapses into:

$$h_{pp} = v_{g1}\hbar\omega t_{12}D_1(\omega)\frac{\partial n(\omega, T)}{\partial T} = v_{g1}t_{12}C_{p1}. \quad (3.28)$$

And in our gray model, where we assume the thermal properties of the materials are independent of temperature, then Eq. (3.28) is applicable regardless of the difference between T_{e1} and T_{e2} .

The properties of gold are taken from Table 3.2. From Eq. (1.7, 3.28) the phonon transmission rate from SAM to gold t_{12} is 0.768, which renders a phonon TBC of 377.74 MW/m²K. This matches our BTE simulation result, and again agrees well with our MD simulation results of 349.3±40.3 MW/m²K. This indicates that the BTE predicted phonon TBC agrees with the DMM predicted value, and that there is no additional TBR which is usually claimed to be the reason for size effect on thermal conductivity. Our LBM equations and boundary conditions are all from well-recognized previous works, and our simulations results show excellent agreement with our theoretical models. Therefore we claim that our calculation is self-consistent and the result is reliable.

It is worth noting that if we apply the conventional Landauer approach to calculate the TBC in our model, it will give the same result with the modified approach. In the conventional Landauer approach, Eq. (3.25) becomes:

$$h_{pp} = v_{g1} \hbar \omega t_{12} D_1(\omega) \frac{n(\omega, T_1) - n(\omega, T_2)}{T_1 - T_2}. \quad (3.29)$$

The factor of 0.5 is removed because the phonon flux is already the “averaged flux” including the entire phonon population. It is then easy to see that Eq. (3.29) leads to the same result with Eq. (3.28). The reason for this is that the modified Landauer approach works better when the two materials are similar, i. e. t_{12} and t_{21} are similar and close to unity. This is where the conventional Landauer approach fails and we have to use the modified one. However, in DMM t_{12} and t_{21} are required to have a unity summation due to the detailed balance principle, and under such condition the modified and conventional Landauer approaches are the same. Therefore they can both predict the same TBC in our simulations.

However it should be noted that we are only observing this disappearance of size effect in the metal middle layer, which has “transmission” interfaces at both ends. When we are looking at the boundaries in contact with thermal reservoirs, size effect is still observed as there is a sudden jump in the temperature profile at the boundary, and the effective thermal conductivity of the film is smaller than the material’s bulk value. This is because the thermal reservoirs relax the phonons’

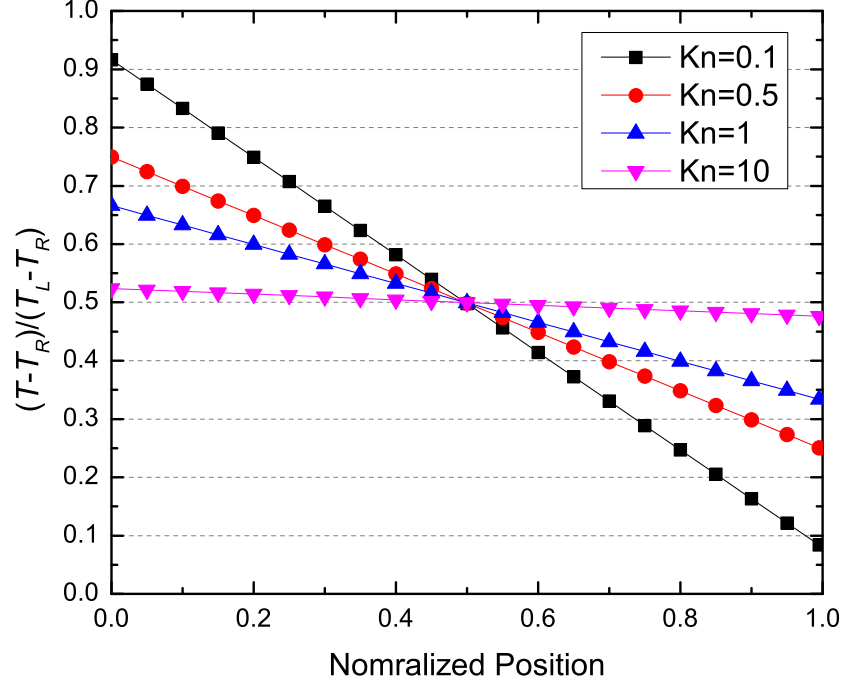


Figure 3.11. Temperature distribution in a single material thin film with different thickness. The temperatures at the two thermal reservoirs are constant. At the boundaries the temperature jump can be clearly observed, which agrees with previous works [90, 124, 134].

distribution when they hit the boundary, as is suggested by many previous BTE works [90, 124, 134]. In order to further validate our result, we also benchmark our BTE method by conducting simulations on a single material film under constant temperature boundary conditions. $Kn = \Lambda/L$ is the ratio of phonon MFP over the length of the film. The temperature of the two thermal reservoirs are kept at $T_L = 350$ K and $T_R = 250$ K respectively, and the film thickness L is varied. The result is shown in Fig. 3.11. This agrees well with previous related BTE works [90, 91], which indicates our approach is functioning correctly. Therefore, for a multi-layer system, we only need to consider the size effect at the very two ends which are in contact with thermal reservoirs, but do not need to consider this additional temperature jump at the interfaces regardless of the system size and the number of layers.

3.5 Conclusions

We have proposed TTM-Fourier and TTM-BTE approaches with input parameters from TTM-MD to predict the critical thickness L_c for metal particle-polymer composite in 1D. A general solution to TTM for thermal transport in a metal film sandwiched between dielectric materials is derived. As an example, L_c for 1D SAM-Au-SAM system is calculated to be around 10.8 nm. Based on the theoretical equations, we define an effective thermal conductivity for sandwiched metal thin films and propose a new thermal circuit analysis that are intuitive to interpret experimental results. A detailed discussion on the applicable range of our model is presented. It is shown that when the metal film is much thinner than its e-p cooling length (thin limit), the effective thermal conductivity reduces to just the phonon part. For a metal layer with large thickness (thick limit), the conventional thermal circuit is more advantageous, and the effective thermal conductivity recovers the metal bulk value. For the thickness in between the two limits, our general TTM solution still provides an accurate method for analysis. We also found Fourier and BTE calculations give identical results, indicating that in such multilayer system size effect does not exist in the middle layers, and we do not need thermal conductivity corrections in such systems except at the boundaries which are in contact with thermal reservoirs. This ensures the possibility to simplify the calculation at nanoscales and to make more methods applicable. Finally several factors affecting L_c are discussed, and it is discovered that the thermal conductivity, TBR and the e-p coupling factor all play important roles in determining L_c , which can provide us with a general guidance in the choice of materials when synchronizing a new composite.

4. TWO-TEMPERATURE MOLECULAR DYNAMICS SIMULATION OF METAL-DIELECTRIC INTERFACES WITH NON-LOCAL ELECTRON-PHONON COUPLING

4.1 Introduction

While the thermal transport at interfaces between dielectric materials have been well studied because only phonon coupling is involved in this process, the one at metal-dielectric interfaces is not fully conceived. Conventional TTM provides us with an excellent picture of the temperature profile where electrons are considered as insulated from entering the dielectric [24, 31, 135], but it also leaves us with questions. As is mentioned previously, experiments show that the ITC is unexpectedly high at several metal-diamond interfaces, indicating that physics in addition to elastic phonon scattering is playing an important role in these cases.

Experiments have demonstrated that at room temperature, the ITC of several systems such as Pb-diamond and Au-diamond are much higher than the values predicted by AMM or DMM models [9], indicating that mechanisms other than elastic phonon transmission are important. Several explanations have been proposed, but no consensus has been reached yet. One model, proposed by Overhauser [9], attributed the high ITC to the coupling of metal electrons to the joint phonon modes formed at the interface. This mechanism is interesting and plausible, while the size of the joint modes region was approximated as the phonon mean free path without much justification. Also, it is questionable to treat the coupling of electrons with joint phonon modes as a single conductance channel without considering the phonon-phonon (p-p) resistance inside the joint modes region. Detailed discussions of these issues are provided in Sec. 4.4.2. Sadasivam et al performed first principles calculations and calculated the Eliashberg function of a heterojunction supercell to obtain a thermal conductance

due to the coupling between electrons and joint phonon modes, and concluded that it cannot be neglected as compared to the p-p channel [136]. Sergeev proposed a Green's function-based model to calculate the cross-interface coupling factor h_{ep} under a gray and diffusive assumption [137, 138]. In contrast, several other studies have shown that this mechanism is not important at room temperature. Stoner and Maris applied time domain thermal reflectance (TDTR) technique to measuring the Kapitza conductance between metal-dielectric interfaces from 50 K to 300 K, and claimed that the high conductance is not due to electronic effects but inelastic phonon process at the interface [11]. Cahill et al used metals with very different electron density while keeping the other conditions similar, and observed similar ITC, supporting the conclusion that electron-joint phonon modes coupling is insignificant [10, 12]. Other experiments done by Hopkins et al [14] came to the same conclusion. The existing TTM [31] and TT-MD [24] studies have also neglected cross-interface electron-phonon (e-p) coupling. Such discrepancy warrants further theoretical and experimental investigation of the role of electrons. It should also be noted that when electrons in the metal are driven strongly out of equilibrium, these high-energy electrons are at very high effective temperature ($>4000\text{K}$) and can indeed interact with phonons in the substrate directly [16, 70, 139]. Models such as the three-temperature model [16] have also been developed to include the cross-interface e-p coupling mechanism for such highly non-equilibrium situations.

In this study we extend our previous TTM-MD approach [24] by including the cross-interface e-p coupling, in order to provide a simulation tool towards addressing the debate. We choose TTM-MD since it can predict the temperature profiles and include all the potentially important process in a single simulation, including elastic and inelastic phonon scattering at the interface; e-p coupling inside the metal as well as cross the interface. The goal of the current work is to introduce the approach and the associated thermal circuit, rather than to assess the relative importance of these processes that may well be system specific.

4.2 Theory

4.2.1 A preliminary model for non-local electron-phonon coupling

The standard two-temperature equations and the resulting temperature profiles of electrons and phonons across metal-nonmetal interfaces have been described in detail in Refs. 24, 31, while the cross-interface e-p coupling was not considered. However, the coupling of electrons in the metal with phonons in the dielectric is a possible thermal transport channel. Such cross-interface e-p coupling is not well understood, and previous treatments by Sergeev [137, 138] and Hopkins [16] are all based on the idea of electron interacting with a geometric interface without volume, which could be described by a Neumann boundary condition mathematically. However, recent studies indicated that this electron-ion interaction is a long-range effect [140]. Therefore it is more reasonable to consider the cross-interface electron-phonon (e-p) interaction as a volumetric effect.

Here we modify the standard two-temperature equations to include non-local e-p coupling. Our model is illustrated in Fig. 4.1, in which the entire system is divided into four regions: A, B, C, and D. For simplicity, we still assume that the e-p interaction is homogeneous in the metal, and the change of e-p coupling strength near the boundary is ignored in the following analysis. Electrons in the nonmetal side are also ignored due to their negligible contribution [24, 141]. The heat transfer process is considered in 1D steady state condition.

Region A is the part of metal that is far away from the interface, hence the standard TTM governing equations could be applied:

$$\begin{aligned} \text{When } x < -b, \\ k_{e,metal} \frac{\partial^2 T_{e,metal}}{\partial x^2} - S_{ep,A}(x) &= 0, \\ k_{p,metal} \frac{\partial^2 T_{p,metal}}{\partial x^2} + S_{ep,A}(x) &= 0, \end{aligned} \tag{1a}$$

where k is the thermal conductivity of each carrier, and $S_{ep,A}$ (unit: W/m³) is the internal volumetric heat generation due to e-p coupling.

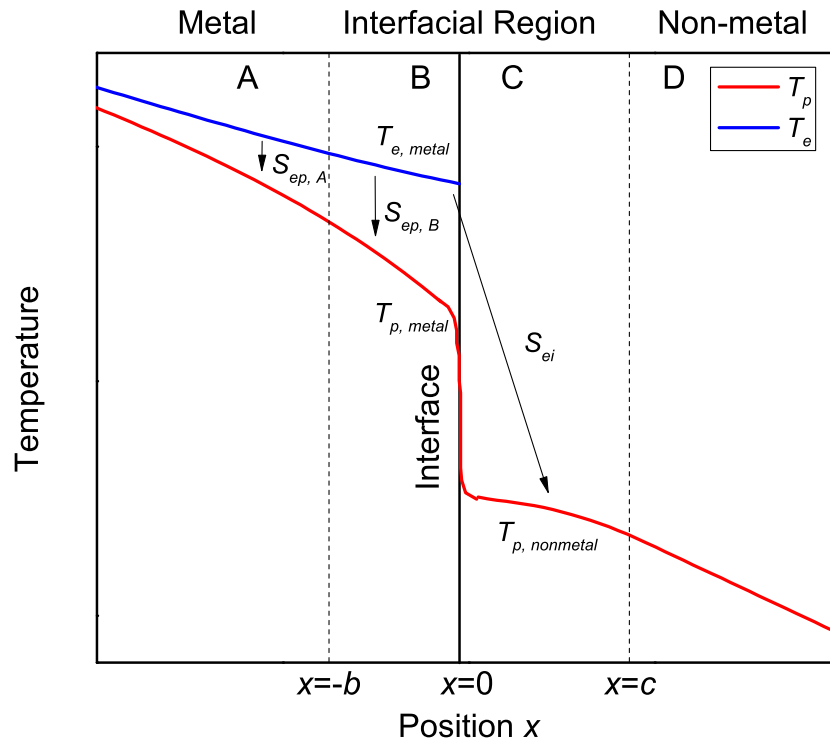


Figure 4.1. The four regions defined at the metal-nonmetal interface in our analysis. Region A is the bulk metal region, while Region B and C are the interfacial regions, and Region D is the bulk nonmetal region.

Region B is the near-interface part of the metal, where electrons in the metal can interact with phonons in both the metal (Region B) and the nonmetal (Region C). In other words, there are both bulk and cross-interface coupling for electrons in this region. The governing equations are:

$$\begin{aligned}
&\text{When } -b < x < 0, \\
&k_{e,metal} \frac{\partial^2 T_{e,metal}}{\partial x^2} - S_{e,B}(x) = 0, \\
&k_{p,metal} \frac{\partial^2 T_{p,metal}}{\partial x^2} + S_{ep,B}(x) = 0, \\
&S_{e,B}(x) = S_{ep,B}(x) + S_{ei}(x), \\
&S_{ep,B}(x) = G_{ep,metal}[T_{e,metal}(x) - T_{p,metal}(x)], \\
&S_{ei}(x) = G_{ei}[T_{e,metal}(x) - T_{p,nonmetal}].
\end{aligned} \tag{1b}$$

Here G_{ep} and G_{ei} (unit: W/m³K) are the bulk e-p coupling factor in the metal and the effective cross-interface e-p coupling factor, respectively. $S_{e,B}$ includes two parts: 1) $S_{ep,B}$ is the volumetric heat generation due to bulk e-p coupling, and 2) S_{ei} is the volumetric heat generation due to electrons in B interacting non-locally with phonons in C. The last expression provides a method to estimate this amount. $T_{p,nonmetal}$ is set as the average phonon temperature in Region C. The choice of G_{ei} will be discussed in Sec. 4.3.2.

In Region C, no free electrons exist, but phonons can interact non-locally with electrons in B. Therefore the governing equation is:

$$\begin{aligned}
&\text{When } 0 < x < c, \\
&k_{p,nonmetal} \frac{\partial^2 T_{p,nonmetal}}{\partial x^2} + S_{p,C}(x) = 0, \\
&\int_{-b}^0 S_{ei}(x)dx = \int_0^c S_{p,C}(x)dx,
\end{aligned} \tag{1c}$$

where $S_{p,C}$ is the volumetric energy source for phonons in the nonmetal, and its relation with S_{ei} is also expressed.

Region D is the bulk part of nonmetal where heat is transferred by phonons, and the governing equation is:

$$\begin{aligned} &\text{When } x > c, \\ &k_{p,\text{nonmetal}} \frac{\partial^2 T_{p,\text{nonmetal}}}{\partial x^2} = 0. \end{aligned} \tag{1d}$$

So far we have derived the governing equations for the metal-nonmetal interface. However, determining the size of regions B and C can be rather arbitrary due to the poor understanding of cross-interface e-p coupling. Based on previous studies, here we use two approximations respectively. The first is based on the “joint-modes” concept proposed by Overhauser [9]. Although in their original model the size of the joint modes region is the phonon mean free path, here we modify it to the region of interface reconstruction according to our molecular dynamics results. The phonon spectrum in this region varies gradually from the bulk spectrum of one material to that of the other. This picture has been successfully used to gain more insights to phonon interfacial transport [142, 143]. In our work, electrons in the metal side of the joint-modes region are assumed to interact with phonons in both sides of the joint-modes region. Therefore Regions B and C together in Fig. 4.1 are the joint-modes region, and the sizes can be predicted through MD simulations. It should be noted that the size will depend on the interfacial bonding strength. For example, van der Waals bonding leads to almost no joint modes region [143]. The other approximation is the “phonon wavelength” model. Since phonon is a wave-particle dual description of lattice vibrations, it cannot be generated within a space that is smaller than its wavelength in any dimension. Meanwhile, we notice that the e-p interaction is non-local since the Coulomb interaction between electrons and nuclei is long-range. Therefore each electron is assumed to interact with phonons within a distance of the phonon wavelength on both left and right. At the interfacial region, electrons in the metal can interact with phonons in the nonmetal up to a distance of the average wavelength of the phonons in the nonmetal. Consequently the e-p coupling becomes non-local throughout the entire system.

4.2.2 Implementation in two-temperature molecular dynamics

We have previously employed TTM-MD to numerically solve the standard two-temperature equations across metal-nonmetal interfaces [24]. Here, we modify the TTM-MD approach to numerically solve the modified two-temperature equations described in the preceding section. The simulation system is divided into grids using finite volume method (FVM). Within a grid the atoms and the corresponding electrons interact with each other through the coupling term according to TTM theory.

To implement the joint-modes model to our original TTM-MD, we assign a group of atoms, i.e. Region C, in the nonmetal that will interact with electrons in the metal. The size of Region C is determined by the size of the joint-modes region, which does not have a definite standard in the literature. In our model, it is defined as the region where the temperature profile becomes nonlinear in a phonon-only NEMD simulation, as used in several previous studies [142, 143]. In a typical NEMD simulation (such as Fig. 4.4a and Fig. 4.4b in the later section), it is usually observed that the temperature profile becomes nonlinear near the interface of two dissimilar materials, which is due to interface reconstruction. The size of the reconstruction region is often affected by many factors such as the interfacial bonding strength, the cutoff range of the potentials used in the simulation, etc. In this study the size of this nonlinear region based on our MD simulations is determined. At the interface, electrons in Region B will have an additional interaction with phonons in Region C, which is added to the FVM equation.

On the other hand, to implement the phonon wavelength model to our original TTM-MD, the non-local e-p interaction is applied throughout the entire system. Hence, the case is more complicated. In the FVM, electrons in each grid interact with phonons in the same grid as well as in adjacent grids within a distance of one phonon wavelength. This mechanism is illustrated in Fig. 4.2.

Each electron can couple to phonons in a region of $2\lambda_{avg}$ centered on the electron. The bulk coupling strength is divided evenly into this region, so the overall effective

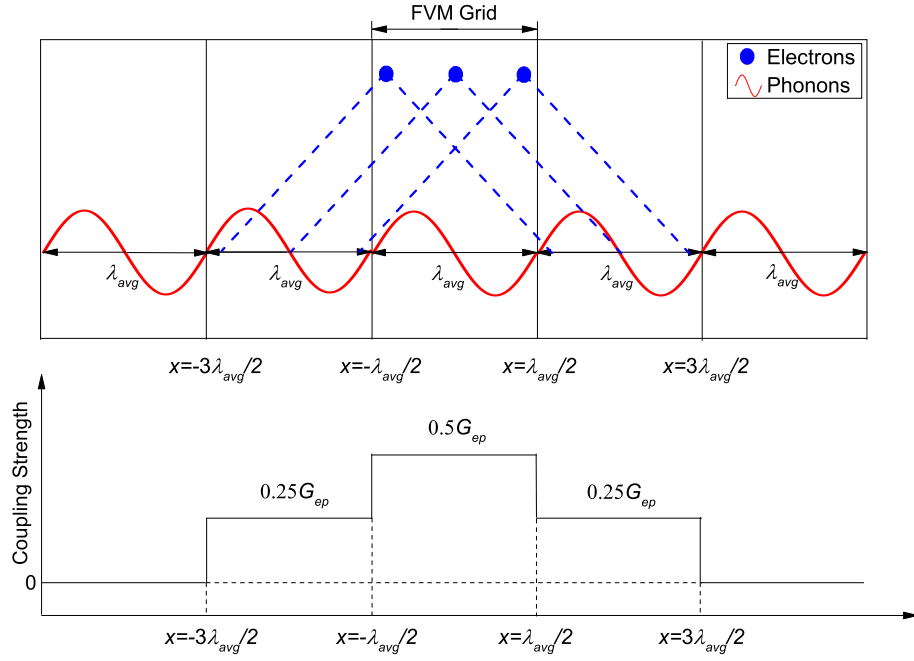


Figure 4.2. Illustration of the non-local coupling mechanism. The system is discretized into grids using FVM. λ_{avg} is the average wavelength of phonons in the material. Each electron can couple to phonons in a region up to the length of $2\lambda_{avg}$. The upper figure also shows the coupling range of three different electrons: one in the center of the grid, and the other two near the boundary of the grid. The lower figure shows the effective coupling strength of electrons in the central grid to phonons from all the grids. G_{ep} is larger in the electrons' own grid, while smaller in the adjacent grids, and becomes zero in grids which are beyond the coupling range of any electron.

coupling factor stays the same. We provide a more specific explanation of this by deriving a new expression for $S_{ep,A}$ in Eq. (1a). For each electron located at x_0 , $S_{ep,A}$ can be expressed as:

$$S_{ep,A}(x_0) = \int_{x_0-\lambda_{avg}}^{x_0+\lambda_{avg}} \frac{G_{ep}}{2\lambda_{avg}} [T_e(x_0) - T_p(x)] dx. \quad (4.1)$$

The expression for $S_{ep,B}$ is similar except that the upper limit in the integration has to be changed,

$$S_{ep,B}(x_0) = \int_{x_0-\lambda_{avg}}^0 \frac{G_{ep}}{2\lambda_{avg}} [T_e(x_0) - T_p(x)] dx. \quad (4.2)$$

The size of Region B is chosen as the same as that in the joint-modes model. In this way the same amount of electrons are involved in the cross-interface e-p coupling so that these two models are more comparable.

4.3 Cu-Si case study and results

In this section, we will present TTM-MD simulation based on our models on the copper-silicon solid interface system.

4.3.1 Simulation system

The Cu-Si system we study here is the same as in our previous work [24], which is illustrated in Fig. 8.1. The system is set up initially with the periodic boundary condition in all three dimensions. Both Cu and Si are in contact via their (100) surface. The lattice parameters for Cu and Si are 3.61 Å and 5.43 Å, respectively, and the cross-section of the system is 10×10 Si unit cells, or 15×15 Cu unit cells. As a result there is 0.3% mismatch between Cu and Si lattice in the cross-section plane. The length of the Si segment is 32 nm, while the length of the Cu segment is 96 nm. The many-body Tersoff potential [144] and the embedded-atom method (EAM) [145] potential are used for Si-Si and Cu-Cu interactions, respectively, and the interfacial Cu-Si interaction is described by the Morse potential [146],

$$U = D_e [e^{-2\alpha(r-r_0)} - 2e^{-\alpha(r-r_0)}], \quad (4.3)$$

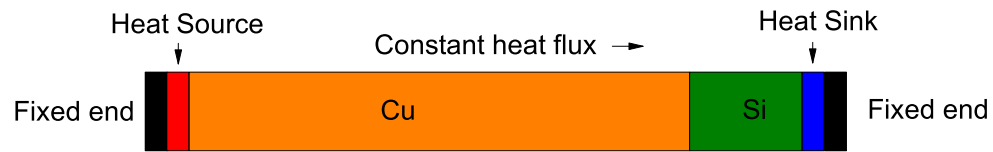


Figure 4.3. Illustration of the simulation system. Black parts refer to the fixed ends where atoms have no velocities. The red and blue parts are the heat source and heat sink respectively. Heat flows in the direction perpendicular to the interface which results in 1D conduction. The periodic boundary condition is applied in the other two directions.

where $D_e=0.9$ eV, $\alpha=1.11$ Å⁻¹, $r_0=3.15$ Å. Initially the system is relaxed under zero-pressure using a Nose-Hoover thermostat [147] at 300 K for 0.3 ns, and then the fixed boundary condition is applied in the x direction in which the heat flows. A layer of two unit cells is fixed at each end. The atoms in these layers are set to zero velocity and zero force so there is no atomic interaction in these regions. The thickness of the two layers together is larger than the potentials' cut off ranges. Therefore the periodic boundary condition is transformed into the fixed boundary condition. Then the system is switched to NEMD, where a constant heat flux of $J=3.2\times 10^{-7}$ W is injected to the heat source region while extracted from the heat sink region, to establish 1D conduction. TTM calculation is presented on the Cu block included in this simulation domain. It is discretized into grids of 0.75 nm thickness for the FVM calculation. The size of the grid is approximately the same as the average phonon wavelength in Cu with a difference of 2%. Therefore in the phonon wavelength model, electrons in each grid will interact with phonons in the same grid and also the two adjacent grids, just as illustrated in Fig. 4.2. However, it should be noted that we cannot specify the precise location of each electron or phonon within the grid, and not all the electrons and phonons in two adjacent grids can interact with each other (since the maximum distance between a pair of electron and phonon is $2\lambda_{avg}$, e.g. one phonon located at $x = -3\lambda_{avg}/2$ cannot interact with one electron located at $x = \lambda_{avg}/2$). Therefore in order to correctly implement Eq. (4.1), we need to specify the effective coupling strength to account for the actual number of interacting energy carriers. As is shown in Fig. 4.2, G_{ep} in one grid is divided into three parts: a local effective $0.5G_{ep}$ in the central grid itself, and a non-local effective $0.25G_{ep}$ in each of the two adjacent grids. In this way the simulation is fully consistent with Eq. (4.1). The overall effective G_{ei} in Region C is set to the same in both models. From the simulation results we can acquire the temperature profiles of both electrons and phonons, and the thermal properties of them.

Table 4.1.
Important input thermal properties for the TTM-MD
calculation

Property	Value
C_e	$5.26 \times 10^4 \text{ J/m}^3\text{K}$
k_e	401 W/mK
$G_{ep,Cu}$	$5.5 \times 10^{16} \text{ W/m}^3\text{K}$
G_{ei}	$5.5 \times 10^{16} \text{ W/m}^3\text{K}$

4.3.2 Input parameter

Different from the original MD, TTM-MD requires an extra set of input parameters, mostly the electronic parameters of the metal. k_e can be estimated using the Wiedemann-Franz law from copper's electrical conductivity. We use 401 W/mK at 300 K [148] as the value for k_e . For volumetric heat capacity C_e and G_{ep} within copper, Lin has shown a comprehensive work on the thermal electronic parameters of different metals [129]. It is reported that C_e is almost linearly proportional to T_e when T_e is below 1000 K . G_{ep} has reported values ranging from $5.5 \times 10^{16} \text{ W/m}^3\text{K}$ to $2.6 \times 10^{17} \text{ W/m}^3\text{K}$ [129, 148]. Here we choose $5.5 \times 10^{16} \text{ W/m}^3\text{K}$ to be consistent with our previous work. b is the size of Region B and c is the size of Region C. They are determined with respect to different models. In the joint-modes model, as stated previously, they are determined by the size of the interface reconstruction region observed in MD simulations. In this work, we found that b was approximately 0.5 nm and c was within the range of $1 \sim 1.5 \text{ nm}$. In the phonon wavelength model, the average phonon wavelength is approximated using $\lambda_{avg} = hv/k_B T$, where v is the average sound velocity in that material, h is the Planck constant and T is the temperature. In silicon λ_{avg} is calculated to be 1.4 nm , which is within the reported range the in previous work Ref. 57 and chosen as the value for c . Therefore, for both models, we set $b=0.5 \text{ nm}$ and $c=1.4 \text{ nm}$. This makes the e-p coupling style the

only difference between these two models. According to previous studies, G_{ei} can be relatively very small when electron temperature is around 300 K [16, 70]. However, in copper there are only acoustic phonons while in silicon there are also optical phonons, and electrons have been reported to couple strongly to some of the optical phonon branches [1, 149], therefore we assume that $G_{ei} = G_{ep, metal}$. Combined with our choice of c , we can obtain an equivalent ITC h_{es} [16] of 77 MW/m²K, which is comparable with the reported value of 10~100 MW/m²K for Au-Si interface at room temperature [16]. Since copper and gold have the same crystal structure and G_{ep} of the same order, we believe our assumption is qualitatively reasonable.

It should be noted that the choices of many parameters used in this simulation are based on simple assumptions, since commonly accepted prediction methods for these parameters are still not available. These parameters include: 1) the coupling distance of non-local e-p coupling. In the phonon wavelength model, we have used the average phonon wavelength estimated from $\lambda_{avg} = hv/k_B T$ which is based on the Debye approximation, hence λ_{avg} primarily represents acoustic phonons. There are certainly other options. For example, it has been pointed out that different phonon branches have different coupling strength to electrons. Hence one may weigh the average phonon wavelength with respect to the coupling strength. 2) Distribution of non-local e-p coupling strength: currently in both models we have distributed electron's (or phonon's) coupling strength evenly into its coupling distance. However, alternative distribution such as Gaussian or exponential may be more realistic since electrons should couple to phonons nearby more strongly than phonons that are farther away. 3) The value of G_{ei} , which is a key factor in determining how efficient the cross-interface e-p coupling could be, is arbitrary in our simulations. Overall, although these parameters are approximate, our primary goal is to demonstrate our TT-MD approach, and later establish a thermal circuit that could correctly describe the interfacial thermal transfer channels. These input parameters can be refined when more sophisticated prediction methods become available in the future.

Table 4.2.
Results of TBR from different MD simulations

Model	$R_{B,tot}$ (m ² K/W)
Original TT-MD	2.8×10^{-9}
The joint-modes model	2.29×10^{-9}
The phonon wavelength model	2.33×10^{-9}

4.3.3 Results

We first present the results of the joint-modes model. The temperature profile is shown in Fig. 4.4a, in which electrons and phonons have a linear equilibrium curve in the middle of the metal block but become non-equilibrium near the interface. The linear equilibrium curve is extrapolated towards the interface. The total TBR is calculated as $R = \Delta T/J$, where ΔT is the temperature jump between $T_{fit}|_{x=0}$ and $T_p|_{x=0}$. The total TBR is calculated to be 2.29×10^{-9} m²K/W, which is about 18% lower than the TBR value of 2.8×10^{-9} m²K/W reported in our previous TT-MD model that did not consider the cross-interface e-p coupling [24].

Then we present the simulation results using the phonon wavelength model on the same system, where all the conditions and parameters applied are the same as the joint-modes model except the coupling style. The temperature profile is shown in Fig. 4.4b. Generally with this global non-local coupling we would expect the results to be different from the joint-modes model. For instance, the e-p non-equilibrium is expected to be smaller. However the results turn out to be fairly similar. The total TBR is calculated to be 2.33×10^{-9} m²K/W, which is about 1.5% larger than that in the joint-modes model. The results of TBR from our original TT-MD in Ref. 24 and two new models in this work are listed in Table. 4.2.

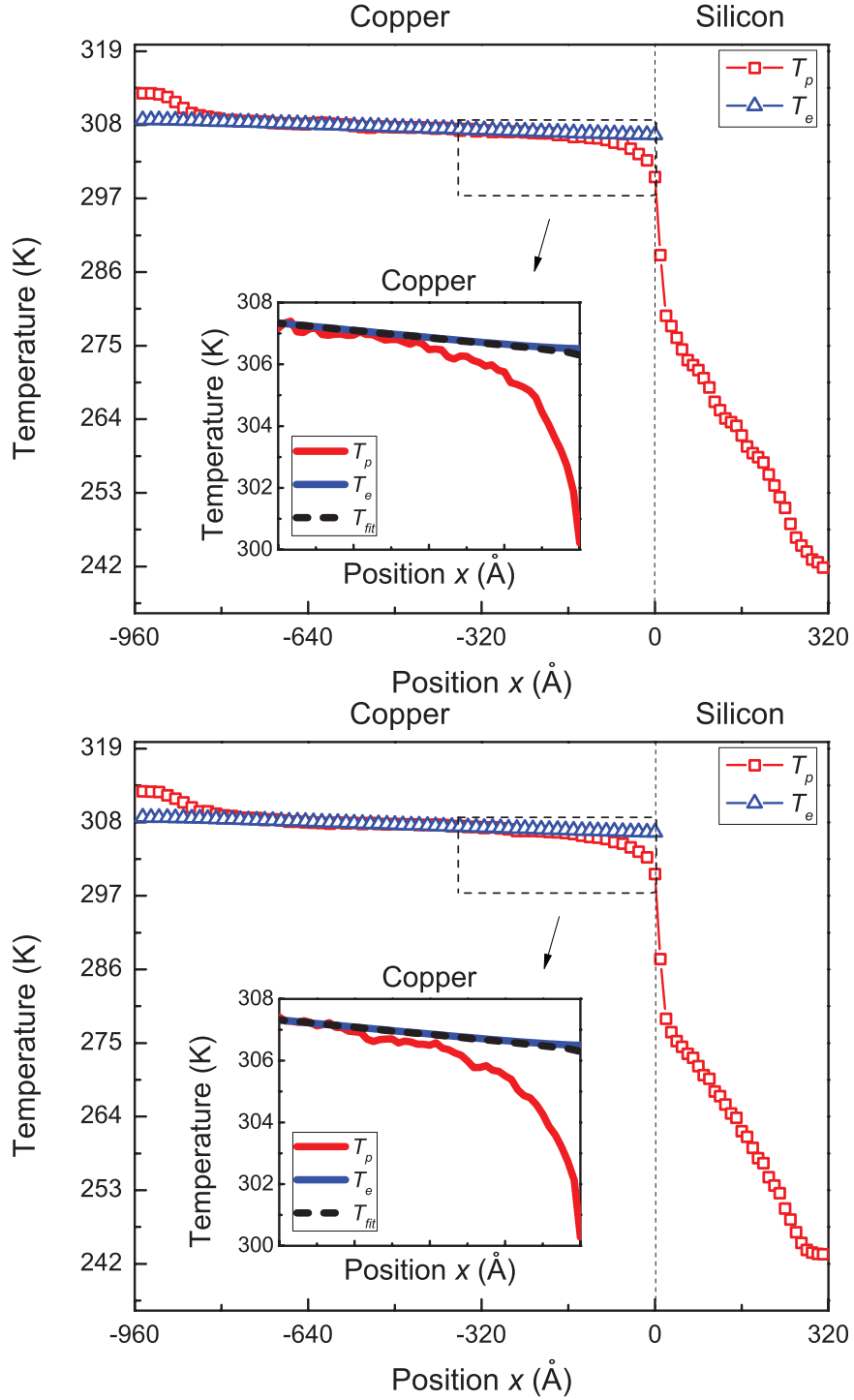
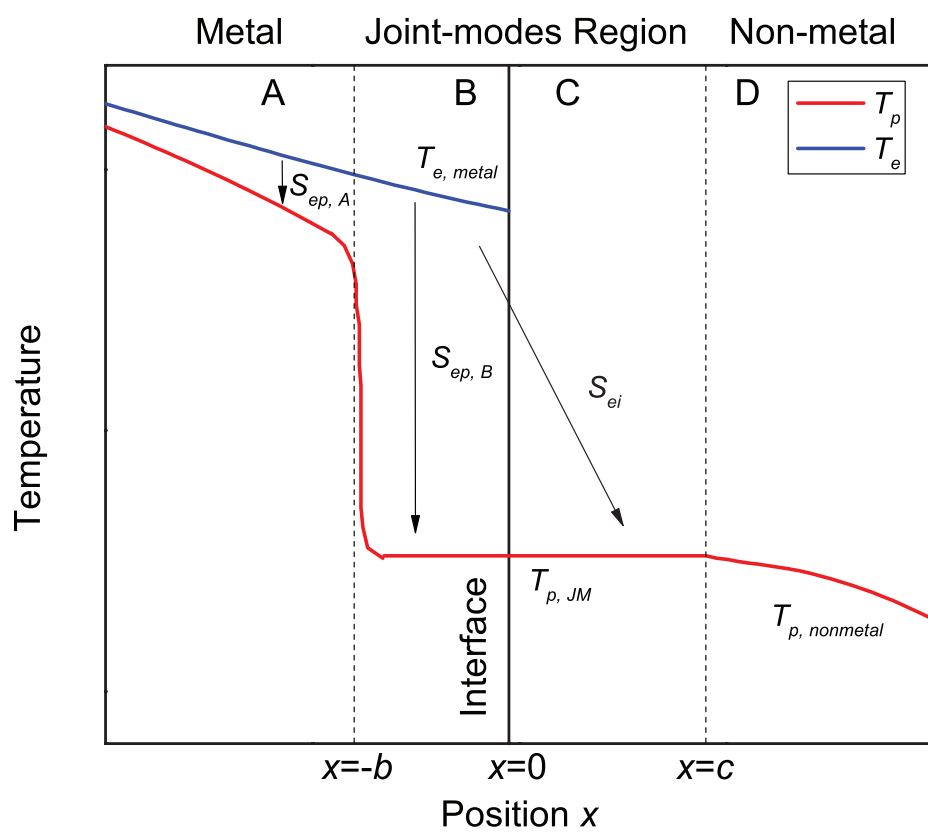
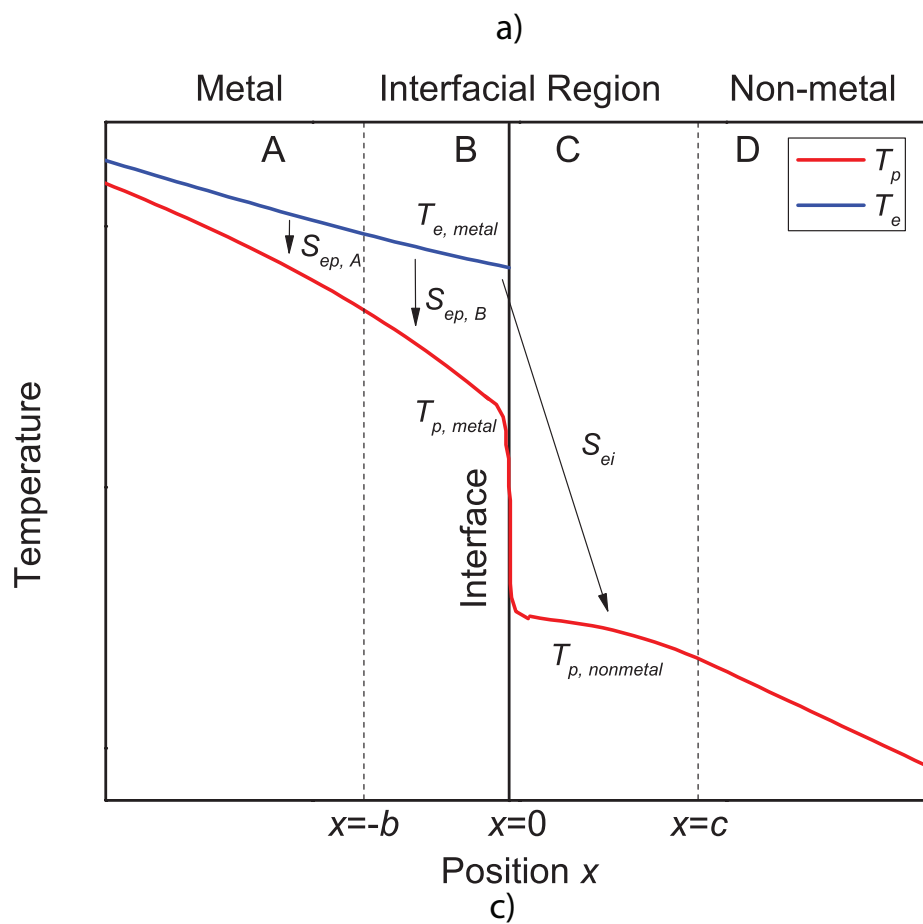


Figure 4.4. a) Temperature profile from a TT-MD simulation on the Cu-Si system with non-local e-p coupling using the joint-modes model. The fitted temperature is acquired by extrapolation. It can be observed that the fitted temperature is almost identical to electrons' temperature since electrons have a much higher effective thermal conductivity. b) Temperature profile from the phonon wavelength model. Overall the result is not much different from that of the joint-modes model.



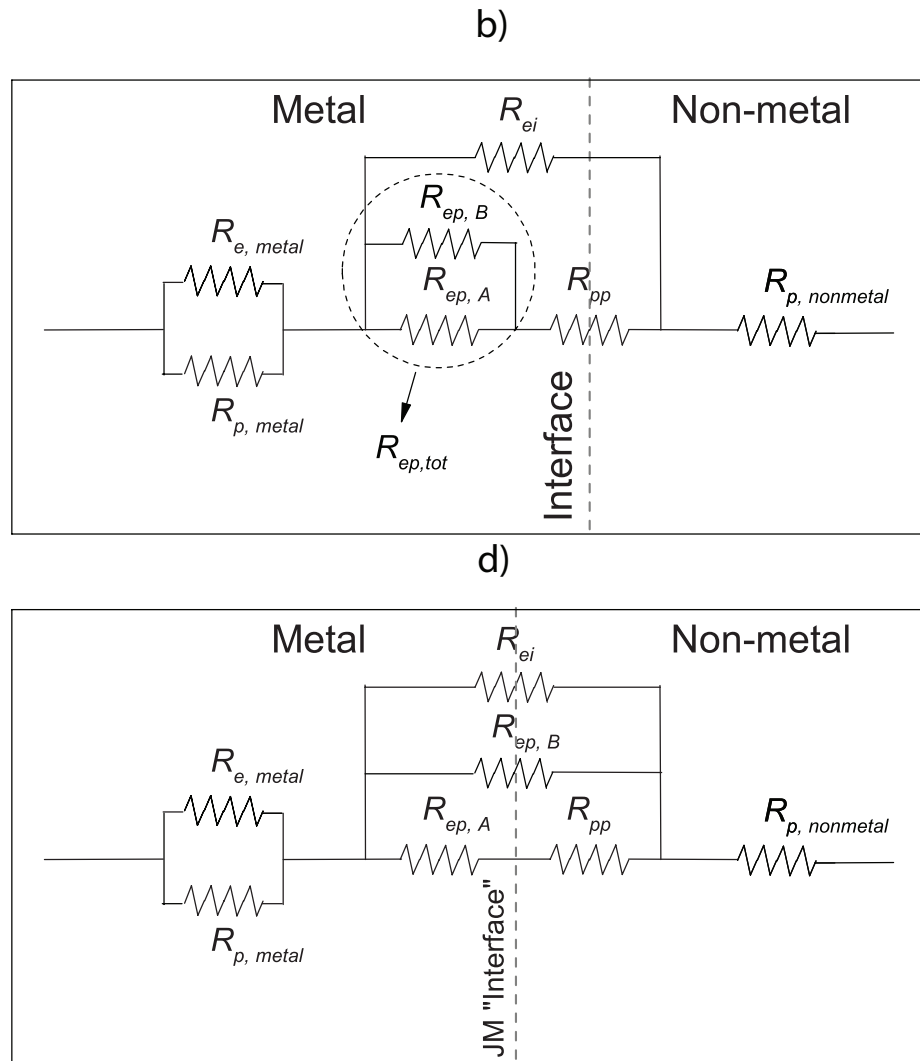


Figure 4.5. a) b) Qualitative temperature profile of our model and the corresponding thermal circuit. c) d) Qualitative temperature profile of Overhauser's model and the corresponding thermal circuit. $R_{ep, tot}$ is the resistance due to e-p non-equilibrium, R_{pp} is the resistance due to p-p cross-interface coupling, and R_{ei} represents the channel of cross-interface e-p coupling.

4.4 Thermal circuit analysis

4.4.1 Thermal circuit based on our models

If the cross-interface e-p coupling is not considered, the thermal circuit is a simple series circuit of the e-p and p-p coupling resistances [24]. It will be insightful to see how the thermal circuit should change after this effect is included. By adding an additional cross-interface e-p coupling channel to the original circuit [24], the thermal circuit can be established as shown in Fig. 4.5b. Among these resistances, R_{pp} can be calculated based on the phonon temperature jump in the MD simulations. $R_{ep,tot}$ is the e-p coupling resistance in the metal which we divide into two parts: $R_{ep,A}$ which is the e-p coupling outside of the “joint-modes” or “phonon wavelength” region but within the electron cooling length, and $R_{ep,B}$ which is the e-p coupling within the “joint-modes” or “phonon wavelength” region. The energy transfer is marked as $S_{ep,A}$ and $S_{ep,B}$, respectively. Since the size of Region B is very small compared with the entire metal block, $R_{ep,B}$ is approximated as:

$$R_{ep,B} = \frac{1}{h_{ep,B}} = \frac{1}{G_{ep,B} \cdot b}, \quad (4.4)$$

where $G_{ep,B}$ is assumed to be the same as in the bulk metal. Finally, R_{ei} can be fitted using the total TBR and all the other known resistances. The decomposed resistances are listed in Table. 4.3. Take the results from the phonon wavelength model as an example, $R_{ep,tot}$ is $0.60 \times 10^{-9} \text{ m}^2\text{K/W}$, with $R_{ep,A}$ being $0.61 \times 10^{-9} \text{ m}^2\text{K/W}$ and $R_{ep,B}$ being $3.64 \times 10^{-8} \text{ m}^2\text{K/W}$. R_{pp} is $2.20 \times 10^{-9} \text{ m}^2\text{K/W}$. Since the overall TBR is $2.33 \times 10^{-9} \text{ m}^2\text{K/W}$, we can obtain an R_{ei} of $1.26 \times 10^{-8} \text{ m}^2\text{K/W}$. The value is comparable with results of $R_{ei,Au-Si} = 0.01 \sim 10 \times 10^{-8} \text{ m}^2\text{K/W}$ measured using TDTR in Refs. 16,139. It is noteworthy that if we use Eq. (4.4) to estimate R_{ei} (rather than fitting) while we replace $G_{ep,B}$ and b with G_{ei} and c respectively, we obtain a result of $1.30 \times 10^{-8} \text{ m}^2\text{K/W}$, which is pretty close to the fitted value with a difference of 3.2%. R_{ei} is much larger compared with other resistances, indicating that the cross-interface e-p coupling is weaker than local coupling even when we assign the coupling factor to be

Table 4.3.
Results of decomposed TBR in different models (values are in unit of $\text{m}^2\text{K/W}$)

Resistances	Our models		Overhauser's model
	The joint-modes model	The phonon wave-length model	
$R_{B,tot}$	2.29×10^{-9}	2.32×10^{-9}	4.50×10^{-10}
R_{pp}	2.20×10^{-9}	2.20×10^{-9}	2.20×10^{-9}
$R_{ep,A}$	0.61×10^{-9}	0.61×10^{-9}	0.69×10^{-9}
$R_{ep,B}$	3.64×10^{-8}	3.64×10^{-8}	4.43×10^{-9}
R_{ei}	1.26×10^{-8}	1.35×10^{-8}	6.06×10^{-10}

the same. However, for metals with medium e-p coupling strength such as copper, this additional energy transfer channel is still able to reduce the overall TBR by approximately 20%.

4.4.2 Merits and drawbacks of the original model of Huberman and Overhauser

The concept of “joint phonon modes” at the interface was proposed by Huberman and Overhauser in Ref. 9, where the interface was understood as a joint region rather than an abrupt geometric interface. This concept was successfully used by several groups later to decompose the phonon interfacial resistance into interfacial region resistance and boundary resistance [142, 143]. When using their model to treat e-p coupled transport across an interface, however, we should note both the merits and drawbacks. In their model, which we designate as “Overhauser’s model”, the “joint-modes” region extends to one phonon mean free path on each side of the interface. Therefore, the material with longer phonon mean free path will have larger portion of the joint-modes region. In the joint-modes region, the atoms are at a uniform

temperature and vibrate in the same “joint-modes”. Under Overhauser’s model, the corresponding temperature profile is shown in Fig. 4.5c, where the temperature of the joint-modes region is uniform and equal to the temperature of the silicon side due to much longer phonon mean free path in silicon than in copper. As a result, the temperature jump has to occur in copper somewhere outside of the joint-modes region. Under this picture, the e-p energy transfer in the metal side of the joint-modes region ($S_{ep,B}$) becomes an independent conductance channel. The corresponding thermal circuit is depicted in Fig. 4.5d. Applying this model to our system, then the sizes of region B and C are modified to be: $b=4.1$ nm and $c=30$ nm, which are the approximate average phonon mean free paths in copper and silicon respectively. In determining the values of each individual resistance, $R_{e,metal}$ and $R_{p,metal}$ are assumed to be the same because the size difference of region B only changes these values by less than 1%. R_{pp} is also set as the average of the results predicted by our MD simulations. $R_{ep,tot}$ is broken down in the same way as previously, and $R_{ep,B}$ is determined by Eq. (4.4) as well. R_{ei} is also determined using Eq. (4.4), but $G_{ep,B}$ is replaced with G_{ei} and b is replaced with c . The results are listed in the last column of Table. 4.3. It turns out that the total TBR predicted by their model is only 20% of the value of our model. We attribute the difference to two reasons. First, our TT-MD simulation results in Fig. 4.4 show that the phonon temperature in the joint-modes region rapidly drops rather than being uniform. Similar results have been obtained in other previous works [142, 143]. This is reasonable since the joint-modes region is the location where most mismatch occurs, and the temperature drop should occur here rather than in the homogeneous metal outside of the joint-modes region. We consider the assumption of uniform temperature in the joint-modes region in Overhauser’s model unphysical. As a result, the e-p coupling in the metal side of the joint-modes region ($R_{ep,B}$) is in series with the p-p coupling across the interface R_{pp} , rather than being an independent conductance channel. The accurate thermal circuit should be represented by Fig. 4.5b instead of 4.5d. Therefore, knowing the temperature profiles and then constructing the correct thermal circuit is essential for understanding metal-dielectric interfacial

transport. Second, the size of the joint-modes region is different between our model and Overhauser’s model. To determine the value of R_{ei} in Overhauser’s model, the effective phonon mean free path is used and it is assumed that electrons in B can couple evenly to phonons in C, and the relatively large size of Region C leads to a very small R_{ei} compared with other resistances. In fact a choice of $c=30$ nm is already conservative since the spectral phonon mean free path in silicon can span several orders of magnitude [150]. However, since electrons lose energy primarily to optical phonons, it will be more appropriate to consider optical phonon mean free path which is usually much smaller than the effective phonon mean free path. Indeed, recent MD simulations have indicated that the joint-modes region is small, on the scale of phonon wavelength or several bond lengths [142, 143]. Nevertheless, the impact range of non-local e-p coupling is not well understood yet and is deserved further studies. In Overhauser’s original model, these two factors have contributed to the over-estimation of the contribution of cross-interface e-p coupling to the ITC.

4.5 Conclusions

We have presented a TTM-MD framework to simulate e-p thermal transport across metal-nonmetal interfaces, which includes the non-local e-p coupling effect. We have extended the previous TTM-MD model and proposed two new models with different coupling mechanism to interpret the process: the “joint-mode” model and the “phonon-wavelength” model. By conducting simulations on the Cu-Si interface which are comparable with the previous study, we obtain results indicating that the proposed mechanism can slightly enhance interfacial thermal transport. The total TBR is reduced by 18% if the cross-interface e-p coupling is considered. Based on the TTM-MD results, we construct a mixed series-parallel thermal circuit, where the e-p coupling resistance in the metal side of the joint-modes region is in series with the p-p resistance, and they together are in parallel with the e-p coupling resistance in the dielectric side of the joint-modes region. As a comparison, the simple series circuit that

neglects the cross-interface e-p coupling slightly over-estimates the interfacial resistance, while the simple parallel circuit under the Overhauser picture under-estimates the total interfacial resistance. Knowing electron and phonon temperature profiles and the corresponding thermal circuit is essential to understand metal-dielectric interfacial thermal transport. And we expect our model can help people better understand the thermal transport physics at such interfaces, and our simulation tool can be put into more practical use once the non-local e-p coupling physics becomes clear.

5. FIRST-PRINCIPLES CALCULATIONS OF ELECTRON-PHONON COUPLING PROPERTIES IN PURE METALS

5.1 Introduction

In TTM, the most important parameter is the electron-phonon (e-p) coupling factor G_{ep} . It determines the validity of the theory and reliability of calculation approaches developed. One practical and straightforward approach to obtain these data is to get them from experiment measurements. However, despite the fact that the experiment conditions are difficult to control, many properties cannot be directly acquired from measurements as well. Therefore a calculation prediction based on solid theory foundation is necessary for us to investigate the physics at such interfaces.

Previous works have shown comprehensive studies focusing on prediction of the e-p coupling properties in pure metals based on first-principles density functional theory (DFT) calculations [36, 129, 151–157]. In this chapter I will present my calculation of Cu based on DFT. Similar to Chapter 2, this work also serves as a foundation for future works in chapter 6.

5.2 Theory

As is mentioned in the introduction, the e-p energy transfer rate can be calculated based on FGR:

$$\frac{\partial E_{ep}}{\partial t} = \frac{4\pi}{\hbar} \sum_{k,k'} \hbar\Omega_q |M_{kk'}|^2 S(k, k') \delta(\varepsilon_k - \varepsilon_{k'} + \hbar\Omega_q). \quad (5.1)$$

According to the Eliashberg theory, a spectrum function for the e-p scattering can be defined as the Eliashberg function:

$$\alpha^2 F(\varepsilon, \varepsilon', \Omega) = \frac{2}{\hbar g(\varepsilon_F)} \sum_{k,k'} |M_{kk'}|^2 \delta(\varepsilon_k - \varepsilon_{k'} + \hbar\Omega_q). \quad (5.2)$$

Then Eq. (5.1) becomes

$$\frac{\partial E_{ep}}{\partial t} = 2\pi g(\varepsilon_F) \int_0^\infty d\Omega \hbar \Omega \int_{-\infty}^\infty d\varepsilon \times \alpha^2 F(\varepsilon, \varepsilon', \Omega) [f(\varepsilon) - f(\varepsilon')] [n(\varepsilon' - \varepsilon, T_e) - n(\hbar\Omega, T_p)], \quad (5.3)$$

where $\varepsilon' = \varepsilon + \hbar\Omega$. Usually a more useful fermi-surface-averaged Eliashberg function $\alpha^2 F(\Omega)$ is used instead [151, 158]. Then Eq. (5.3) can be rewritten as:

$$\frac{\partial E_{ep}}{\partial t} = 2\pi g(\varepsilon_F) \int_0^\infty d\Omega \hbar \Omega \alpha^2 F(\Omega) [n(\hbar\Omega, T_e) - n(\hbar\Omega, T_p)] \int_{-\infty}^\infty d\varepsilon [f(\varepsilon) - f(\varepsilon')], \quad (5.4)$$

The integral with respect to ε can be done by considering the fact that ε varies at a much larger scale than $\hbar\Omega$ so that $f(\varepsilon) - f(\varepsilon') \cong f'(\varepsilon) \hbar\Omega$. And $\partial E_{ep}/\partial t = G_{ep}(T_e - T_p)$. If we take the limit that the difference between T_e and T_p is infinite small, then the EPC factor G_{ep} can be expressed as:

$$G_{ep} = 2\pi g(\varepsilon_F) \int_0^\infty \alpha^2 F(\Omega) (\hbar\Omega)^2 \frac{\partial n(\hbar\Omega, T)}{\partial T} d\Omega. \quad (5.5)$$

The e-p mass enhancement factor λ can be expressed as:

$$\lambda = 2 \int_0^\infty \alpha^2 F(\Omega) \Omega d\Omega, \quad (5.6)$$

These equations serve as the foundation for a first-principles calibration of the e-p coupling properties in metallic systems. Many studies have performed calculations based on the above theory. In the later section of this thesis I will extend these theories to perform new calculations.

5.3 Cu case study

Copper is chosen as the material to perform these calculations as an example because of its broad range of application in electronic devices.

The QUANTUM ESPRESSO package is used for performing the DFT based first-principles calculations. Ultrasoft pseudopotential based on LDA is chosen for Cu [159]. Optimization of the unit cells gives a bulk a_0 of 3.552 Å. Calculation of the e-p scattering matrix is done with respect to the k -point discretization mesh of the first

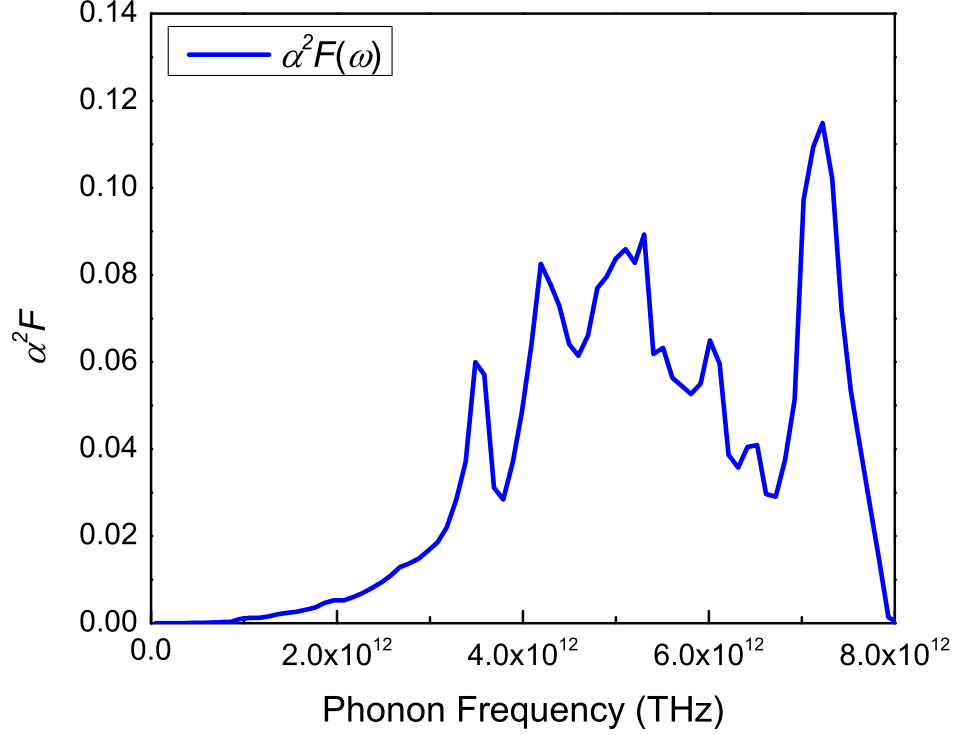


Figure 5.1. Eliashberg function of bulk Cu. The result agrees with previous literature.

Brillouin Zone. A convergence study shows that the results reach steady values after the mesh of the first Brillouin zone is denser than $8 \times 8 \times 8$. Eventually a $16 \times 16 \times 16$ grid is used.

The Eliashberg function for bulk Cu is shown in Fig. 5.1. λ is calculated to be 0.12, while G_{ep} is found to be 8.58×10^{16} W/m³K. G_{ep} 's accumulation with phonon frequency is shown in Fig. 5.2. And a “normalized G_{ep} ” is defined as $G_{ep}(\omega)$ over the phonon DOS. The physical significance of this term is the coupling strength of phonons to the electrons with respect to their frequencies while regardless of their population. And the results show that generally phonons with higher frequencies couple stronger to electrons. The electron-phonon scattering rate is also calculated with respect to the k -point mesh, details and further study into its effect on the material thermal conductivities can be found in Ref. 160.

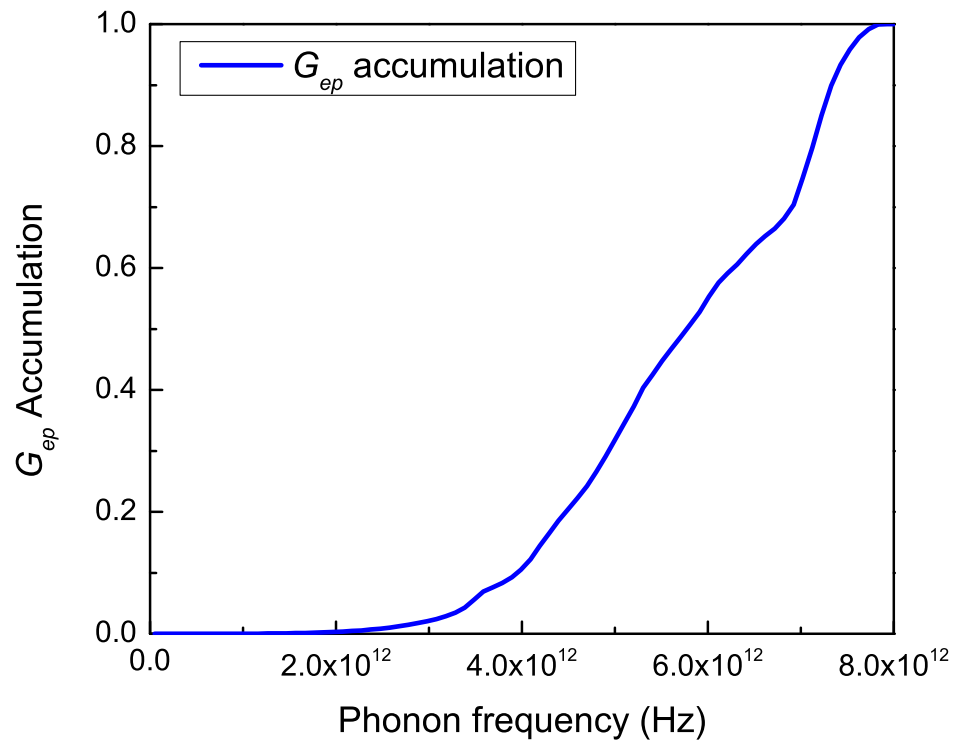


Figure 5.2. The accumulation of G_{ep} with phonon frequency in bulk Cu.

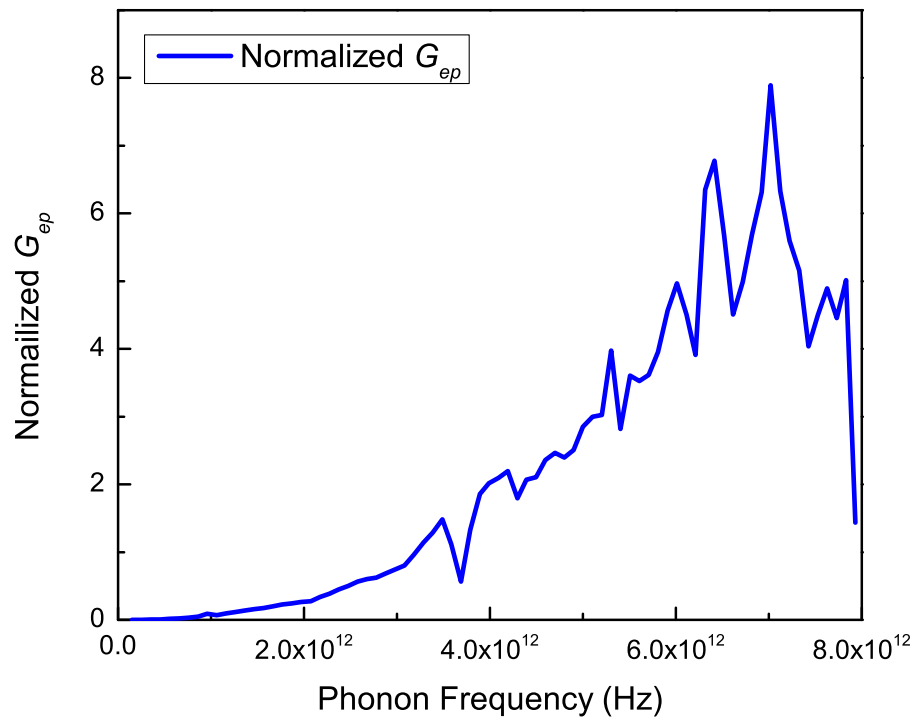


Figure 5.3. The normalized G_{ep} over the phonon DOS. Generally the coupling is stronger as the phonon frequency gets higher.

6. NON-LOCAL ELECTRON-PHONON COUPLING IN PURE METALS MANIFESTED BY SIZE EFFECT BASED ON FIRST-PRINCIPLES CALCULATIONS

6.1 Introduction

In Chapter 4 we have presented a preliminary model for non-local electron-phonon (e-p) coupling and developed a tool which is capable of running simulation including this new physics. However, the details of this non-local e-p coupling mechanism remains unknown to us and few works have been done on this topic. My eventual goal is to elaborate the thermal transport at metal-dielectric interfaces by considering more physics, and to achieve this the investigation of non-local e-p coupling is essentially necessary. Therefore in this chapter I will talk about my work so far on this topic.

In the two-temperature model (TTM), the e-p coupling process has been generally considered as local, i.e., electrons and phonons can only interact at the same location, despite the fact that Coulomb interaction, which is the cause of e-p coupling, is a long-range effect. This is warranted by the fact that in bulk materials the size is much larger than the Coulomb range, such that a non-local treatment of e-p coupling is unnecessary. Indeed, the local coupling picture has enjoyed great success in predictions and explanations of the experimental results in bulk materials [36, 162, 163]. However, controversies have arisen for metal-dielectric heterogeneous systems. Modern electronic devices, e.g. the heat-assisted magnetic recording (HAMR) devices and transistors [1–3], feature many metal-dielectric interfaces. Usually the metal elements operate at a high temperature and dissipate heat to the dielectric heat sinks. Achieving high interfacial conductance will help keep the electronic devices cool. Experiments have shown that the interfacial thermal conductances measured at several metal-diamond interfaces significantly exceed the value when only consid-

ering elastic phonon transmission across the interface [9,10]. Two possible additional energy transport channels have been proposed: one attributes the high conductance to inelastic phonon transmission at the interface [10–15], while the other hypothesizes that electrons in the metal can couple to phonons in the dielectric [9,16–20], which is essentially a specific form of non-local e-p coupling. However, no consensus has been reached, due to the lack of direct theoretical or experimental assessment whether non-local e-p coupling is significant, and if so what the coupling distance is. Although first principles calculations have been used widely to calculate the bulk G_{ep} of metals [6,129,151,153,160,164–166], assessing whether the e-p coupling is non-local remains an unsolved question.

In this study, we use first principles calculations on delicately-designed systems to directly assess the non-local e-p coupling phenomenon in Al, Cu and Ag [167]. We first calculate Al thin films and observe interesting size effect of the e-p coupling factor, which leads us to establish the existence of non-local e-p coupling. A spatial e-p coupling strength distribution function is then constructed. We have found that electrons can couple non-locally to phonons at a distance on the order of 1 nm. The work is expected to offer new non-local perspectives to many physical processes involving e-p coupling.

6.2 Case study of Al: size effect of electron-phonon coupling manifested

We start off looking for evidences of non-local e-p coupling. Bulk systems cannot be used since the size is much larger than any coupling distance so that the observables will not be sensitive to any non-local effect. However, we hypothesize that if a free-standing thin film is considered and the thickness is smaller than the non-local coupling distance, we should observe a size effect. Consider electrons at a given location, the coupling strength will be the largest for phonons at the same location, and it will decay for phonons farther away. When the film thickness becomes smaller than the coupling distance, some of the non-local coupling will be truncated. This

hypothesis is illustrated in Fig. 6.1. The in-plane direction of the system is infinite large so that the analysis can be simplified to 1D. The e-p coupling strength distribution function (CSDF) $G'_{ep}(x)$ is defined as G_{ep} per unit length. Cases a) and b) show that if e-p coupling is local, $G'_{ep}(x)$ would be a delta function at the positions of electrons. $G_{ep}(x)$, which represents the local G_{ep} at x , is a constant. The overall G_{ep} of a metal thin film would be the same as the bulk regardless of the film thickness. On the other hand, if e-p coupling is non-local, as is shown in cases c) and d), $G'_{ep}(x)$ has a non-zero spatial distribution and is truncated at the boundaries. As a result, $G_{ep}(x)$ becomes smaller near the boundaries and the overall G_{ep} in thin films will be smaller than its bulk value. Therefore, checking the size effect on G_{ep} will allow us to check the existence of non-local coupling. Aluminum is chosen since it has strong e-p coupling [168].

A comparative study between bulk Al and a free-standing Al thin film with only one layer of unit cell (two layers of atoms in the (100) plane) is performed. In order to make comparisons between corresponding phonon branches, the simulation uses one face-centered cubic unit cell containing 4 Al atoms as the “primitive cell” for both cases. As a result, there are 12 corresponding phonon branches in each case. A norm-conserving pseudopotential developed based on local density approximation (LDA) is used [159]. Calculation is preformed using the QUANTUM ESPRESSO package [169]. Optimization of the unit cells gives a lattice constant of $a_0 = 3.953$ Å for the bulk case, while the 1-layer case a_0 has 7.3% expansion in the out-of-plane direction and 4.7% shrinkage in the in-plane direction. Phonon and e-p coupling calculations are then performed on these unit cells.

A more detailed set of calculation parameters for the bulk cases is listed in Table 6.1. The simulation domains are different for bulk and 1-layer cases. For the bulk case, the simulation domain is the unit cell itself, and the periodic boundary condition in all three dimensions eventually generates a bulk metal. For the 1-layer case, the simulation domain is much larger than the unit cell in the out-of-plane direction. As a result, the infinite number of metal thin films generated by periodic boundary

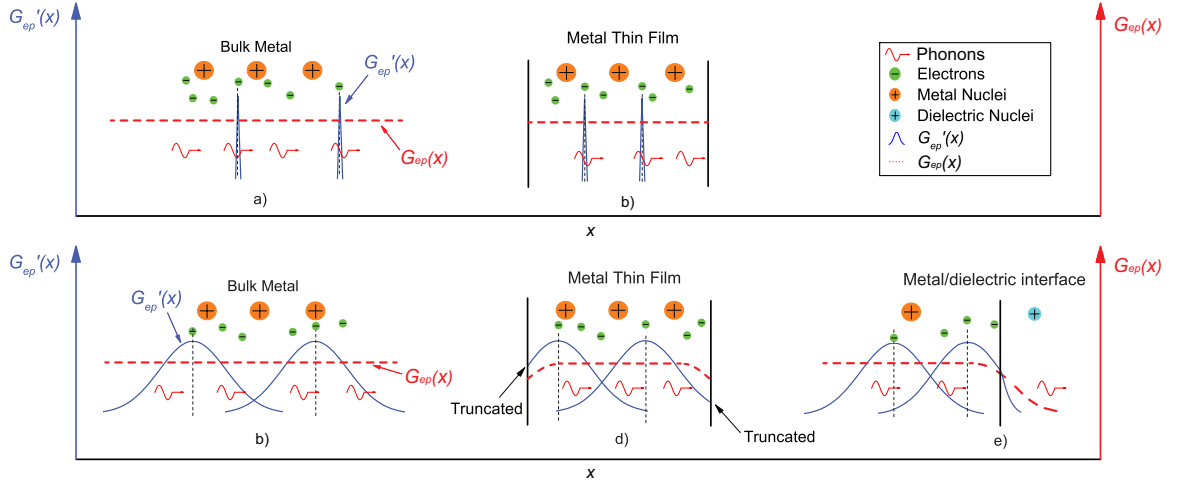


Figure 6.1. a) Local e-p coupling in bulk metal where $G'_{ep}(x)$ is delta functions at the positions of each overlapping electron and phonon. b) Local e-p coupling in a metal thin film where the overall G_{ep} is the same with the bulk. c) Non-local e-p coupling in bulk metal where $G'_{ep}(x)$ has a spatial distribution. d) Non-local e-p coupling in a metal thin film where $G'_{ep}(x)$ is truncated at the boundaries and the overall G_{ep} is smaller than the bulk. e) Non-local e-p coupling at a metal-dielectric interface where metal electrons can couple to dielectric nuclei within their coupling distance. Note $G'_{ep}(x)$'s curve may change in the dielectric.

Table 6.1.
Details of the inputs for the DFT calculations for the bulk cases

Metal	Lattice constant after optimization	k-grid of the first Brillouin zone	Wavefunction cutoff radius	Charge density cutoff range
Al	3.953 Å	$16 \times 16 \times 16$	10.584 Å	127.003 Å
Cu	3.552 Å	$16 \times 16 \times 16$	26.459 Å	105.835 Å
Ag	4.111 Å	$16 \times 16 \times 16$	15.875 Å	95.252 Å

Table 6.2.
Details of the inputs for the DFT calculations for the 1-layer cases

Metal	In-plane lattice constant after optimization	Length of unit cell in out-of-plane direction	k-grid of the first Brillouin zone
Al	3.767 Å	131.852 Å	$32 \times 32 \times 1$
Cu	3.394 Å	118.795 Å	$32 \times 32 \times 1$
Ag	3.960 Å	118.811 Å	$32 \times 32 \times 1$

conditions are separated by a distance identical to the length of the simulation domain which is larger than the potential's cutoff range. Therefore these thin films cannot interact with each other and can be considered as free-standing. For the 1-layer cases, the same cutoff radii for potentials are used for each metal with its bulk case respectively. The length of the simulation domain is chosen as an integral multiple of the lattice parameter, e.g. for Al it is 35 times. The in-plane direction of the first Brillouin zone has 32×32 k points while the out-of-plane direction only has 1 k point. Details are listed in Table 6.2. The Methfessel-Paxton smearing with a Gaussian spreading of 0.27 eV is used for the Brillouin zone integration in these metals [170].

The phonon dispersions of 1-layer and bulk Al are shown in Fig. 6.2. As is observed from the figure, the phonon branches with lower frequencies have significant differences. They either have large frequency shift or have different frequency spans, rendering them not comparable. The overall G_{ep} of the 2 cases are similar, however the electron density of states (DOS) significantly differ from each other. A summary of some supplementary results of Al, Cu and Ag calculations can be found in Table 6.4. The results of 1-layer Al agree well with previous literature [168], indicating that our results are reliable.

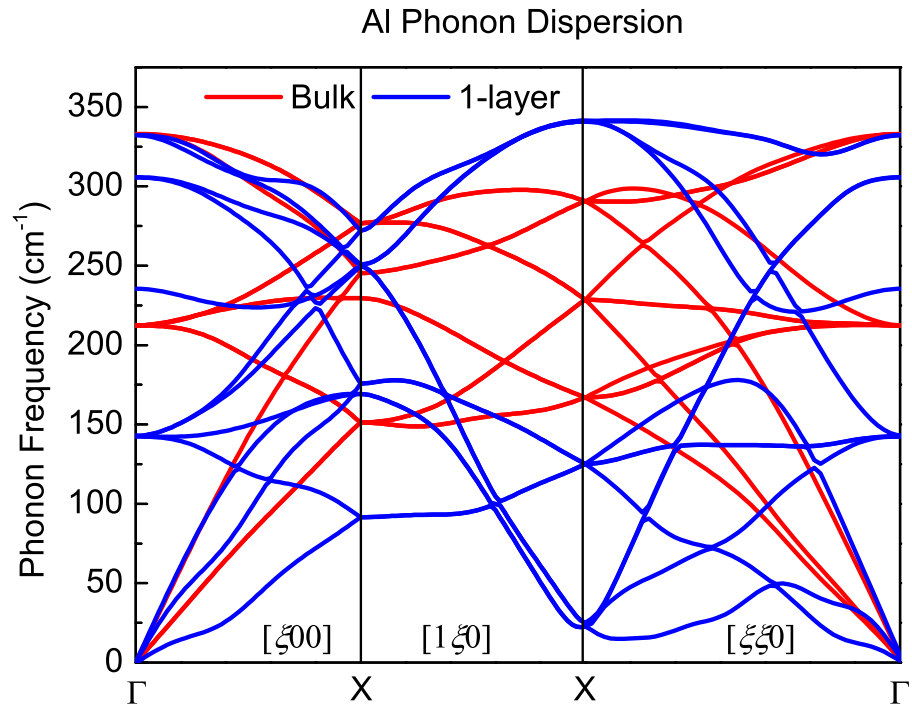


Figure 6.2. The phonon dispersion of bulk and 1-layer Al. There are 4 atoms in one “primitive cell” so there are altogether 12 phonon branches. Most of the low frequency phonons have frequency shifts and different frequency spans in these two cases, while the high frequency branches are much more similar, especially along the Γ -X line.

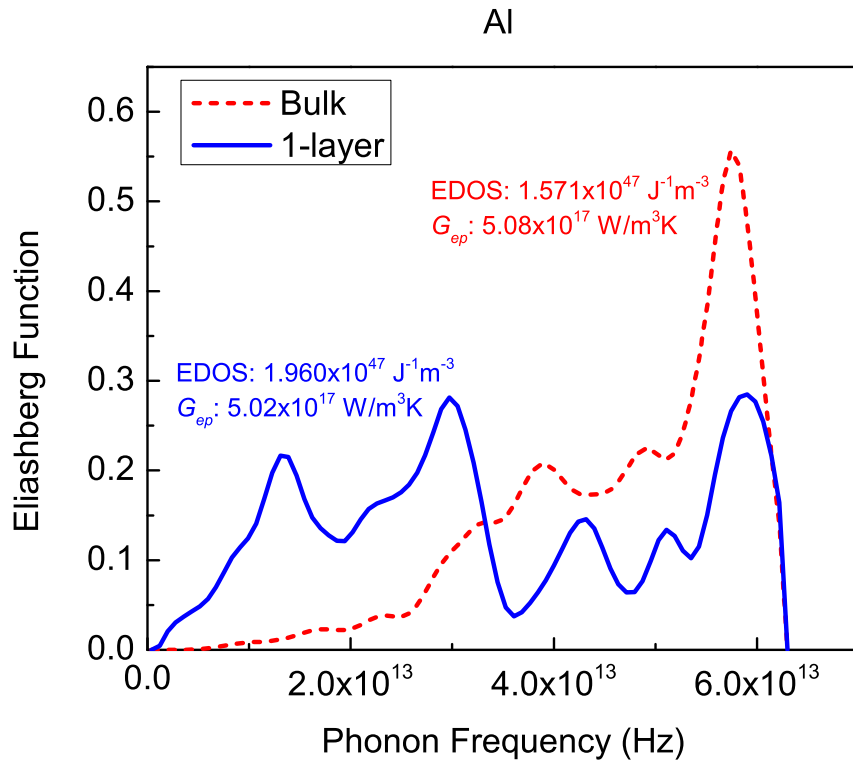


Figure 6.3. The Eliashberg function of bulk and 1-layer Al. Due to the changes in phonon dispersion, the shapes of the function curves are significantly different. The overall coupling factors are similar while the electron DOS deviates, indicating that the actual coupling strengths are different in these two cases.

The Eliashberg functions of the two cases, which define the spectrum of the e-p coupling strength with respect to the phonon frequency [129, 151, 153, 171], are shown in Fig. 6.3. Although the overall G_{ep} 's are similar, the curve shapes are significantly different, indicating that e-p coupling has strong size effect in Al. Per our hypothesis above we would conclude that e-p coupling must be non-local, however we need to be very careful since many other lattice and electronic properties have also changed from bulk to the 1-layer system. The size effect of e-p coupling cannot readily prove the non-local e-p coupling yet.

6.3 Theory

We take a closer look at the Eliashberg function $\alpha^2 F(\Omega, \varepsilon, \varepsilon')$. Here Ω is the phonon frequency, ε and ε' are the initial and final energy state of electrons respectively. Although the function changes with the electron energy, usually it is reasonable to neglect this dependence because the variation only happens at a very large scale. The electron-Fermi-surface-averaged Eliashberg function $\alpha^2 F(\Omega, \varepsilon_F, \varepsilon_F)$ which only depends on phonon frequency is often used [151, 158]. $F(\Omega)$ represents the phonon DOS, while α^2 can be conceived as the “spectral coupling strength”. Then the expression for G_{ep} is:

$$G_{ep} = 2\pi g(\varepsilon_F) \int_0^\infty \alpha^2 F(\Omega) (\hbar\Omega)^2 \frac{\partial n(\hbar\Omega, T)}{\partial T} d\Omega, \quad (6.1)$$

where $g(\varepsilon_F)$ is the electron DOS at the Fermi surface, T is temperature and n is the Bose-Einstein distribution. Eq. (6.1) expresses G_{ep} as the derivative of the energy transfer rate between electrons and phonons with respect to temperature, and it quantifies how the coupling strength depends on several parameters together. Therefore in order to extract the size-truncation information, we need to isolate the dependencies on other factors: phonon DOS, electron DOS, phonon dispersion and electron band structure.

6.3.1 The partial coupling strength

The definition of $\alpha^2 F(\Omega)$ ensures that it is independent of the electron DOS. To isolate the two phonon factors, we use the idea of partial phonon DOS which describes the phonon DOS with respect to individual phonon branches. We calculate the partial Eliashberg function and further define a new term: the partial e-p coupling strength α_v^2 . The partial phonon DOS of a specific branch v is defined as [172]:

$$F_v(\Omega) = \sum_q^v \delta(\Omega - \Omega_{qv}), \quad (6.2)$$

where q refers to the phonon wave vector. Based on this, α_v^2 is defined as:

$$\alpha_v^2(\Omega) = \frac{\alpha_v^2 F_v(\Omega)}{\sum_q^v \delta(\Omega - \Omega_{qv})}, \quad (6.3)$$

where $\alpha_v^2 F_v(\Omega)$ is the partial Eliashberg function of phonon branch v . It can be easily seen that through these definitions the partial e-p coupling strength α_v^2 is allocated with respect to individual phonon branches while normalized by the corresponding phonon DOS.

At this point only one factor remains to be isolated: the electron band structure. Calculation of the e-p coupling with resolved electron bands can be very cumbersome and not practical. In this study we apply an approximation that has been used in the literature [129, 173], that the e-p scattering, when averaged over all angles, is independent of electron states. Then the scattering at a specific electron state is only dependent on the corresponding electron DOS, and the Eliashberg functions have the following relationship:

$$\frac{\alpha^2 F(\varepsilon, \varepsilon', \Omega)}{g(\varepsilon)g(\varepsilon')} = \frac{\alpha^2 F(\varepsilon_F, \varepsilon_F, \Omega)}{g(\varepsilon_F)g(\varepsilon_F)}. \quad (6.4)$$

Therefore we further normalize α_v^2 with the corresponding electron DOS again and define the normalized partial e-p coupling strength:

$$\alpha_{v,norm}^2 = \frac{\alpha_v^2}{g(\varepsilon_F)^2}. \quad (6.5)$$

Now it only contains the size-truncation information caused by non-local e-p coupling on a single phonon branch.

Table 6.3.
Reduction factor of $\alpha_{v,norm}^2$ of phonon branch 11 and 12
in Al

Phonon branches	Reduction factor
11	52.59%
12	50.22%

6.4 Results: the non-local electron-phonon coupling properties in Al

Our results show that the $\alpha_{v,norm}^2$ of low frequency phonon branches are significantly different in the bulk and 1-layer case, while the high frequency branches show excellent similarities. The two optical branches with the highest frequencies, i.e. Branch 11 and 12, have similar frequency spans and distributions within this range in each case, indicating that their dispersions have not changed with the system. Therefore they are chosen to calibrate the non-local e-p coupling properties. From Fig. 6.4, the amplitude of $\alpha_{v,norm}^2$ in the 1-layer case is significantly smaller than the bulk case, which is expected because the coupling should be weaker in the thin film due to size truncation effect. By taking the average of the $\alpha_{v,norm}^2$ within its frequency range we can calculate the ratio of $\alpha_{v,norm,1-layer}^2/\alpha_{v,norm,bulk}^2$ on the same phonon branch, which we define as the “reduction factor” (RF). Then we are able to get the following values in Table 6.3. RF represents the significance of the size-truncation effect, and an RF smaller than 1 indicates the existence of non-local e-p coupling.

Now we use this reduction factor to reconstruct the CSDF. We assume that all the phonon branches have the same CSDF, and propose a Gaussian-distribution function to describe the non-local coupling distribution, i.e. electrons can couple to phonons at a distance, but with decaying strength. The expression of $G'_{ep}(x)$ is:

$$G'_{ep}(x) = G'_0 \exp\left(-\frac{x^2}{2\sigma^2}\right), \quad (6.6)$$

where G'_0 and σ are unknown parameters that need to be fitted. We also define

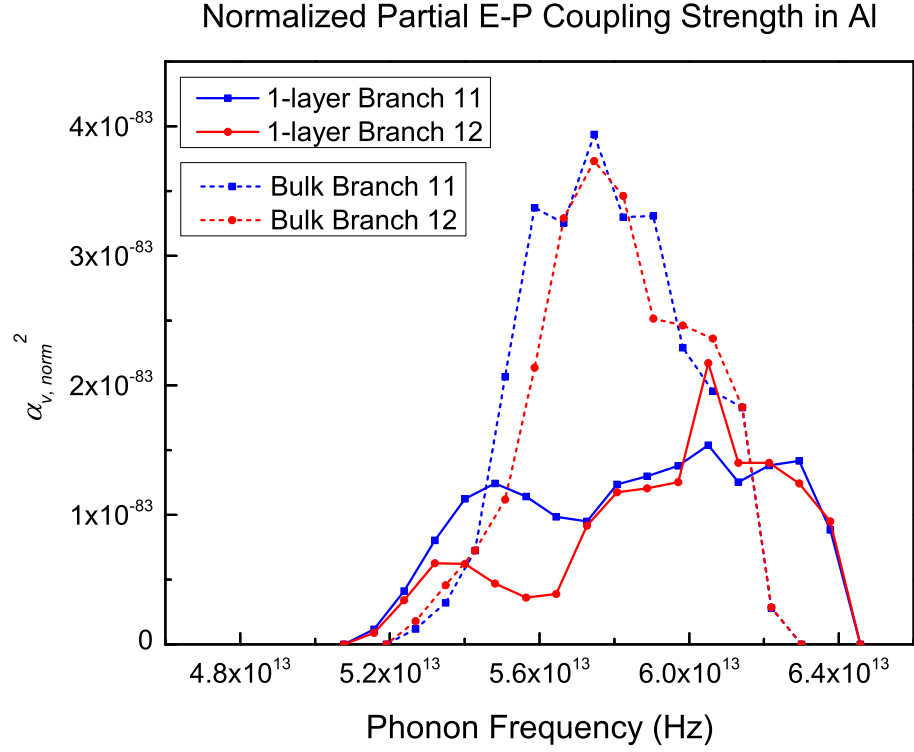


Figure 6.4. $\alpha_{v, norm}^2$ phonon branch 11 and 12 in bulk and 1-layer Al. The two optical phonon branches have similar frequency spans and shapes of curve.

$G'_{ep}(x)$'s integral over length as G_{cumu} :

$$\frac{1}{2}G_{cumu}(x) = \int_0^x G'_{ep}(t)dt = \sqrt{\frac{\pi}{2}}\sigma G'_0 \text{erf}\left(\frac{x}{\sqrt{2}\sigma}\right). \quad (6.7)$$

Then in bulk materials, the e-p coupling factor can be expressed as:

$$G_{ep} = \frac{\int_{-\infty}^{\infty} dx \int_{-\infty}^{\infty} dy G'_{ep}(y-x)}{\int_{-\infty}^{\infty} dx} = G_{cumu}(\infty), \quad (6.8)$$

However, for a system with finite size the integral will be cut off at the system's "effective boundaries" which are $a'_0/4$ outside the boundary atomic layers, where a'_0 is the lattice constant of the system. Here we assume electrons and phonons only exist within the effective boundaries. As for our 1-layer Al, the actual coupling range of an electron is shown in Fig. 6.5. Then for the 1-layer Al in our calculation, the overall coupling factor is:

$$\frac{\int_{-\frac{a'_0}{2}}^{\frac{a'_0}{2}} dx \int_{-\frac{a'_0}{2}}^{\frac{a'_0}{2}} G'_{ep}(y-x)dy}{\int_{-\frac{a'_0}{2}}^{\frac{a'_0}{2}} dx} = \frac{\int_0^{a'_0} G_{cumu}(z)dz}{a'_0}. \quad (6.9)$$

The ratio $\int_0^{a'_0} G_{cumu}(t)dt/(a'_0 G_{cumu}(\infty))$ corresponds to the values in Table 6.3. The fitting yields $\sigma = 0.70a_0 = 0.28$ nm and $G'_0 = G_{ep}/\sqrt{2\pi}\sigma = 7.32 \times 10^{26}$ W/m⁴K. The $G'_{ep}(x)$ of Al is shown in Fig. 6.6. The coupling strength still has 77% of its maximum value at a distance of $a_0/2 = 0.20$ nm. This means electrons in Al have significant non-local coupling to all phonons in its vicinity. We can define 3σ as the coupling distance, because the accumulated coupling strength within this range is >99% of its total value. For Al this coupling distance is $2.1a_0$, or 0.83 nm.

We anticipate that our findings will have significant implications. In electronic devices, heat generation and dissipation at metal-dielectric interfaces become a critical issue, and our study can provide new insights in developing solutions. The existence of non-local e-p coupling implies that heat can be generated no longer only at the locations of electrons, but also at remote locations within the coupling distance. It can also enable the direct heat transfer from hot electrons in the metal to phonons

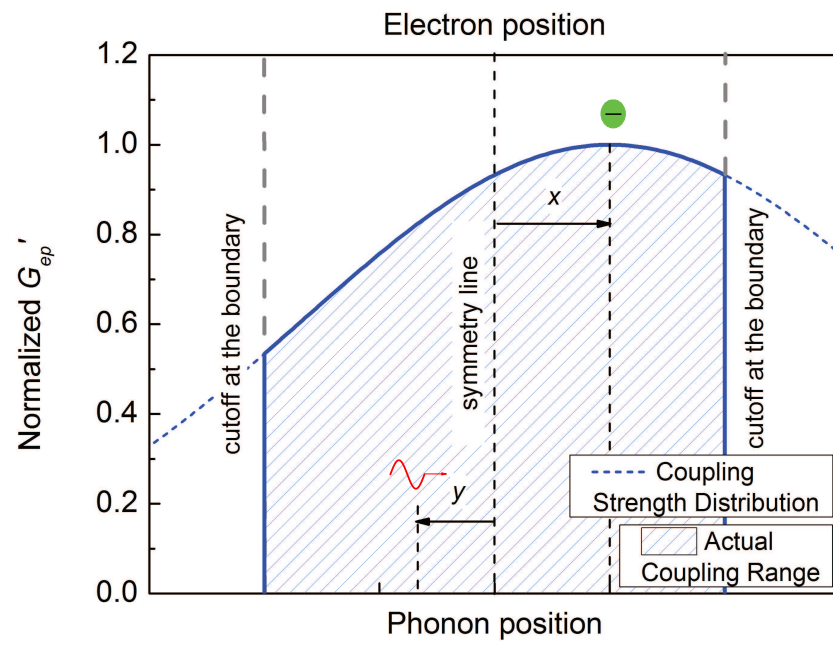


Figure 6.5. The actual coupling range of one electron in 1-layer Al. The distribution is cut off at the “effective boundary” of the material.

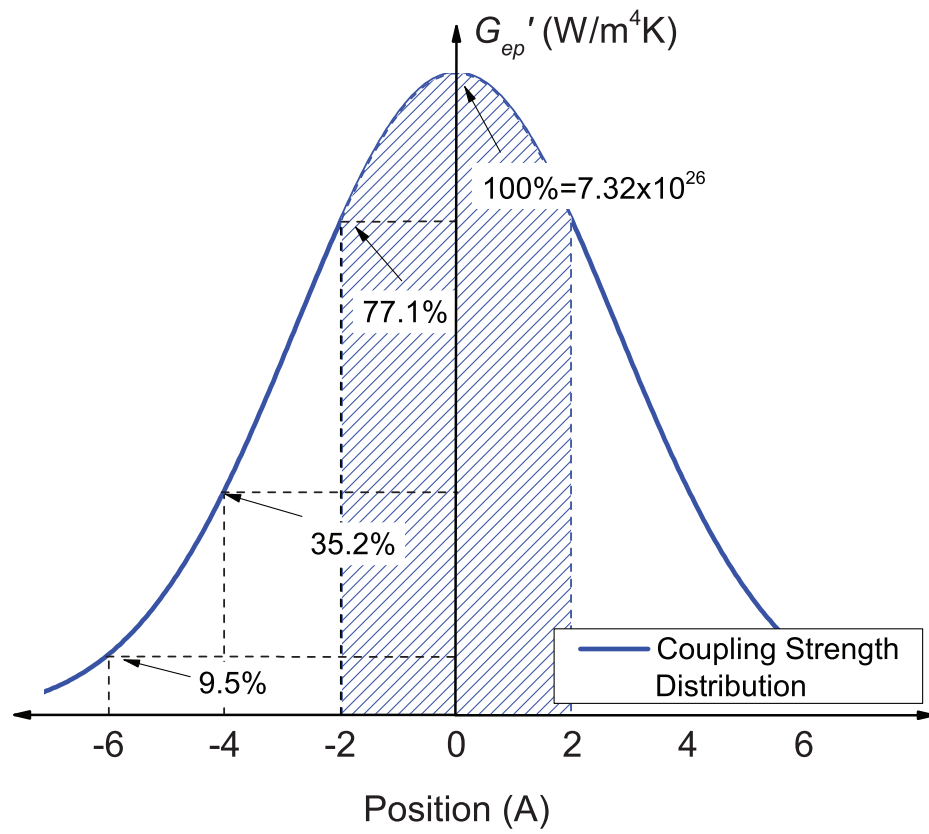


Figure 6.6. CSDF in Al. The standard deviation of the Gaussian function is 0.28 nm. The shaded area represents the truncated CSDF of a electron located in the center of 1-layer Al.

in the dielectric as a new heat dissipation mechanism, as shown in Fig. 6.1 e). Consequently the metal elements will operate at a decreased temperature with increased performance and reliability. Although our present work is on pure metal, we can make a first-order estimation on its impact on interfacial conductance by assuming that the CSDF stays the same for the interface system. The thermal conductance enabled by the non-local e-p coupling mechanism of Al is h of $\sqrt{\pi}\sigma^2G'_0 = 100 \text{ MW/m}^2\text{K}$:

$$h = \int_{-\infty}^0 dx \int_0^{\infty} G'_{ep}(y-x)dy = \sqrt{\pi}\sigma^2G'_0. \quad (6.10)$$

Compared with typical metal-dielectric h 's of 200-700 MW/m²K [11, 99, 174], this is a considerable improvement to interfacial thermal transport. Still, further work is warranted to investigate whether CSDF is the same for all phonon branches and how it changes in different materials across the interface. In addition, our model can be readily applied to improve the original local TTM to a non-local TTM by modifying the space-independent G_{ep} to a space-dependent $G_{ep}(x)$, expressed as:

$$G_{ep}(x) = \int_{-\frac{L}{2}}^{\frac{L}{2}} G'_{ep}(t-x)dt, \quad (6.11)$$

where L is the length of the system. It is straightforward to verify that for a large system where $L \rightarrow \infty$, away from the boundaries $G_{ep}(x) = G_{cumu}(\infty) = G_{ep,bulk}$, and it decreases as x approaches $L/2$ and eventually becomes $G_{ep}(L/2) = G_{ep,bulk}/2$, as is shown in Fig. 6.1 d). With the CSDF in hand, one can calculate $G_{ep}(x)$ in the entire system and replace the G_{ep} in the original TTM equations [18]. Moreover, our work will provide new insights to many other systems where e-p coupling is concerned, such as hot electron relaxation through phonons in core-shell quantum dots for photovoltaic applications [175].

6.5 Case study of Cu and Ag

We also apply our model on two other metals: Cu and Ag. They are elements of the same group and thus have similar electronic structures. The simulation details are included in the supplementary material. The phonon dispersions of Ag and Cu

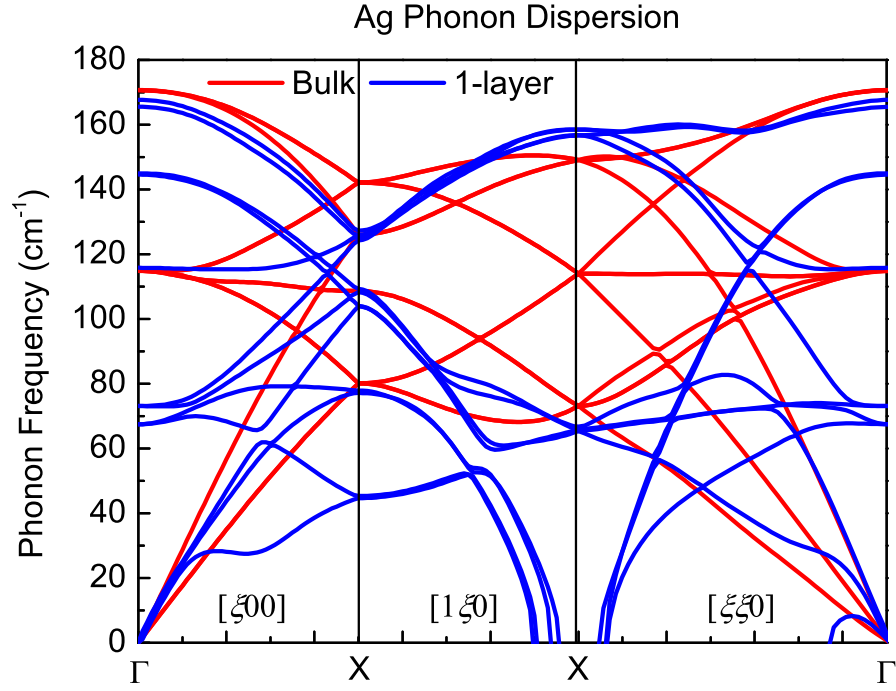


Figure 6.7. The phonon dispersion of bulk and 1-layer Ag. Different from the Al case, the phonon dispersion have changed significantly. Even the high frequency phonons don't have excellent overlap along the Γ -X line. It is also worth noting that results of the low frequency phonon branches near the $[110]$ point is not very reliable, but this does not affect our result because we are only using the high frequency phonon branches for calculation.

are shown in Fig. 6.7 and 6.8. Compared with the Al case, the phonon branches in Ag and Cu change more significantly when the metal changes from bulk to 1-layer film, making it difficult to find corresponding phonon branches with excellent overlap even at high frequencies. The Eliashberg functions of Ag and Cu are shown in Fig. 6.10 and 6.11. Some supplementary results are also shown in Table 6.4.

The $\alpha_{v,norm}^2$ function plots for phonon branch 11 and 12 in Ag and Cu are shown in Fig. 6.9. We can see the overlap is not as good as Al, which means the phonon branches have changed significantly even at high frequency. However our model can still be applied to get an approximated result, where the non-local e-p coupling properties are calibrated using the average of the $\alpha_{v,norm}^2$ reduction factor of phonon branch 11 and 12. We notice that for Cu, the coupling distance of 3σ is approximately 0.4

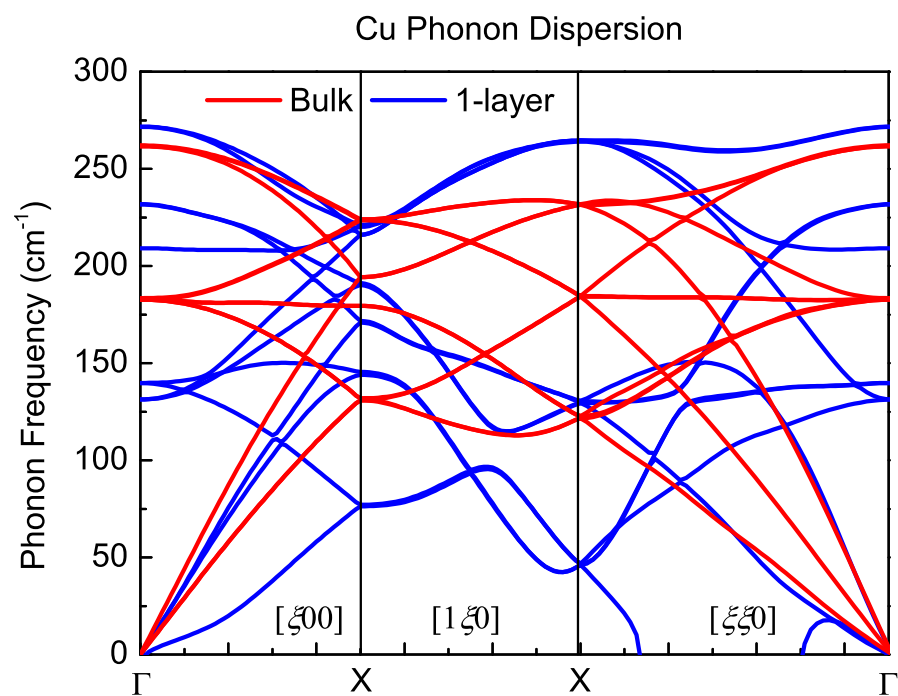


Figure 6.8. The phonon dispersion of bulk and 1-layer Cu. The physical significance is similar with the Ag case.

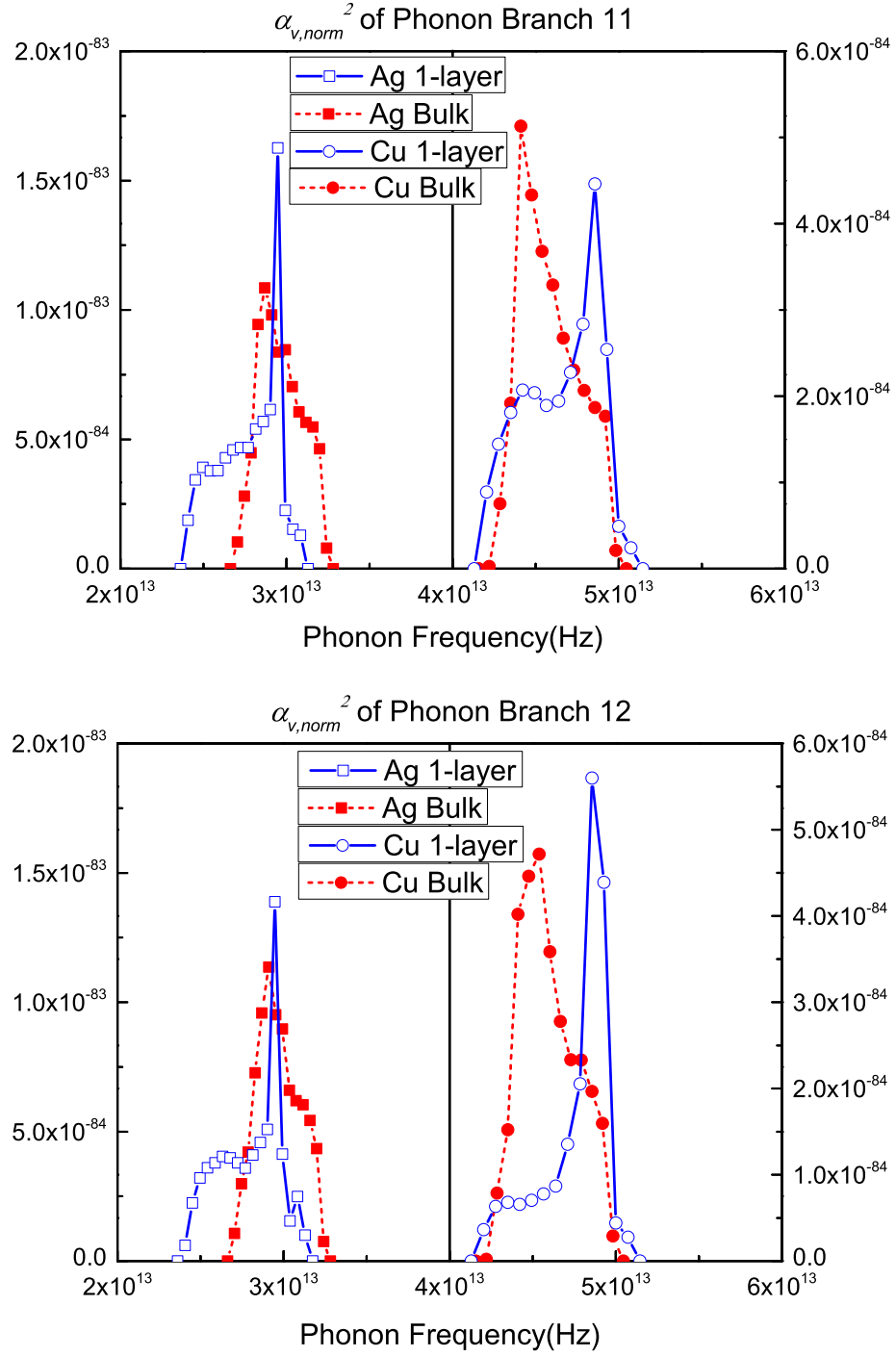


Figure 6.9. $\alpha_{v,norm}^2$ of Branch 11 and 12 in Ag and Cu. The non-local e-p coupling is less significant than in Al, and the peak value of $\alpha_{v,norm}^2$ is even higher in 1-layer case, but the overall coupling strength in 1-layer is smaller than the bulk value.

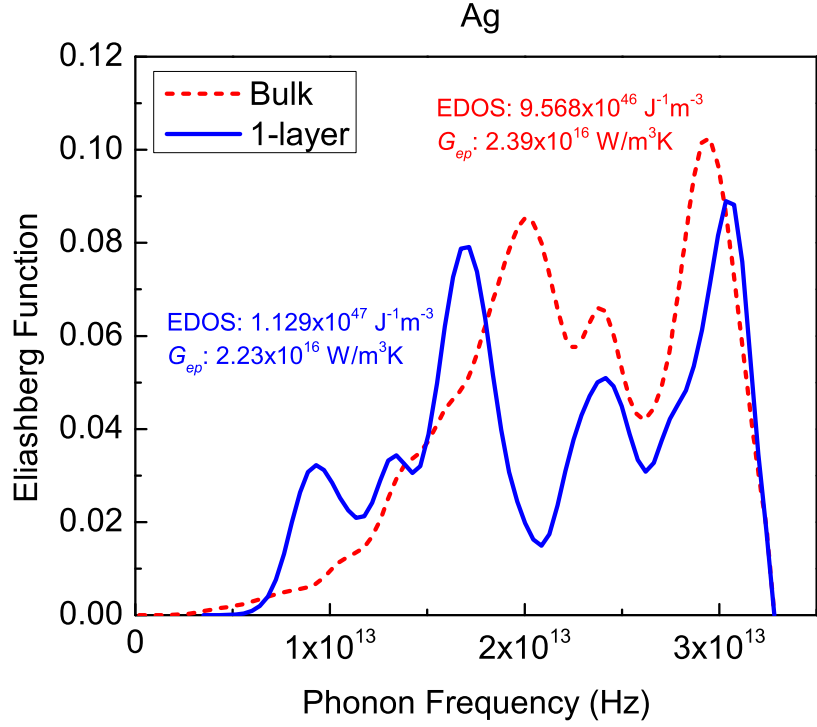


Figure 6.10. The Eliashberg function of bulk and 1-layer Ag.

Table 6.4.

A summary of the results of e-p coupling in Al, Cu and Ag

	$g(\varepsilon_F)(10^{47} \text{ J}^{-1} \text{ m}^{-3})$		$G_{ep}(10^{16} \text{ W/m}^3 \text{ K})$		λ	
	Bulk	1-layer	Bulk	1-layer	Bulk	1-layer
Al	1.571	1.960	50.8	50.2	0.3988	0.7517
Cu	1.661	1.988	8.58	6.81	0.1169	0.1420
Ag	0.957	1.129	2.39	2.23	0.1214	0.1533

nm, which validates our previous hypothesis that electrons can couple to phonons within a range of phonon wavelength rather than the phonon mean free path. [18]. Finally, it is noteworthy that our approach, while working well in Al, does not perfectly apply in Cu and Ag, because the phonon branches have changed significantly and this makes it difficult to find comparable branches to calculate the RF. This posts some limitation to our model, as it may not be applicable to every material.

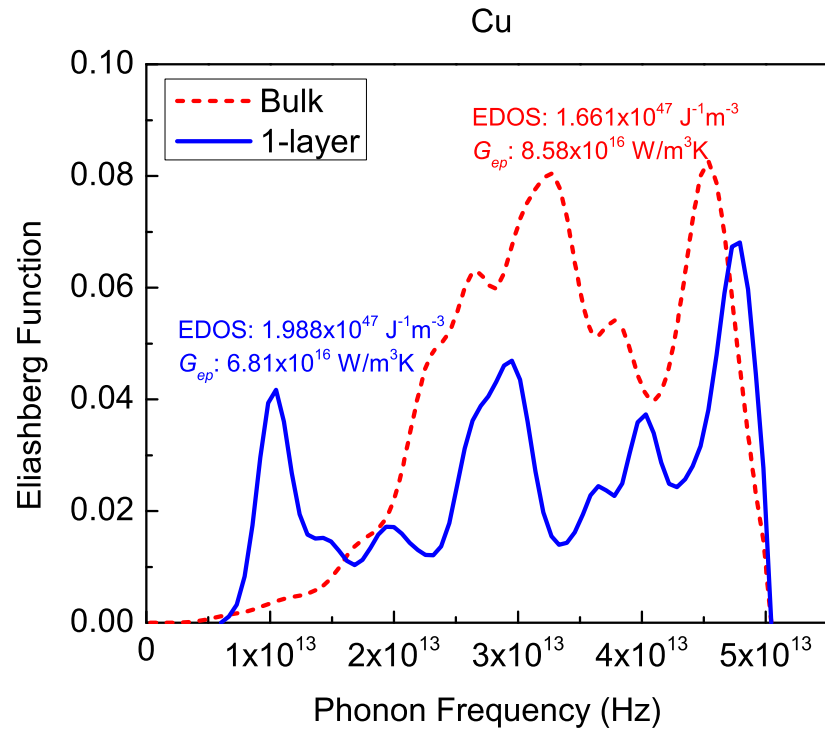


Figure 6.11. The Eliashberg function of bulk and 1-layer Cu

Table 6.5.
Non-local e-p coupling properties of Cu and Ag

	Cu	Ag
Branch 11 RF	83.04%	75.87%
Branch 12 RF	61.81%	64.14%
3σ (nm)	0.37	0.49
G'_0 (W/m ⁴ K)	2.75×10^{26}	5.80×10^{25}

We find that the non-local e-p coupling in Cu and Ag is not as strong as in Al, with coupling distances of 0.37 nm and 0.49 nm respectively. An interesting finding is that the corresponding values in Table 6.5 from Cu and Ag are similar, as are the shapes of the $\alpha_{v,norm}^2$ functions. Therefore we suspect that elements with similar electronic structures have similar non-local e-p coupling properties, regardless of the difference in their atomic masses.

6.6 Conclusions

In summary, we have identified the non-local e-p coupling phenomenon in Al, Cu and Ag, and presented a quantitative description based on first-principles calculations. The size effect of e-p coupling is first observed through calculations on Al films of different sizes. The CSDF is then defined and constructed. Calculation results show that the non-local e-p coupling is significant in Al, with a coupling distance of 0.83 nm. Cu and Ag are studied as comparisons, and weaker non-local interactions are observed, with coupling distances of 0.37 nm and 0.49 nm respectively. The CSDFs of Cu and Ag resemble each other, which suggests that elements of similar electronic structures have similar non-local e-p coupling properties. We believe our model demonstrates the significance of the non-local e-p coupling, and this can provide new insights on the electrical and thermal transport in metal-semiconductor systems.

7. MULTI-TEMPERATURE MODEL SIMULATION OF NON-EQUILIBRIUM THERMAL TRANSPORT

7.1 Introduction

So far the electron-phonon (e-p) non-equilibrium thermal transport at metal-dielectric interfaces, and the closely related non-local e-p coupling phenomenon has been investigated. However, phonon local thermal equilibrium is still assumed for all previous studies, which leaves the potential of inaccuracy. Therefore in this chapter I will look into the non-equilibrium thermal transport among phonons.

E-p coupling is an important physical phenomenon that affects Joule heating, laser-matter interaction and hot electron relaxation [7, 60, 129, 151, 153, 161, 165, 176]. The two-temperature model (TTM) has been widely used for analysis [31]. Despite the fact that all materials have multiple phonon branches which are different from each other, a simple assumption that all phonons are in thermal equilibrium with a common temperature T_p is used in TTM. However, recently it has been shown that in certain applications, such as laser heating of semiconductors and metals, phonon branches can be driven into strong non-equilibrium by selective e-p coupling, and an equilibrium picture can result in misleading or wrong interpretations [7]. For example, single-layer graphene (SLG) has drawn intensive attention among researchers due to its unique chemical and physical structures [177–181]. Theoretical calculations and experiments such as Raman measurements have been used widely to predict and measure its thermal conductivity [24, 105, 106, 182–186], but the reported values range from 600 W/mK to as high as 5800 W/mK [47–51]. Similar with most metals, TTM was used to interpret the experimental measurement and derive k [187]. However, it has been pointed out recently that this method is not accurate since different phonon branches have different coupling strength with the electrons, and their temperatures

significantly deviate from each other [7]. As a result, assuming phonon local thermal equilibrium can subsequently under-predict SLG's thermal conductivity by over 50%. It should be noted that several other mechanisms, such as imperfect experimental conditions and higher-order phonon scattering, may also contribute to the uncertainty of graphene thermal conductivity [52–55]. Several other studies on hot electron relaxation in metals or semiconductors also show that the different phonon modes are in non-equilibrium, which can significantly affect the electron cooling rates [6, 20, 28]. We can note that the steady-state phonon non-equilibrium within the cooling length region reported in Refs. 7, 8 and the transient state phonon non-equilibrium during the phonon relaxation time in Refs. 6, 20 are equivalent and due to the same physical origin: modal selective e-p and phonon-phonon (p-p) scattering.

Theoretical methods are needed to capture such modal phonon non-equilibrium. Modal and spatial Boltzmann transport equation (BTE) [56, 57, 72] and molecular dynamics combined with modal analysis [61, 75] are rigorous and accurate methods, but they are quite complicated and this hinders their access by experimentalists. Alternatively, a simple multi-temperature model (MTM) has been developed which is essentially an extension of TTM that can resolve the temperatures of different phonon branches [6, 7]. Subsequently, a detailed proof of such extension was given in Ref. 75 where the relaxation time approximation (RTA) was necessary, suggesting that MTM is rigorously valid when the separated phonon groups couple weakly. For phonon groups that couple strongly, a more rigorous way is to directly treat the scattering. However, the computation cost is high, and we believe in practice we can still use MTM by letting the phonon groups interact with a common thermal reservoir under RTA. This practice has been widely used in the spectral BTE community and the original TTM [31, 72, 78, 79]. Nevertheless, the current MTM models are either still in rather complex forms which hinder easy implementation, or only presented in the steady state. Therefore a simple and explicit approach that can capture the non-equilibrium nature among electrons and phonons is needed to accurately interpret experimental results as well as predicting electronic device performance.

In this study, we will present a general and simple phonon branch-resolved multi-temperature numerical simulation approach which can capture the non-equilibrium process between electrons and different phonon branches under both steady and transient states. The original TTM is extended to MTM with e-p coupling strength for each phonon branch. A lattice reservoir which all phonon branches scatter with is defined and the RTA is used. Based on our method, case studies of the steady-state heat transfer and transient hot electron relaxation processes in laser-irradiated SLG are presented respectively. The branch-resolved temperature profiles are shown and the degree of non-equilibrium is discussed. Finally a comparison with the original TTM is made to show the advantage of MTM.

7.2 Theory: Multi-temperature model with electron-phonon coupling

The steady-state MTM with e-p coupling has been introduced in our previous work in terms of the e-p cooling power [7]. In this work, we recast it into a more general and convenient form using the e-p coupling factor, and extend the original equations to account for the transient heat transfer process as well. Details are in the introduction chapter. Compared with our previous steady-state MTM [7], in this work we not only extend it to make the transient-state simulation possible, but also use the spectral G_{ep} instead of e-p cooling power to describe the phonon branch-resolved coupling strength, which makes our model more general and easier to use.

7.3 Case study: thermal transport in laser-irradiated single-layer graphene

In this section we will present a case study of the thermal transport process in laser-irradiated SLG.

7.3.1 Simulation domain and input parameters

We will use the same input parameter as in Ref. 7. All of the thermal properties, i.e. the thermal conductivity k , the heat capacity C , the e-p coupling factor G_{ep} and the p-p coupling factor $G_{pp,i}$ are temperature dependent. Here we report their room temperature (297 K) values, which are listed in Table 7.1. The details to obtain these values are introduced in Ref. 7 and its supplementary materials. The fact that all the $G_{pp,i}$'s are on the same order with the overall G_{ep} suggests that our previous analogy between e-p and p-p coupling in Eq. (1.11) is reasonable. The electrons have a heat capacity C_e of 3.6×10^2 J/m³K and a thermal conductivity k_e of 50 W/mK. Our result is higher than the common experimentally measured k_e which is within 10 W/mK, and we attribute this discrepancy to the absence of defects in SLG in our density functional theory calculations. The simulation is conducted on a $10 \mu\text{m} \times 10 \mu\text{m}$ SLG, with all four boundaries fixed at 297 K. The system is illustrated in Fig. 8.1. Initially the entire domain is at a uniform temperature of 297 K, when laser starts to shine at the center of the SLG sample. The expression of the laser spot is:

$$S_{laser}(r) = 0.063 \times 10^9 \times \exp(-7.744 \times 10^{16} r^2) \text{ [W/m}^2\text{]}, \quad (7.1)$$

where r (unit: m) is the distance from the center of the sample. The laser energy follows the Gaussian distribution with a laser source of 0.1 mW and a spot radius of $0.5 \mu\text{m}$. The electrons are heated up by the laser which subsequently heat up the phonons. Two cases are investigated on the same system. The first case represents the laser heating process during the Raman experiment where the laser irradiation is constant after the simulation starts. The simulation runs for 50 ns to ensure all temperatures are converged at the steady state. The second case represents a pulse laser heating process which is common in time-domain thermoreflectance experiments and modern electronics such as the heat assisted magnetic recording (HAMR) devices [3–5, 188]. A single laser pulse is implemented at the beginning of the simulation with a pulse width of 50 fs, where the laser power is tuned to 100 times larger than the constant irradiation case. Results of the simulations are shown in the next section.

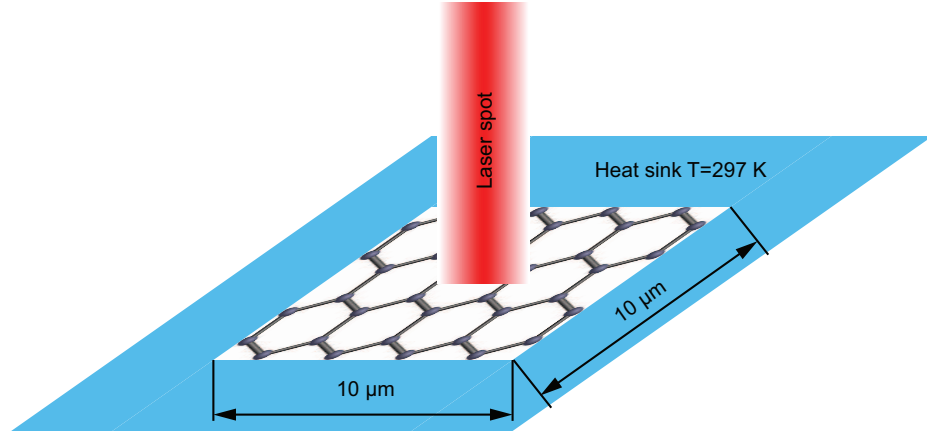


Figure 7.1. Illustration of the Raman experiment setup on SLG.

Table 7.1.
Thermal Properties of SLG at 297 K

Thermal Property	LA	TA	ZA	LO	TO	ZO
$G_{ep}(10^{16} \text{ W/m}^3\text{K})$	0.01	0.0001	0	0.06	0.27	0
$G_{pp}(10^{16} \text{ W/m}^3\text{K})$	0.27	1.30	0.19	0.27	0.14	0.04
$C_p(10^6 \text{ J/m}^3\text{K})$	0.19	0.32	0.61	0.03	0.02	0.16
$\tau(\text{ps})$	70.8	24.7	317	10	12	388
$k(\text{W/mK})$	863.0	237.9	2780.0	10.0	10.0	20.9

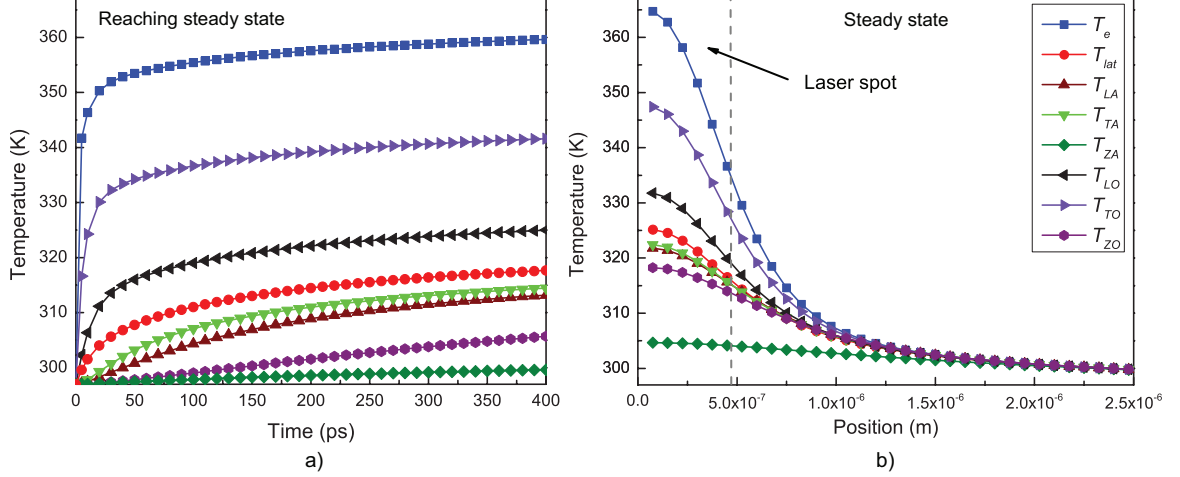


Figure 7.2. Temperature profiles of the SLG under constant laser irradiation in MTM: a) The transient temperature profile in the center of the SLG in the first 400 ps after the laser is on and b) the steady-state temperature profile of SLG along the line from the center to the mid-point of one boundary.

7.3.2 Results: transient and steady-state temperature profile

Case A: constant laser heating

The temperature profile of the center of the SLG for the first 400 ps after the laser is on is shown in Fig. 7.2 a). Initially the LO and TO phonons have quicker response to the heating from electrons, while the other phonon branches receive energy much more slowly due to their weak coupling to electrons. The steady-state temperature profile in MTM on SLG, as is shown in Fig. 7.2 b), is consistent with that reported in our previous work as expected [7]. In MTM, electrons can reach a temperature of 365 K while the temperature of the scattering lattice reservoir is around 325 K. Electrons and different phonon branches are in significant non-equilibrium. The largest temperature rise on TO phonons is 50 K which is more than 6 times larger than the smallest temperature rise of 8 K on ZA phonons, and the cooling radius, which is defined as the distance from the center of the SLG to the position where electrons and phonons reach

equilibrium, is $1.5 \mu\text{m}$ or 3 times the radius of the laser spot. As expected from the thermal properties in Table 7.1, the LO and TO phonons have higher temperatures. This is because their large G_{ep} 's make them gain energy from electrons efficiently in the center, and their low k also prevents heat from dissipating fast to the boundaries. The ZA branch, on the other hand, is an opposite to these two branches. It cannot receive energy from electrons directly and only gets heated by the scattering lattice reservoir with a weak coupling factor, and its exceptionally high k helps heat dissipate fast to the boundaries, resulting in a relatively flat temperature profile which stays near the boundary temperature. The LA, TA and ZO phonons stay in between due to their intermediate thermal properties. It is noteworthy that T_{lat} here is the temperature of the scattering lattice reservoir, which is averaged by G_{pp} over all six phonon branches and does not necessarily represent the apparent lattice temperature that can be observed in experiment. A more detailed discussion will be presented in the later section.

Case B: pulse laser heating

The transient temperature profile of the center of the SLG is shown in Fig. 7.3 a). During the first 50 fs of the simulation, electrons are heated to a maximum temperature of about 778 K, and start to cool sharply after the laser pulse diminishes. The LO and TO phonons undergo similar processes. The other phonon branches, however, still get heated up for a while, as is more clearly shown in Fig. 7.3 b). Interestingly, electrons become cooler than the TO phonons soon after the laser pulse diminishes. This is because k_e is much higher than k_{LO} while C_e is much smaller than C_{LO} , or the ratio of k/C is much larger for electrons. As a result, electrons dissipate heat faster which leads to an even larger temperature drop, and their temperature profile crosses that of the TO phonons. Similar processes also happen for LA, TA, LO and ZO phonons, with an exception for the ZA phonons which have exceptional high thermal conductivity but have no coupling with the electrons. The energy received by

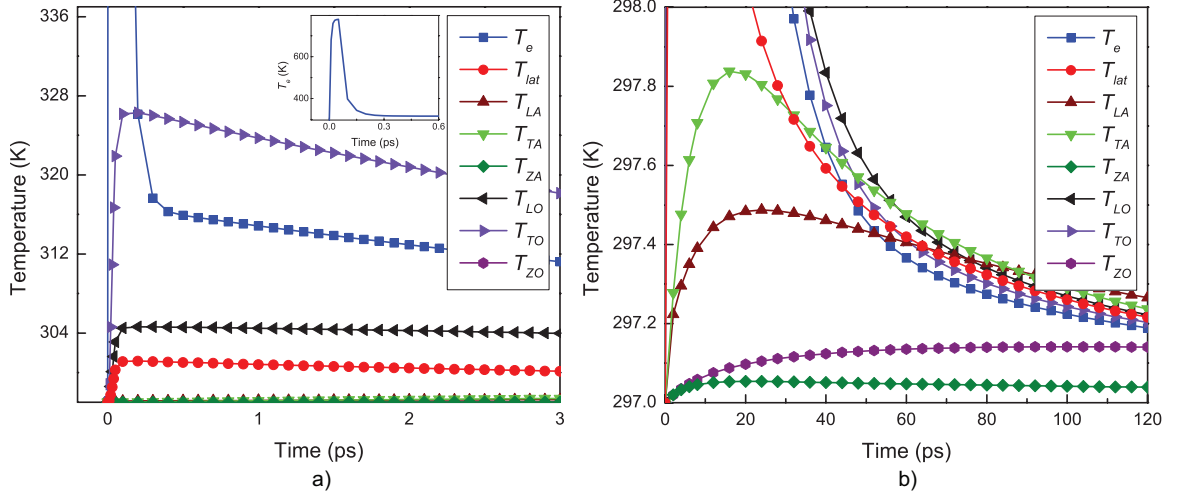


Figure 7.3. The transient temperature profiles in the center of the SLG under pulse laser heating in MTM.

ZA phonons from other phonons is dissipated fast to the boundaries and they always stay as the branch with the lowest temperature. Although the temperature difference between different phonon branches and the electrons is smaller than 0.4 K after 120 ps, they are still not in complete equilibrium.

7.4 Discussions

7.4.1 The apparent lattice temperature and degree of non-equilibrium

In the previous section, we have used the scattering lattice reservoir temperature T_{lat} to represent the average phonon temperature. However, questions arise as to whether T_{lat} is the apparent lattice temperature T_p that can be probed in experiments. We argue that the apparent lattice temperature T_p should represent the overall internal energy of the lattice, hence it should be defined as:

$$T_p = \frac{\sum C_{p,i} T_{p,i}}{\sum C_{p,i}}. \quad (7.2)$$

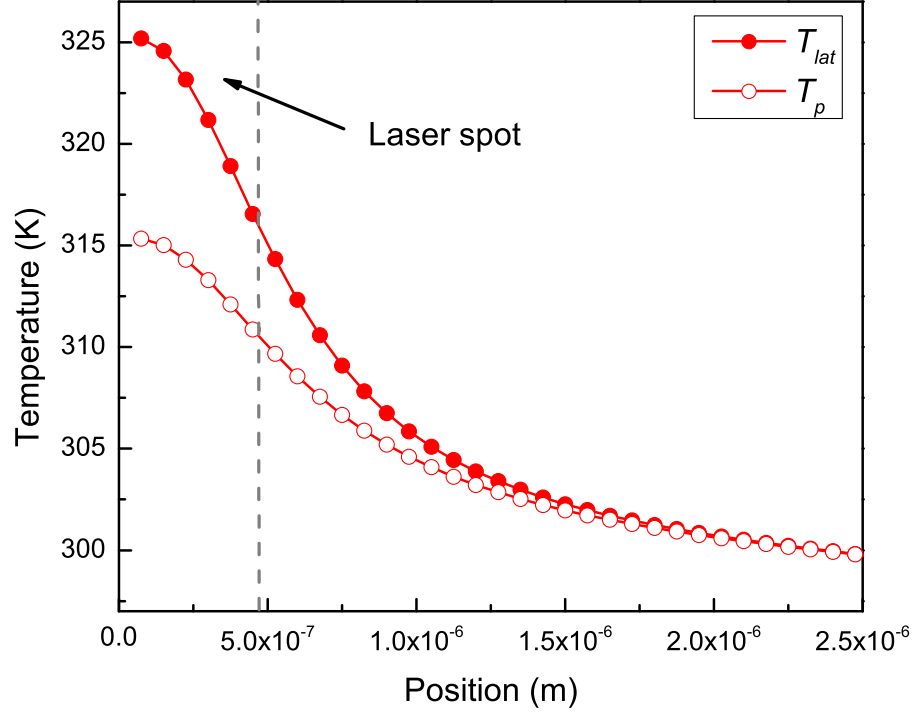


Figure 7.4. The comparison between the apparent lattice temperature T_p and the scattering lattice reservoir temperature T_{lat} .

A plot of the apparent lattice temperature T_p and scattering lattice reservoir temperature T_{lat} is shown in Fig. 7.4. We can see their deviation is significant inside the laser spot and gradually diminishes as the location approaches the boundaries. This can be explained by the degree of non-equilibrium between different phonon branches. From Eqs. (1.14) & (7.2) we can see that T_p is more dominated by the acoustic phonons, especially the ZA phonons due to its large heat capacity, while T_{lat} is more dependent on the branches with higher p-p coupling factor G_{pp} , e.g. the TA phonons. When the phonon branches have great non-equilibrium among each other, e.g. inside the laser spot, the two temperatures deviate from each other. They quickly converge outside the laser spot where the phonon non-equilibrium decreases. Then we plot the normalized deviation of all the 6 phonon branches, which is defined by:

$$\delta = \frac{T_{p,i} - T_p}{T_p - T_0}, \quad (7.3)$$

where T_0 is the boundary temperature of 297 K. The plot is shown in Fig. 7.5. The LO, TO and ZA phonons have the largest deviations, and this is primarily due to their largest and smallest e-p coupling strength respectively as discussed in the previous section. Here we want to propose a simple approximation to estimate their degree of non-equilibrium. As is discussed previously, a stronger e-p coupling strength will make the phonon temperature closer to the electron's, while a larger thermal conductivity will make its temperature profile flatter. For those branches with a higher temperature than T_p , a larger G_{ep} and smaller k will drag its temperature closer to T_e thus contributing to its deviation from T_p . Therefore a term G_{ep}/k can be used to determine its degree of non-equilibrium, the larger this value is, the more non-equilibrium there will be. Similarly, for those that have lower temperatures than the lattice, the previous term's inverse k/G_{ep} can be used. The larger this value is, the more deviation there will be. We tabulate the values of these two terms for each phonon branch of SLG in Table 7.2. It should be noted that a zero value does not necessarily mean the absence of non-equilibrium. The G_{pp} term, on the other hand, will always try to reduce the non-equilibrium.

From the results above we can gain some insights on how to quickly estimate the degrees of non-equilibrium and assess their significance. For example during the Raman experiment on SLG, before start one can use the thermal properties of SLG to estimate the degree of non-equilibrium of each phonon branch. The analysis above can provide insights on how accurate the measurement is. Further study can also be oriented since our MTM is not limited only to graphene, but can be extended to other materials of higher dimension as well. By performing similar calculations and analysis on other materials, it is also possible to build up a relationship between the G_{ep}/k term and the measured k 's error, which can then be used as a simple way to assess experiment accuracy.

Table 7.2.
Ratio of G_{ep}/k and k/G_{ep} of SLG at 297 K

Thermal Property	LA	TA	ZA	LO	TO	ZO
G_{ep}/k	0.001	0.0001	-	0.56	2.6	0
k/G_{ep}	-	-	∞	-	-	-

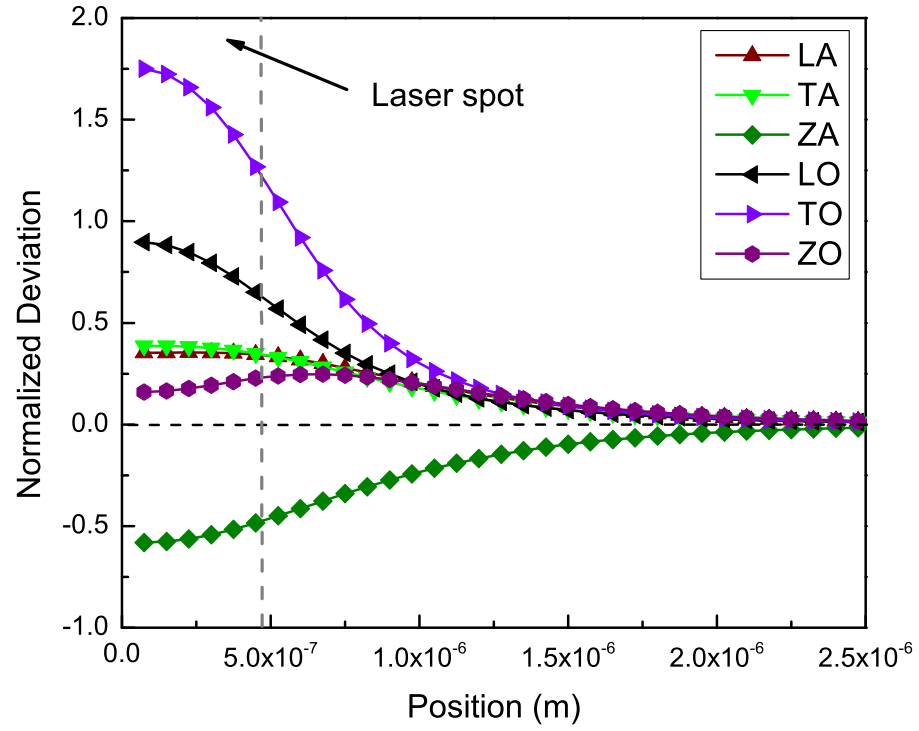


Figure 7.5. The normalized deviation of all 6 phonon branches in SLG.

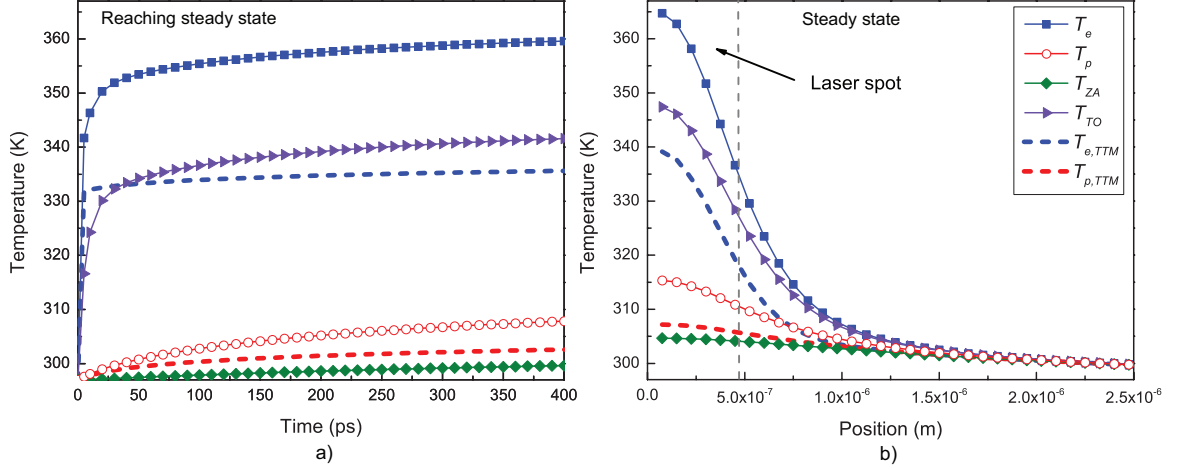


Figure 7.6. Temperature profiles of the SLG under constant laser irradiation in TTM: a) The transient temperature profile in the center of the SLG in the first 400 ps after the laser is on and b) the steady-state temperature profile of SLG along the line from the center to the mid-point of one boundary. Four representative temperatures from MTM are also included for reference.

7.4.2 A comparison with the original two-temperature model

Now with the apparent lattice temperature defined, we present a comparison between our MTM and the conventional TTM. The TTM calculation is conducted on the same system with the same initial and boundary conditions. The thermal properties of the SLG, i.e. k , C and G_{ep} are acquired simply by summing up the values used in MTM over all the phonon branches. The heating-up and steady-state TTM temperature profiles of the system are shown in Fig. 7.6 along with some representative temperatures from MTM. It can be seen from the figure that MTM and TTM have completely different results. In TTM, the steady-state electron temperature in the center is 340 K while that of phonons is 308 K. The two temperatures quickly get into equilibrium with a cooling radius of approximately $1\mu\text{m}$, or two times the radius of the laser spot. The electron and apparent lattice temperature in MTM are higher than those in TTM by 50% and 80%, respectively. In addition, in MTM the

temperatures of certain phonon branches are significantly higher than the apparent lattice temperature. Interestingly, the TO phonons' temperature in MTM is even higher than the electron temperature in TTM. Due to their strong e-p coupling, the TO phonons get heated up quickly to a high temperature in MTM. This becomes the so-called “hot phonon bottleneck”, which in return prevents electron from cooling and results in a higher electron temperature. Another interesting finding is that the lattice temperature in TTM is very close to the ZA phonons in MTM. This is because in TTM, all the phonon branches collapse into one single phonon branch with the combined G_{ep} and k . As a result the lattice quickly dissipates heat to the boundaries with its large k and stays at a low temperature close to the boundary. The electron temperature is also dragged down which is even cooler than the TO phonons in MTM. As expected, in TTM the system converges faster to steady state due to the absence of the hot phonon bottleneck.

The large difference between MTM and TTM has important and wide range of implications for processes involving laser-matter interactions. We can regard the MTM temperatures as the “real” temperatures in the experiment. Therefore, in order to increase the temperatures in TTM to match those in MTM, one has to use a smaller k in TTM. Based on the Fourier's Law of conduction $k \nabla^2 T + S_{laser} = 0$, the fitted apparent k will be around 1700 W/mK, less than 60% of the value used in the simulation. Therefore it is necessary to use MTM instead of TTM for an accurate prediction. In other words, the laser heating leads to an apparent thermal conductivity lower than the intrinsic value due to the local thermal non-equilibrium. It also has important implications to thermal management of electronic devices. Our MTM shows that certain phonon temperatures can be much higher than the apparent lattice temperature. These hot phonons can displace the lattice along their eigenvectors and result in “non-thermal damage” of the device even though the apparent temperature is still lower than the damage threshold [25, 32]. Therefore, MTM is advantageous over TTM for thermal design to better prevent such non-thermal device failures.

We also perform the pulse laser heating simulation using TTM. The transient temperature profile is shown in Fig. 7.7. Different from the constant irradiation case, the maximum temperatures of electrons and phonons are almost identical in both models. $T_{e,TTM}$ has a maximum value of 775 K at 50 fs. The temperature profiles of T_p and $T_{p,TTM}$ differ by about 30%, but the absolute value is trivial because the lattice heat capacity is much larger than its electronic counterpart and the temperature rise is small. This indicates that using a simple TTM will not affect the prediction of the lattice temperature too much. However, the hot electron relaxation processes are completely different as is more clearly shown in Fig. 7.7 b). In TTM, $T_{e,TTM}$ drops to below 298 K within 0.5 ps, while this only happens to $T_{e,MTM}$ after more than 30 ps due to the hot optical phonons. Therefore TTM over-predicts the electron relaxation rate by more than 60 times. Slow electron relaxation is beneficial for solar cells where electron cooling should be minimized for efficiency enhancement [189, 190], hence our MTM will be a much more accurate design tool than TTM.

7.5 Conclusions

We have developed a multi-temperature simulation approach which can present phonon branch-resolved temperature profile and capture the non-equilibrium thermal transport process. Using temperature-dependent and phonon branch-resolved thermal properties as inputs, we obtained the transient and steady-state temperature profiles of the thermal transport in laser irradiated SLG. Results show that the phonon branches are in strong non-equilibrium due to their different e-p coupling strength. The largest temperature rise occurred for the TO phonons is more than 6 times larger than the smallest of the ZA phonons. The thermal transport is dominated by different material properties during constant and pulse laser heating processes. Then we discuss and define the apparent lattice temperature in MTM and make a comparative study with the original TTM. It is found that TTM predicts a temperature profile significantly lower than MTM, and a simple assumption that

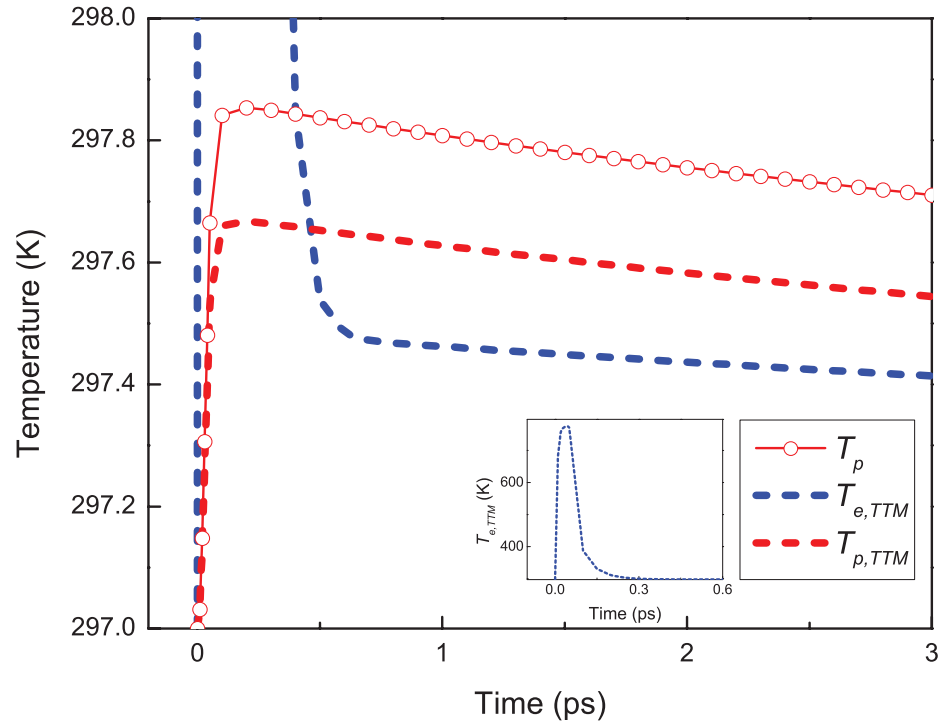


Figure 7.7. The transient temperature profiles in the center of the SLG under pulse laser heating in TTM. Figure b)'s horizontal axis is on logarithmic scale, which shows the electron relaxation in two models.

ignores the thermal non-equilibrium between phonons can under-predict the thermal conductivity by more than 40%, while over-predicting the hot electron relaxation rate by more than 60 times. We also find that the term G_{ep}/k can be used to estimate the degree of non-equilibrium of phonon branches during a steady-state conduction. We anticipate that our model and results will be useful for experimentalists and engineers in prediction and interpretation of a wide range of processes involving laser-matter interactions. Our model can also be extended to apply to other materials of higher dimensions and eventually become a generalized methodology.

8. MULTI-TEMPERATURE MODEL SIMULATION OF NON-EQUILIBRIUM THERMAL TRANSPORT AT INTERFACES

8.1 Introduction

Nowadays as electronic devices shrink into nano-scale, interfacial heat generation and dissipation become critical issues in designing these nano-structures. Traditional prediction methods for the lattice portion of interfacial thermal conductance (ITC) include calculations based on acoustic mismatch model (AMM), diffuse mismatch model (DMM), atomistic Green's function, molecular dynamics (MD) and density functional theory (DFT), etc [15, 22, 123, 167]. Among them DMM is often used to provide reference for experimental measurements due to its practical simplicity and its advantage in describing the interface between dissimilar materials. The lattice ITC is then calculated using the Landauer approach as follows:

$$h_{pp} = \int_0^\infty D(\omega)t(\omega)v_g\hbar\omega\frac{dn}{dT}d\omega. \quad (8.1)$$

Here ω is the phonon frequency, D is the density of states, t is the transmission, n is the Bose-Einstein distribution function and T is temperature. In Eq. (8.1), two important assumptions are made: 1) elastic phonon scattering and 2) local thermal equilibrium. However, experimental measurements of ITC at several metal-diamond interfaces exceed the upper limits of DMM predictions by 20% to as large as 10 times [10–12], which challenges the validity of the aforementioned two assumptions. While the possible cross-interface electron-phonon (e-p) coupling and inelastic phonon scattering hypotheses have been investigated [13–15, 18, 137, 138], little effort has been delivered to the impact of phonon thermal non-equilibrium on ITC. It has been demonstrated that during many applications such as irradiation-matter interactions, phonons can be driven into strong non-equilibrium by mechanisms such as selective e-p coupling, and a simple equilibrium picture leads to misleading or wrong results. For example,

in Raman spectroscopy measurement of graphene's thermal conductivity, a simple two-temperature model (TTM) assuming local thermal equilibrium will under-predict the thermal conductivity by more than 50% [7, 8]. Strong phonon non-equilibrium has also been observed at graphene-graphene interfaces in MD simulations [61, 75]. Similarly, the e-p non-equilibrium at metal-dielectric interfaces has been proved to significantly affect the ITC [24, 31, 59]. These facts give rise to the question as whether phonon thermal non-equilibrium can also affect the lattice ITC significantly, therefore a method that can capture this non-equilibrium feature and predict its significance is necessary.

In this study, we will present a multi-temperature model (MTM) simulation approach which can capture the phonon non-equilibrium thermal transport process in dielectrics and across their interfaces. The phonon branch-resolved ITC's are calculated using AMM applied to each phonon branch. A case study of the thermal transport process at Si-Ge interfaces is presented to show the impact of non-equilibrium thermal transport on ITC.

8.2 Case study: thermal transport across Si-Ge interfaces

We perform calculation using our models on Si-Ge interfaces since both materials have six phonon branches and the thermal properties have been well predicted in previous literatures [72]. The input parameters are listed in Table 8.1 & 8.2. The phonon branch-resolved transmission coefficients at the interface are predicted using AMM. The transmission function of a single phonon mode with frequency ω for interface between 3D materials from AMM is shown in the following equation [22]:

$$t_{12,AMM}(\theta_1, \omega) = t_{21,AMM}(\theta_2, \omega) = \frac{4 \frac{Z_2}{Z_1} \frac{\cos \theta_2}{\cos \theta_1}}{\left(\frac{Z_2}{Z_1} + \frac{\cos \theta_2}{\cos \theta_1} \right)^2}, \quad (8.2)$$

where θ_1 is the angles of incidence, θ_2 is the angle of refraction, and Z is the acoustic impedance which equals the product of the material mass density ρ and the phonon

group velocity v_g . With the transmission coefficient from AMM, the heat flux J (unit: W/m²) and ITC h_{AMM} can be calculated from the Landauer approach:

$$J = \frac{1}{2} \int_0^{\frac{\pi}{2}} \int_0^{+\infty} \hbar \omega [D_1(\omega) v_{g1}(\omega) t_{12}(\theta_1, \omega) n(T_{e,1}) \sin \theta \cos \theta] d\omega d\theta - \frac{1}{2} \int_0^{\frac{\pi}{2}} \int_0^{+\infty} \hbar \omega [D_2(\omega) v_{g2}(\omega) t_{21}(\theta_2, \omega) n(T_{e,2}) \sin \theta \cos \theta] d\omega d\theta,$$

$$h_{AMM} = \frac{J}{\Delta T} = \frac{J}{(T_{e,1} - T_{e,2})}, \quad (8.3)$$

where $T_{e,1}$ and $T_{e,2}$ are the emitted phonon temperatures [133]. Our calculation assumes the interfacial transmission does not change the phonons' vibration patterns, so Eqs. (8.2) & (8.3) are applied to each phonon branch. The results are listed in Table 8.3. Because the optical phonon branches have no frequency overlaps, their t 's are all 0.

The simulation domain consists of a 500 nm-long Si block in contact with a 500 nm-long Ge block, as is shown in Fig. 8.1. The two ends are fixed at 310 K and 290 K respectively and heat flows in the direction perpendicular to the interface. Initially the entire system is at 300 K and then the simulation runs for 50 ns to ensure steady state is reached. The steady-state temperature profile is shown in Fig 8.2. It can be seen that the degree of non-equilibrium is not very strong at such interfaces. Different phonon branches are in equilibrium in most parts of the Ge block. The cooling length, defined as the distance for the largest temperature deviation between phonon branches to reach 5% of its maximum value, is smaller than 50 nm in Ge. The non-equilibrium is stronger in Si with a cooling length of approximately 200 nm, but the temperature deviation is trivial compared to the temperature jump across the interface. Several general trends can be observed from the results. The optical phonon branches have almost identical temperatures with T_{lat} due to their large G_{pp} values, while the non-equilibrium is stronger among acoustic branches. The TA phonons have a higher temperature than T_{lat} and dump energy to the lattice reservoir, while the LA phonons have a lower temperature and receive energy.

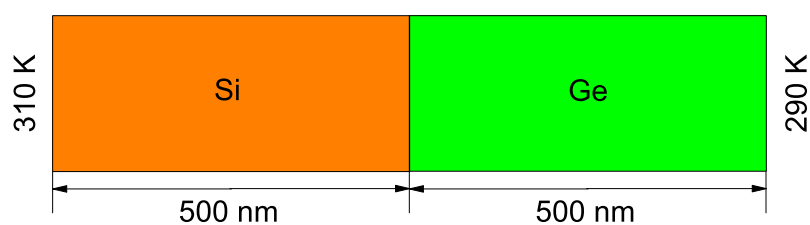


Figure 8.1. Illustration of the simulation domain consisting of a 500 nm-Si block and a 500 nm-Ge block.

Table 8.1.
Thermal Properties of Si at 297 K

Thermal Prop-erty	LA	TA	LO	TO
$G_{pp}(10^{16} \text{ W/m}^3\text{K})$	0.8	0.2	3.7	4.1
$C_p(10^5 \text{ J/m}^3\text{K})$	1.8	2.0	1.4	1.2
$\tau(\text{ps})$	21.7	136.4	3.8	3.0
$k(\text{W/mK})$	53.6	49.1	2.5	0.1

The total ITC across the interface is calculated by extrapolating the linear equilibrium section of the temperature profile to the interface to obtain the averaged temperature jump ΔT_{fit} , as is shown in Fig. 8.3. The result of $h_{MTM} = J / \Delta T_{fit}$ is 375.1 MW/m²K. Compared with the classical ITC based on local thermal equilibrium assumption, which is acquired by summing up the branch-resolved AMM results $h_{LA} + 2h_{TA} = 396.6 \text{ MW/m}^2\text{K}$ as can be easily verified using Eqs. (8.2) & (8.3), h_{MTM} is 5.4% smaller. This can be explained by the non-equilibrium in phonon temperatures. In both materials, acoustic phonons are the major heat carriers while the optical phonon contribution is trivial. When we use T_{fit} to calculate the ITC, J_{LA} is under-predicted since the gradient of T_{fit} is smaller than that of T_{LA} , while ΔT_{LA} is over-predicted, resulting in an under-prediction of LA phonons' contribution to the total ITC. The TA phonons, on the other hand, can be straightforwardly verified to be over-predicted on their contribution to the h_{MTM} . The competing effect between TA and LA eventually results in a smaller h_{MTM} than $h_{LA} + 2h_{TA}$. It is noteworthy that if all phonons are in thermal equilibrium, h_{MTM} should be identical to $h_{LA} + 2h_{TA}$, as can be verified from Eqs. (8.2) - (8.3). Therefore it is reasonable to conclude that this discrepancy originates from the non-equilibrium phonon thermal transport at the interface, and it is similar to the e-p non-equilibrium which occurs at metal-dielectric interfaces which also introduces additional interfacial thermal resistance.

Table 8.2.
Thermal Properties of Ge at 297 K

Thermal Prop- erty	LA	TA	LO	TO
$G_{pp}(10^{16} \text{ W/m}^3\text{K})$	0.5	0.1	3.1	3.6
$C_p(10^5 \text{ J/m}^3\text{K})$	1.6	1.6	1.5	1.4
$\tau(\text{ps})$	30.1	188.4	4.8	4.0
$k(\text{W/mK})$	20.2	7.1	1.1	0.1

Table 8.3.
ITC from AMM calculations

Phonon branch	h_{AMM}
LA	243.8 W/m ² K
TA	76.4 W/m ² K
LA & TO	0

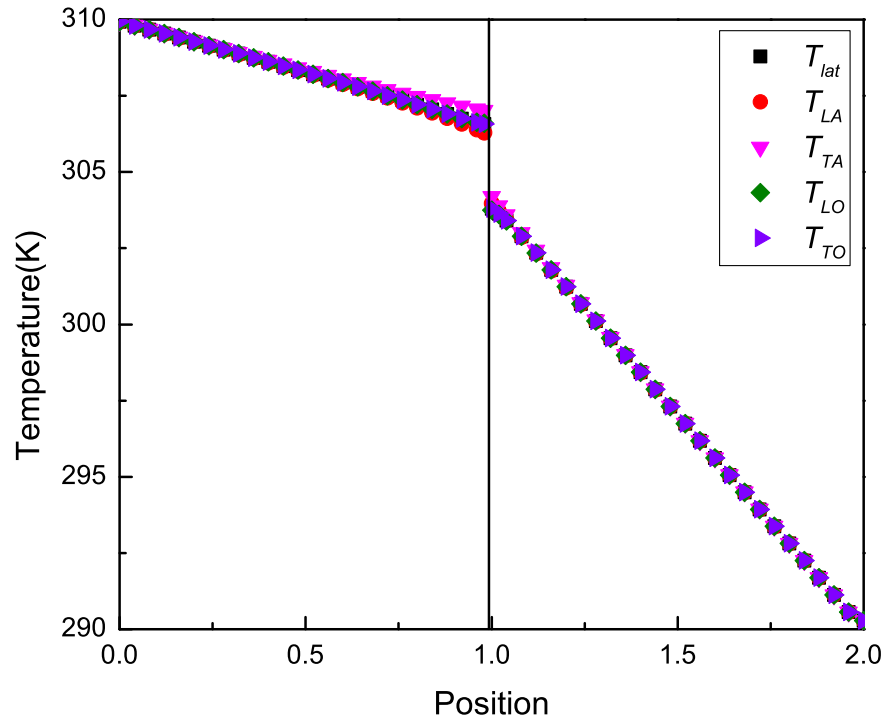


Figure 8.2. The steady-state temperature profile of a Si-Ge interface. The degree of non-equilibrium induced by p-p coupling is not very strong, with all phonon branches in thermal equilibrium in most parts of the system.

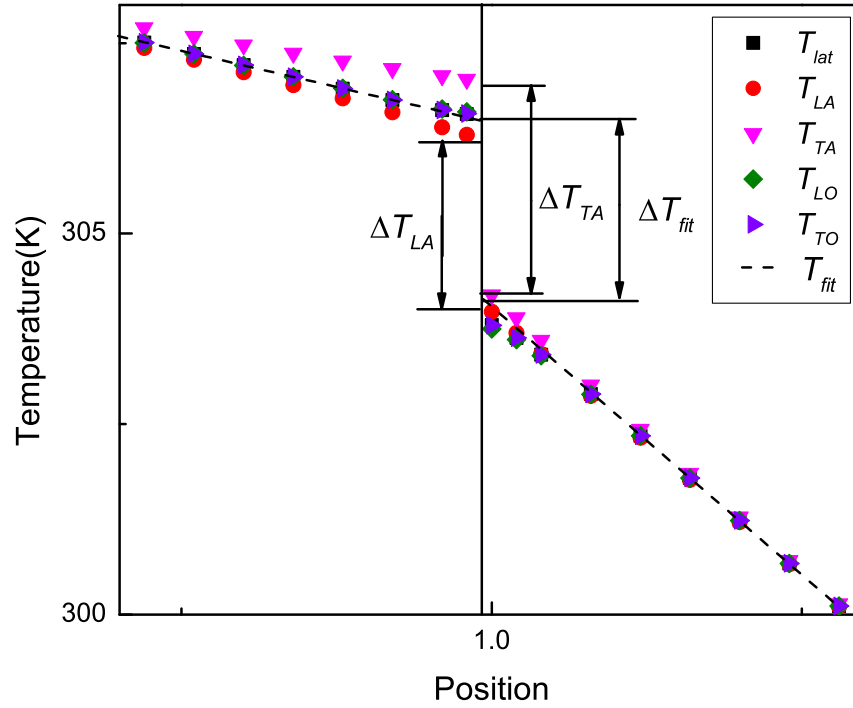


Figure 8.3. A zoomed-in picture of the temperature profile of the Si-Ge interface. The fitted temperature T_{fit} is acquired by extrapolating the linear equilibrium part of the temperature profile. It can be observed that $\Delta T_{LA} < \Delta T_{fit}$ and $\Delta T_{TA} > \Delta T_{fit}$

8.3 Conclusions

We have presented a multi-temperature simulation approach which can predict phonon branch-resolved temperature profile and capture the non-equilibrium thermal transport process in dielectrics and across interfaces. A case study of thermal transport across Si-Ge interfaces is presented using our MTM. Non-equilibrium between different phonon branches is observed due to their different transmission coefficients at the interface. Results show that the ITC from the simulation is 5.4% smaller than the classical prediction based on local thermal equilibrium assumption, and the discrepancy originates from the phonon thermal non-equilibrium near the interface. The impact of non-equilibrium phonon thermal transport on ITC is not very significant at Si-Ge interfaces and therefore may not readily answer the unresolved questions. Still our MTM is a general approach and can be applied to materials where non-equilibrium is stronger than Si-Ge and better manifest its impact.

9. SUMMARY

9.1 Conclusions

9.1.1 Investigation of non-equilibrium thermal transport in metal thin films based on two-temperature model

In this study we investigate the non-equilibrium thermal transport in a thin metal film embedded in dielectric matrix by deriving a general solution to the two-temperature model (TTM) equation, as well as performing Fourier and Boltzmann transport equation (BTE) simulations to benchmark our model. In the first stages we have studied the bulk thermal conductivity of Au and SAM (self-assembly-monolayer) as well as the interfacial thermal conductance (ITC) at their interfaces. Conventional non-equilibrium molecular dynamics (NEMD) simulation is conducted at a Au-SAM-AU-SAM-Au system at 100 K. Results show that h_{Bd} is 292.28 ± 17.71 MW/m²K, which agrees well with values reported by other literatures. Then a TTM-MD is conducted at room temperature on the same system. Results show that h_{Bd} rises to 349.3 ± 40.3 MW/m²K, which is expected because at higher temperature more phonons become available for interfacial thermal transport. In TTM an additional thermal boundary resistance (TBR) is introduced due to electron-phonon (e-p) non-equilibrium. The thermal conductivity of Au and SAM molecule chain is also calibrated, with $k_{p,Au} = 6.37$ W/mK and $k_{p,SAM} = 1.48$ W/mK. These results are used in the later Fourier and BTE studies of thermal transport in metal thin films embedded in polymer matrix.

Then we study the thermal transport in the system where a Au thin film is embedded in SAM matrix. At first, a classical TTM-Fourier calculation is performed. A general analytic solution to the TTM equations without film thickness approximations is derived, and it is used to get the temperature profile in the system. The

“critical thickness”, above which the particle size must reach in order to enhance the thermal conductivity of the composite material, is introduced and calculated using the general solution as well. Results show that for a Au film embedded in SAM matrix, the critical thickness is 10.8 nm.

Then a gray lattice Boltzmann method (LBM) combined with TTM is applied to simulate the same system, while the input parameters are set to be consistent with previous calculations. The results are generally the same with the TTM-Fourier calculation with the critical thickness being 10.6 nm, indicating the two approaches are identical under such conditions. It is confirmed that although BTE captures the “additional” temperature jump at material boundaries adjacent to thermal reservoirs, there is no such additional TBR at interfaces between non-reservoir materials. Several factors that can affect this critical thickness are also investigated. It is found that G_{ep} , R_{Bd} , k_{poly} and $k_{p,metal}$ can all affect L_c significantly, while $k_{e,metal}$ plays a relatively trivial role at such thickness.

Finally the thermal transport in metal thin films adjacent to dielectric substrates is investigated as a general issue. It is found that in metal films with the thickness of only several nanometers, the electrons hardly contribute to the thermal transport. A general expression for the effective thermal conductivity is derived. A quantitative analysis is made based on the solution. Results show that when the film thickness is very small, i. e. the thin limit, k_{eff} converges to k_p , while it converges to $k_p + k_e$ at the opposite extreme “thick limit”. A physical explanation of this phenomenon is that in such metal films, e-p non-equilibrium exists at the two boundaries, which significantly negates the electron thermal transport efficiency regardless of its high intrinsic thermal conductivity.

The fact that our classical TTM-Fourier method and semi-classical TTM-LBM method are identical at such metal-dielectric interfaces makes it possible to simplify simulation tools. And our results of the critical thickness as well as the analysis on thermal transport in metal thin films can prove useful for researchers in designing

experiments and interpreting experiment results. Still a simulation tool of higher dimensions which can cope with more sophisticated cases is desired.

9.1.2 Two-temperature molecular dynamics simulation of metal-dielectric interfaces with non-local electron-phonon coupling

In this study we focus on understanding and developing a preliminary model for non-local e-p coupling along with a corresponding simulation tool which includes such physics. Two models are proposed to incorporate this physics in the simulation. In the phonon-wavelength model, based on the conventional TTM equations, non-local e-p coupling is incorporated by modifying the coupling terms. In the metal, electrons can couple to phonons in a range of 2 phonon-wavelength λ_{avg} rather than only those at the same location. The coupling term in the equation is modified to an integral form accordingly. At the interface, new boundary conditions are added to enable the cross-interface e-p coupling. Similar to the non-local e-p coupling inside metal, electrons can couple to atoms with a distance of 1 phonon-wavelength of the dielectric material in the dielectric substrate. In the “joint-modes” model, based on the “joint-phonon-modes” physics, a joint-mode region is defined at the interface which contains atoms from both sides, and electrons in this region can evenly couple to all the atoms in the same region.

Then we modify our previous TTM-MD approach to include this new mechanism. A group of atoms in the dielectric near the interface is designated as the ones in the dielectric part of the joint-modes region. Based on the Langevin equation, an extra friction force is added to this group of atoms to account for the cross-interface e-p coupling, and the energy is transferred to/from the metal surface electrons to ensure energy conservation. These modifications successfully implemented the non-local e-p coupling in the TTM-MD code. The simulation is then conducted on Cu-Si interfaces in comparison to our previous study on the same system. With all the inputs in common set to the same, and the cross-interface coupling factor G_{ei} set to

be the same with G_{ep} in metal, results show that the additional energy channel at the interface can reduce the TBR by 18%. Results of the two parallel simulations of our two models, with the difference of whether e-p coupling is non-local inside metal, show that non-local EPC does not affect the thermal transport in bulk materials significantly.

Finally a thermal circuit analysis is made based on our model and the model provided in the previous Huberman and Overhauser's work. We construct a mixed series-parallel thermal circuit, where the e-p non-equilibrium resistance in the metal side of the joint-modes region is in series with the phonon-phonon (p-p) resistance, and they together are in parallel with the interfacial e-p coupling resistance in the dielectric side of the joint-modes region. We are able to get each value of the decomposed R_{Bd} components. As a comparison, the simple series circuit that neglects the cross-interface e-p coupling slightly over-estimates the interfacial resistance, while the simple parallel circuit under the Overhauser picture under-estimates the total interfacial resistance. Knowing electron and phonon temperature profiles and the corresponding thermal circuit is essential to understand metal-dielectric interfacial transport.

Rather than correctly describing the e-p coupling physics at such interface, we focus on interpreting the thermal circuit and developing a useful simulation tool. We expect that our results will be beneficial to researchers in understanding the thermal transport process, and that our tool can become more practical when the physics of cross-interface e-p coupling is clear.

9.1.3 Non-local electron-phonon coupling in pure metals manifested by size effect based on first-principles calculations

In our previous study with TTM-MD, we already proposed a preliminary non-local e-p coupling model which has very simple assumptions. Inspired by the aforementioned idea and driven by the necessity to predict accurate e-p coupling properties,

in this work the effort is put into proposing a more accurate model based on solid theoretical calculations. Starting with calculating the e-p coupling properties in bulk Cu, we are able to get results that are consistent with previous works, as well as the conclusion that electrons generally couple stronger to phonons with higher frequencies.

Then we move on to investigate the non-local e-p coupling phenomenon in pure metals based on first-principles methods. To demonstrate the effect, we first perform calculations on Al, Cu and Ag films of different sizes and find that G_{ep} is different in these cases, confirming that e-p coupling has size effect. In order to manifest the non-local coupling phenomenon while isolating other factors that can influence e-p coupling, we define a new term: normalized partial coupling strength $\alpha_{v,norm}^2$, which describes the coupling strength between electrons and individual phonon branches while normalized by their density of states (DOS) and dispersion. By comparing the $\alpha_{v,norm}^2$ of bulk and thin film metal, we are able to calculate the “reduction factor” of the coupling strength, from which we construct a Gaussian-distribution function based coupling strength distribution function (CSDF). Results show that electrons in Al can couple to atoms in a range of up to 2 lattice-constants, or 0.83 nm. The coupling strength between electrons and phonons in adjacent atomic layers still preserves more than 75% of that between electrons and phonons in the same atomic layer.

Comparative studies are performed on Cu and Ag. Results show that the non-local e-p coupling is not as significant as in Al, but the effective ranges are still more than 2 lattice-constants with 0.37 nm for Cu and 0.49 nm for Ag, and coupling strength in the adjacent atomic layers is approximately 40% of that in the center. Cu and Ag also exhibit similar non-local e-p coupling properties. Considering the fact that they are elements in the same group, we propose that non-local e-p coupling is similar in materials that has similar electronic structure while regardless of the atomic masses.

Our work is the first to present a theoretical calculation to investigate the non-local e-p coupling effect. Our results already contain promising information, as the distance between the surface atomic layers at a metal-dielectric interface is similar with that

between adjacent atomic layers inside metal. This indicates that cross-interface e-p coupling can be quite significant according to the results of our calculations, which gives us confidence in carrying on our calculation into a real metal-dielectric interface. In fact a calculation based on our model suggests that the ITC due to cross-interface coupling is on the order of $100 \text{ MW/m}^2\text{K}$, which is quite significant compared with typical metal-dielectric ITC's of $200\text{-}700 \text{ MW/m}^2\text{K}$. The material tested, Al, is a very common metal with low cost. Although the real application is still limited by other mechanical properties such as hardness, our results can still be useful in providing people with guidance when choosing materials. It is possible that certain Al alloys also has similar non-local e-p coupling properties and other features that are more applicable. Besides, our results also have many implications in a wide range of applications where e-p coupling is important, such as hot electron relaxation through phonons in core-shell quantum dots and solar cells.

9.1.4 Multi-temperature model simulation of non-equilibrium phonon transport in metals and across interfaces

In this work, we go beyond TTM to study the phonon thermal non-equilibrium transport which has been largely overlooked by previous studies. Based on TTM equations, a multi-temperature model (MTM) is developed with phonon branch-resolved e-p coupling strength. An averaged scattering lattice reservoir is defined that couples with each phonon branch, which represents the phonon-phonon scattering mechanism. With proper inputs of their material properties such as e-p coupling factor G_{ep} , thermal conductivity k and heat capacity C , our MTM is able to simulate thermal transport processes in materials and present branch-resolved temperature profiles.

A case study of the transient and steady-state thermal transport in laser irradiated single-layer graphene (SLG) is presented. Results show that phonons are in strong non-equilibrium driven by selective e-p coupling. In SLG under constant laser

irradiation, the the largest steady-state temperature rise of phonons is 6 times larger than the smallest one. Compared with TTM, MTM predicts 80% higher electron temperature and 50% higher phonon temperature. The higher overall temperature is primarily induced by the “hot phonon bottleneck” where optical phonons have much larger temperature than the acoustic phonons and effectively prevent electrons from cooling. The constant laser irradiation case represents the heat transfer process during a Raman spectroscopy experiment. If a TTM analysis is applied to the observed lattice temperature under non-equilibrium, the measure the thermal conductivity will be under-estimated by approximately 40%. In another case featuring a pulse laser heating process on SLG, which is common in time-domain-thermoreflectance (TDTR) experiments and modern electronics such as heat assisted-magnetic recording devices, MTM increases the hot electron relaxation time by 60 times. Our results demonstrate the significance of phonon thermal non-equilibrium, and justifies the necessity to use the sophisticated but simple MTM for an accurate prediction of experimental results and device performance.

Our MTM is also applied to investigate the effect of thermal non-equilibrium on ITC at dielectric interfaces. Si-Ge interfaces are chosen as the case study. In addition to the aforementioned needed inputs, the individual ITC for each phonon branch is calculated using branch-resolved acoustic mismatch model (AMM) based on the phonon dispersions. Results show phonons are in non-equilibrium near the interface due to the selective p-p coupling conductance, and the thermal non-equilibrium causes the ITC predicted from the simulation to be smaller than the summation of the branch-wise AMM ITC’s. The observation is consistent with what have been demonstrated at metal-dielectric interfaces, where e-p non-equilibrium introduces an additional TBR and reduces the ITC. For Si-Ge ITC this reduction is 5.4%, which is not significant due to the strong p-p coupling in both materials which leads to an insignificant thermal non-equilibrium. However, we expect the effect will be stronger in materials with strong phonon thermal non-equilibrium such as SLG.

Besides our results and findings, our MTM is a general simulation approach that can be applied to most materials. The phonon branch-resolved predictions will prove advantageous over the classical TTM, and gain use by experimentalists and engineers in predicting the thermal transport involving laser-matter interaction and hot electron relaxation, such as during Raman experiments, in modern electronics and nuclear reactors.

9.2 Future works

Non-equilibrium thermal transport, as it begins to draw researchers' attention, gives rise to a fundamental question: how to define the local temperature when the system is in thermal non-equilibrium? As is mentioned in Chapter 1 the definition of temperature is closely related to the distribution functions, and in non-equilibrium systems energy particles do not share a common distribution function. Regardless, in practice we still only observe one lattice temperature, and it is not clear how this "averaged" temperature is related to the temperatures of each phonon mode. Is it the scattering lattice reservoir temperature? Or can it be the one averaged by phonon heat capacities? In Raman experiments this measured temperature may be close to those of the phonons with intermediate frequencies, while in TDTR they may be more closely related to the optical phonons which are more sensitive to e-p coupling. Therefore It will be helpful to investigate how the observed temperature is related to the phonon modal temperatures, which will be helpful for experimentalist to interpret their results and for engineers to evaluate device performance.

Non-equilibrium thermal transport has a wide range of applications and fields to research into. The TTM-MD as a predictive method which can incorporate complicated lattice physics and electronic influence at the same time, can be applied to more occasions other than electronic devices. In nuclear reactors, materials sustain long time ion and electromagnetic wave irradiation, and e-p coupling plays an important role in the radiation damage production and evolution [43,44]. TTM-MD can be used

to predict this process as a practical tool, but it also meets the challenge when simulating high-energy irradiation as the electrons' temperature will become high which will likely make the simulation unstable [30,80]. Many temperature-dependent properties will also change significantly during this process and the current TTM-MD where electronic properties are temperature-independent values will need improvement. Our MTM as a sophisticated but simple tool, can also be applied in a wide variety of applications. As is mentioned in Chapter 8, the thermal non-equilibrium's effect on interfacial thermal transport is still not clear and deserves further investigation on materials that have strong phonon thermal non-equilibrium. Extension to higher dimensions which can describe thermal transport processes in real devices is also desired.

The current work finished on non-local e-p coupling is merely the starting stage for the investigation into the thermal transport at metal-dielectric interfaces. The next step is to apply the calculation to interfaces rather than pure metals, which is more practical to solve the long-time debate but also much more challenging. There are two issues we need to settle before we can start a practical calculation on a metal-dielectric interface: 1) excellent lattice mismatch so that the unit cell does not contain too many atoms which can make the calculation impossible and 2) reliable experimental results which can be used to benchmark our calculations. The material pairs that satisfy the second criteria can be easily found as there are numerous TDTR experiments on metal-diamond interfaces which provide consistent results. However, none of these pairs have acceptable lattice mismatch that can form a relatively small unit cell. For example, a Pb-diamond interface unit cell has to contain at least 200 atoms to reduce the cross-section lattice mismatch to within 1%, which makes the calculation nearly impossible. Currently the solution I propose for the future work is performing calculation on the Cu-diamond interfaces. The lattice mismatch for a face-centered cubic (FCC) Cu unit cell and a diamond unit cell is smaller than 1%, so it is possible to construct an interface with the unit cell number 1 to 1 of the two materials, which significantly decreases the number of atoms in the unit cell. On

the other hand, one practical approach which can also help understand the thermal transport at such interfaces in addition to investigating the non-local e-p coupling is developing an accurate interatomic potential for the material pair. As is mentioned above, MD simulation automatically includes all the complex phonon physics and is therefore an excellent tool for predicting the phonon thermal transport. If a fine potential can be applied, the ITC due to phonon coupling at metal-dielectric interfaces can be reasonably accurately predicted, and then by comparing it to experiments it is straightforward to see what is causing the ITC to be unexpectedly high and whether cross-interface e-p coupling is important.

REFERENCES

REFERENCES

- [1] Jeremy A Rowlette and Kenneth E Goodson. Fully coupled nonequilibrium electron-phonon transport in nanometer-scale silicon FETs. *IEEE Transactions on Electron Devices*, 55(1):220–232, 2008.
- [2] John Robertson. High dielectric constant gate oxides for metal oxide Si transistors. *Reports on Progress in Physics*, 69(2):327–396, 2005.
- [3] Liang Pan and David B. Bogy. Data storage: Heat-assisted magnetic recording. *Nature Photonics*, 3(4):189–190, 2009.
- [4] B. Xu, H. Wang, Z. Cen, Z. Liu, K. Ye, H. Yang, J. Zhang, and J. Li. Short pulse laser heating for hamr: Density potential and implementation issues. In *2015 IEEE Magnetics Conference (INTERMAG)*, May 2015.
- [5] Jhih-An Yang, Stephen Parham, Daniel Dessau, and Dmitry Reznik. Novel electron-phonon relaxation pathway in graphite revealed by time-resolved raman scattering and angle-resolved photoemission spectroscopy. *Nature Scientific Reports*, 7(40876), Jan 2017.
- [6] Lutz Waldecker, Roman Bertoni, Ralph Ernstorfer, and Jan Vorberger. Electron-phonon coupling and energy flow in a simple metal beyond the two-temperature approximation. *Phys. Rev. X*, 6:021003, Apr 2016.
- [7] Ajit K. Vallabhaneni, Dhruv Singh, Hua Bao, Jayathi Murthy, and Xiulin Ruan. Reliability of raman measurements of thermal conductivity of single-layer graphene due to selective electron-phonon coupling: A first-principles study. *Phys. Rev. B*, 93:125432, Mar 2016.
- [8] Sean Sullivan, Ajit Vallabhaneni, Iskandar Kholmanov, Xiulin Ruan, Jayathi Murthy, and Li Shi. Optical generation and detection of local nonequilibrium phonons in suspended graphene. *Nano Letters*, 17(3):2049–2056, 2017.
- [9] M. L. Huberman and A. W. Overhauser. Electronic kapitza conductance at a diamond-pb interface. *Phys. Rev. B*, 50:2865–2873, Aug 1994.
- [10] Gregory T Hohensee, R B Wilson, and David G Cahill. Thermal conductance of metal-diamond interfaces at high pressure. *Nature communications*, 6:6578, January 2015.
- [11] R. J. Stoner and H. J. Maris. Kapitza conductance and heat flow between solids at temperatures from 50 to 300 k. *Phys. Rev. B*, 48:16373–16387, Dec 1993.
- [12] Ho-Ki Lyeo and David G. Cahill. Thermal conductance of interfaces between highly dissimilar materials. *Physical Review B*, 73(14):144301, April 2006.

- [13] Patrick E. Hopkins. Multiple phonon processes contributing to inelastic scattering during thermal boundary conductance at solid interfaces. *Journal of Applied Physics*, 106(1):013528, 2009.
- [14] Ashutosh Giri, John T. Gaskins, Brian F. Donovan, Chester Szwejkowski, Ronald J. Warzoha, Mark a. Rodriguez, Jon Ihlefeld, and Patrick E. Hopkins. Mechanisms of nonequilibrium electron-phonon coupling and thermal conductance at interfaces. *Journal of Applied Physics*, 117(10):105105, 2015.
- [15] J. T. Gaskins, G. Kotsonis, A. Giri, C. T. Shelton, E. Sachet, Z. Cheng, B. M. Foley, Z. Liu, S. Ju, Junichiro, M. S. Goorsky, S. Graham, T. Luo, A. Henry, J.-P. Maria, and P. E. Hopkins. Thermal boundary conductance across epitaxial ZnO/GaN interfaces: Assessment of phonon gas models and atomistic Green's function approaches for predicting interfacial phonon transport. *ArXiv e-prints*, October 2017.
- [16] Patrick E. Hopkins, Jared L. Kassebaum, and Pamela M. Norris. Effects of electron scattering at metal-nonmetal interfaces on electron-phonon equilibration in gold films. *Journal of Applied Physics*, 105(2):023710, 2009.
- [17] Keng-Hua Lin and Alejandro Strachan. Role of direct electron-phonon coupling across metal-semiconductor interfaces in thermal transport via molecular dynamics. *The Journal of Chemical Physics*, 143(3):034703, 2015.
- [18] Zexi Lu, Yan Wang, and Xiulin Ruan. Metal/dielectric thermal interfacial transport considering cross-interface electron-phonon coupling: Theory, two-temperature molecular dynamics, and thermal circuit. *Physical Review B*, 93:064302, Feb 2016.
- [19] Tingyu Lu, Jun Zhou, Tsuneyoshi Nakayama, Ronggui Yang, and Baowen Li. Interfacial thermal conductance across metal-insulator/semiconductor interfaces due to surface states. *Phys. Rev. B*, 93:085433, Feb 2016.
- [20] Sridhar Sadasivam, Ning Ye, Joseph P. Feser, James Charles, Kai Miao, Tillmann Kubis, and Timothy S. Fisher. Thermal transport across metal silicide-silicon interfaces: First-principles calculations and green's function transport simulations. *Phys. Rev. B*, 95:085310, Feb 2017.
- [21] C. Kittel. *Introduction to Solid State Physics (Wiley, Hoboken, NJ, 2005)*. 2005.
- [22] E. T. Swartz and R. O. Pohl. Thermal boundary resistance. *Rev. Mod. Phys.*, 61:605–668, Jul 1989.
- [23] S V Lebedev and A I Savvatimski. Metals during rapid heating by dense currents. *Soviet Physics Uspekhi*, 27(10):749, 1984.
- [24] Yan Wang, Xiulin Ruan, and Ajit K. Roy. Two-temperature nonequilibrium molecular dynamics simulation of thermal transport across metal-nonmetal interfaces. *Phys. Rev. B*, 85:205311, May 2012.
- [25] Y. Wang and X. Xu. Molecular dynamics studies of ultrafast laser-induced nonthermal melting. *Applied Physics A*, 110(3):617–621, Mar 2013.

- [26] B. Y. Mueller and B. Rethfeld. Relaxation dynamics in laser-excited metals under nonequilibrium conditions. *Phys. Rev. B*, 87:035139, Jan 2013.
- [27] A. De Luca, J. Viti, D. Bernard, and B. Doyon. Nonequilibrium thermal transport in the quantum Ising chain. , 88(13):134301, October 2013.
- [28] Ye Yang, David P. Ostrowski, Ryan M. France, Kai Zhu, Jao van de Lagemaat, Joseph M. Luther, and Matthew C. Beard. Observation of a hot-phonon bottleneck in lead-iodide perovskites. *Nature Photonics*, 10:53–59, 2016.
- [29] J.-L. Domenech-Garret. Non equilibrium thermal and electrical transport coefficients for hot metals. *ArXiv e-prints*, January 2017.
- [30] Yanwen Zhang, Shijun Zhao, William J. Weber, Kai Nordlund, Fredric Granberg, and Flyura Djurabekova. Atomic-level heterogeneity and defect dynamics in concentrated solid-solution alloys. *Current Opinion in Solid State and Materials Science*, 21(5):221 – 237, 2017. Concentrated Solid Solution Alloys Perspective.
- [31] Arun Majumdar and Pramod Reddy. Role of electronphonon coupling in thermal conductance of metal/nonmetal interfaces. *Applied Physics Letters*, 84(23):4768–4770, 2004.
- [32] Tobias Zier, Eeuwe S. Zijlstra, Alan Kalitsov, Ioannis Theodonis, and Martin E. Garcia. Signatures of nonthermal melting. *Structural Dynamics*, 2(5):054101, 2015.
- [33] M.I. Kaganov, I.M. Lifshitz, and L.V. Tanatarov. Relaxation between electrons and the crystalline lattice. *Journal of Experimental and Theoretical Physics*, 4:232, 02 1957.
- [34] Sergei Anisimov, B L. Kapeliovich, and T L. Perelman. Electron emission from metal surfaces exposed to ultra-short laser pulses. *Journal of Experimental and Theoretical Physics*, 39:776–781, 07 1974.
- [35] Bernd Huettnner. Short-pulse laser heating of metals: a new approach. In *Proc.SPIE*, 1997.
- [36] J. K. Chen, W. P. Latham, and J. E. Beraun. The role of electronphonon coupling in ultrafast laser heating. *Journal of Laser Applications*, 17(1):63–68, 2005.
- [37] Zijian Li, Si Tan, Elah Bozorg-Grayeli, Takashi Kodama, Mehdi Asheghi, Gil Delgado, Matthew Panzer, Alexander Pokrovsky, Daniel Wack, and Kenneth E Goodson. Phonon dominated heat conduction normal to Mo/Si multilayers with period below 10 nm. *Nano letters*, 12(6):3121–6, June 2012.
- [38] R. A. Treumann. Quantum-statistical mechanics in the lorentzian domain. *EPL (Europhysics Letters)*, 48(1):8, 1999.
- [39] G. Livadiotis and D. J. McComas. Invariant kappa distribution in space plasmas out of equilibrium. *The Astrophysical Journal*, 741(2):88, 2011.

- [40] Dilpuneet S. Aidhy, Chenyang Lu, Ke Jin, Hongbin Bei, Yanwen Zhang, Lumin Wang, and William J. Weber. Point defect evolution in ni, nife and nicr alloys from atomistic simulations and irradiation experiments. *Acta Materialia*, 99:69 – 76, 2015.
- [41] A. Tamm, G. Samolyuk, A. A. Correa, M. Klintonberg, A. Aabloo, and A. Caro. Electron-phonon interaction within classical molecular dynamics. *Phys. Rev. B*, 94:024305, Jul 2016.
- [42] Laurent Karim Bland, German D. Samolyuk, and Roger E. Stoller. Differences in the accumulation of ion-beam damage in ni and nife explained by atomistic simulations. *Journal of Alloys and Compounds*, 662:415 – 420, 2016.
- [43] Eva Zarkadoula, German Samolyuk, and William J. Weber. Two-temperature model in molecular dynamics simulations of cascades in ni-based alloys. *Journal of Alloys and Compounds*, 700:106 – 112, 2017.
- [44] Eva Zarkadoula, German Samolyuk, and William J. Weber. Effects of the electron-phonon coupling activation in collision cascades. *Journal of Nuclear Materials*, 490:317 – 322, 2017.
- [45] Shijun Zhao, Yanwen Zhang, and William J. Weber. Stability of vacancy-type defect clusters in ni based on first-principles and molecular dynamics simulations. *Scripta Materialia*, 145:71 – 75, 2018.
- [46] Aleksi A. Leino, German D. Samolyuk, Ritesh Sachan, Fredric Granberg, William J. Weber, Hongbin Bei, Jie Liu, Pengfei Zhai, and Yanwen Zhang. Gev ion irradiation of nife and nico: Insights from md simulations and experiments. *Acta Materialia*, 151:191 – 200, 2018.
- [47] Alexander A. Balandin, Suchismita Ghosh, Wenzhong Bao, Irene Calizo, Desalegne Teweldebrhan, Feng Miao, and Chun Ning Lau. Superior thermal conductivity of single-layer graphene. *Nano Letters*, 8(3):902–907, 2008.
- [48] Weiwei Cai, Arden L. Moore, Yanwu Zhu, Xuesong Li, Shanshan Chen, Li Shi, and Rodney S. Ruoff. Thermal transport in suspended and supported monolayer graphene grown by chemical vapor deposition. *Nano Letters*, 10(5):1645–1651, 2010.
- [49] Clement Faugeras, Blaise Faugeras, Milan Orlita, M. Potemski, Rahul R. Nair, and A. K. Geim. Thermal conductivity of graphene in corbino membrane geometry. *ACS Nano*, 4(4):1889–1892, 2010.
- [50] Jae-Ung Lee, Duhee Yoon, Hakseong Kim, Sang Wook Lee, and Hyeonsik Cheong. Thermal conductivity of suspended pristine graphene measured by raman spectroscopy. *Phys. Rev. B*, 83:081419, Feb 2011.
- [51] S. Yiğen and A. R. Champagne. Wiedemannfranz relation and thermal-transistor effect in suspended graphene. *Nano Letters*, 14(1):289–293, 2014.
- [52] Feng Hao, Daining Fang, and Zhiping Xu. Mechanical and thermal transport properties of graphene with defects. *Applied Physics Letters*, 99(4):041901, 2011.

- [53] Tianli Feng, Xiulin Ruan, Zhenqiang Ye, and Bingyang Cao. Spectral phonon mean free path and thermal conductivity accumulation in defected graphene: The effects of defect type and concentration. *Phys. Rev. B*, 91:224301, Jun 2015.
- [54] H. Malekpour, P. Ramnani, S. Srinivasan, G. Balasubramanian, D. L. Nika, A. Mulchandani, R. K. Lake, and A. A. Balandin. Thermal conductivity of graphene with defects induced by electron beam irradiation. *Nanoscale*, 8:14608–14616, July 2016.
- [55] Tianli Feng and Xiulin Ruan. Four-phonon scattering reduces intrinsic thermal conductivity of graphene and the contributions from flexural phonons. *Phys. Rev. B*, 97:045202, Jan 2018.
- [56] G. Chen. Thermal conductivity and ballistic-phonon transport in the cross-plane direction of superlattices. *Phys. Rev. B*, 57:14958–14973, Jun 1998.
- [57] C. Dames and G. Chen. Theoretical phonon thermal conductivity of si/ge superlattice nanowires. *Journal of Applied Physics*, 95(2):682–693, 2004.
- [58] Sridhar Sadasivam, Maria K. Y. Chan, and Pierre Darancet. Theory of thermal relaxation of electrons in semiconductors. *Phys. Rev. Lett.*, 119:136602, Sep 2017.
- [59] Zexi Lu, Yan Wang, and Xiulin Ruan. The critical particle size for enhancing thermal conductivity in metal nanoparticle-polymer composites. *Journal of Applied Physics*, 123(7):074302, 2018.
- [60] D M Duffy and a M Rutherford. Including the effects of electronic stopping and electron-ion interactions in radiation damage simulations. *Journal of Physics: Condensed Matter*, 19(1):016207, January 2007.
- [61] Tianli Feng, Wenjun Yao, Zuyuan Wang, Jingjing Shi, Chuang Li, Bingyang Cao, and Xiulin Ruan. Spectral analysis of nonequilibrium molecular dynamics: Spectral phonon temperature and local nonequilibrium in thin films and across interfaces. *Phys. Rev. B*, 95:195202, May 2017.
- [62] David G. Cahill. Heat transport in dielectric thin films and at solid-solid interfaces. *Microscale Thermophysical Engineering*, 1(2):85–109, 1997.
- [63] B.S. Yilbas and S. Bin Mansoor. Phonon and electron transport in aluminum thin film: Influence of film thickness on electron and lattice temperatures. *Physica B: Condensed Matter*, 407(24):4643–4648, December 2012.
- [64] Yan Wang, Zexi Lu, Ajit K. Roy, and Xiulin Ruan. Effect of interlayer on interfacial thermal transport and hot electron cooling in metal-dielectric systems: An electron-phonon coupling perspective. *Journal of Applied Physics*, 119(6), 2016.
- [65] M. L. Roukes, M. R. Freeman, R. S. Germain, R. C. Richardson, and M. B. Ketchen. Hot electrons and energy transport in metals at millikelvin temperatures. *Phys. Rev. Lett.*, 55:422–425, Jul 1985.
- [66] J. Ordonez-Miranda, Ronggui Yang, and J. J. Alvarado-Gil. On the thermal conductivity of particulate nanocomposites. *Applied Physics Letters*, 98(23):233111, 2011.

- [67] J. Ordonez-Miranda, Ronggui Yang, and J. J. Alvarado-Gil. A model for the effective thermal conductivity of metal-nonmetal particulate composites. *Journal of Applied Physics*, 111(4):044319, 2012.
- [68] J. Ordonez-Miranda, J. J. Alvarado-Gil, and Ronggui Yang. Effective Thermal Conductivity of MetalDielectric Composites at the Non-dilute Limit. *International Journal of Thermophysics*, 33(10-11):2118–2124, July 2012.
- [69] J. Ordonez-Miranda, Ronggui Yang, and J. J. Alvarado-Gil. A crowding factor model for the thermal conductivity of particulate composites at non-dilute limit. *Journal of Applied Physics*, 114(6):064306, 2013.
- [70] Patrick E. Hopkins and Pamela M. Norris. Substrate influence in electron-phonon coupling measurements in thin Au films. *Applied Surface Science*, 253(15):6289–6294, May 2007.
- [71] P. E. Hopkins and P. M. Norris. Relative contributions of inelastic and elastic diffuse phonon scattering to thermal boundary conductance across solid interfaces. *Journal of Heat Transfer*, 131(2):–, 2009.
- [72] D. Singh, J. Murthy, and T. Fisher. Effect of phonon dispersion on thermal conduction across si/ge interfaces. In *ASME 2009 InterPACK Conference*, 2009.
- [73] David Mann, Eric Pop, Jien Cao, Qian Wang, and Kenneth and Goodson. Thermally and molecularly stimulated relaxation of hot phonons in suspended carbon nanotubes. *The Journal of Physical Chemistry B*, 110(4):1502–1505, 2006.
- [74] Jesse Maassen and Mark Lundstrom. Modeling ballistic effects in frequency-dependent transient thermal transport using diffusion equations. *Journal of Applied Physics*, 119(9):095102, 2016.
- [75] Meng An, Qichen Song, Xiaoxiang Yu, Han Meng, Dengke Ma, Ruiyang Li, Zelin Jin, Baoling Huang, and Nuo Yang. Generalized two-temperature model for coupled phonons in nanosized graphene. *Nano Letters*, 17(9):5805–5810, 2017.
- [76] D. J. Sanders and D. Walton. Effect of magnon-phonon thermal relaxation on heat transport by magnons. *Phys. Rev. B*, 15:1489–1494, Feb 1977.
- [77] A. J. H. McGaughey and M. Kaviani. Quantitative validation of the boltzmann transport equation phonon thermal conductivity model under the single-mode relaxation time approximation. *Phys. Rev. B*, 69:094303, Mar 2004.
- [78] Dhruv Singh, Jayathi Y. Murthy, and Timothy S. Fisher. Spectral phonon conduction and dominant scattering pathways in graphene. *Journal of Applied Physics*, 110(9):094312, 2011.
- [79] Dhruv Singh, Jayathi Y. Murthy, and Timothy S. Fisher. Mechanism of thermal conductivity reduction in few-layer graphene. *Journal of Applied Physics*, 110(4):044317, 2011.
- [80] Shijun Zhao, William J. Weber, and Yanwen Zhang. Unique challenges for modeling defect dynamics in concentrated solid-solution alloys. *JOM*, 69(11):2084–2091, Nov 2017.

- [81] Florian Mller-Plathe. A simple nonequilibrium molecular dynamics method for calculating the thermal conductivity. *The Journal of Chemical Physics*, 106(14):6082–6085, 1997.
- [82] Patrick K. Schelling, Simon R. Phillpot, and Pawel Keblinski. Comparison of atomic-level simulation methods for computing thermal conductivity. *Phys. Rev. B*, 65:144306, Apr 2002.
- [83] Robert J. Stevens, Leonid V. Zhigilei, and Pamela M. Norris. Effects of temperature and disorder on thermal boundary conductance at solidsolid interfaces: Nonequilibrium molecular dynamics simulations. *International Journal of Heat and Mass Transfer*, 50(1920):3977 – 3989, 2007.
- [84] E. S. Landry and A. J. H. McGaughey. Thermal boundary resistance predictions from molecular dynamics simulations and theoretical calculations. *Phys. Rev. B*, 80:165304, Oct 2009.
- [85] R. Car and M. Parrinello. Unified approach for molecular dynamics and density-functional theory. *Phys. Rev. Lett.*, 55:2471–2474, Nov 1985.
- [86] D M Duffy and A M Rutherford. Including the effects of electronic stopping and electronion interactions in radiation damage simulations. *Journal of Physics: Condensed Matter*, 19(1):016207, 2007.
- [87] A. A. Joshi and A. Majumdar. Transient ballistic and diffusive phonon heat transport in thin films. *Journal of Applied Physics*, 74(1):31–39, 1993.
- [88] A Majumdar. Microscale heat conduction in lelectnc thin films. *Journal of Heat Transfer*, 115(February 1993):7–16, 1993.
- [89] G Chen. Size and interface effects on thermal conductivity of superlattice and periodic thin-film structures. *Journal of Heat Transfer*, 119:220–229, 05 1997.
- [90] J. Kaiser, T. Feng, J. Maassen, X. Wang, X. Ruan, and M. Lundstrom. Thermal transport at the nanoscale: A fourier’s law vs. phonon boltzmann equation study. *Journal of Applied Physics*, 121(4):044302, 2017.
- [91] Rodrigo Escobar, Brian Smith, and Cristina Amon. Lattice Boltzmann Modeling of Subcontinuum Energy Transport in Crystalline and Amorphous Micro-electronic Devices. *Journal of Electronic Packaging*, 128(2):115, 2006.
- [92] Rodrigo A Escobar and Cristina H Amon. Time-dependent simulations of sub-continuum heat generation effects in electronic devices using the lattice boltzmann method. *Proceeding of ASME 2003 International Mechanical Engineering Congress and Exposition*, 2003.
- [93] Escobar Rodrigo A. and Amon Cristina H. Thin film phonon heat conduction by the dispersion lattice boltzmann method. *Journal of Heat Transfer*, 130:220–229, 09 2008.
- [94] J. M. Ziman. *Electrons and Phonons*. Oxford University Press, 1960.
- [95] Andreas Mortensen and Javier Llorca. Metal Matrix Composites. *Annual Review of Materials Research*, 40(1):243–270, June 2010.

- [96] G. W. Milton. *The Theory of Composites* (Cambridge University Press, Cambridge, UK, 2002). 2002.
- [97] Joanna Aizenberg, Andrew J. Black, and George M. Whitesides. Oriented growth of calcite controlled by self-assembled monolayers of functionalized alkanethiols supported on gold and silver. *Journal of the American Chemical Society*, 121(18):4500–4509, 1999.
- [98] I.-H. Sung and D.-E. Kim. Molecular dynamics simulation study of the nano-wear characteristics of alkanethiol self-assembled monolayers. *Applied Physics A*, 81(1):109–114, 2005.
- [99] Tengfei Luo and John R. Lloyd. Non-equilibrium molecular dynamics study of thermal energy transport in AuSAMAu junctions. *International Journal of Heat and Mass Transfer*, 53(1-3):1–11, January 2010.
- [100] Zhaohui Wang, David G. Cahill, Jeffrey A. Carter, Yee Kan Koh, Alexei Lagutchev, Nak-Hyun Seong, and Dana D. Dlott. Ultrafast dynamics of heat flow across molecules. *Chemical Physics*, 350(13):31 – 44, 2008. Femtochemistry and Femtobiology Papers associated with the 8th International Conference on Femtochemistry and Femtobiology.
- [101] Tengfei Luo and John R. Lloyd. Equilibrium molecular dynamics study of lattice thermal conductivity/conductance of au-sam-au junctions. *Journal of Heat Transfer*, 132(3):–, 2009.
- [102] T. Meier, F. Menges, P. Nirmalraj, H. Hölscher, H. Riel, and B. Gotsmann. Length-dependent thermal transport along molecular chains. *Phys. Rev. Lett.*, 113:060801, Aug 2014.
- [103] Eric S. Toberer, Lauryn L. Baranowski, and Chris Dames. Advances in Thermal Conductivity. *Annual Review of Materials Research*, 42(1):179–209, August 2012.
- [104] Ronggui Yang and Gang Chen. Thermal conductivity modeling of periodic two-dimensional nanocomposites. *Physical Review B*, 69(19):195316, May 2004.
- [105] Xi Shen, Zhenyu Wang, Ying Wu, Xu Liu, Yan-Bing He, and Jang-Kyo Kim. Multilayer graphene enables higher efficiency in improving thermal conductivities of graphene/epoxy composites. *Nano Letters*, 16(6):3585–3593, 2016.
- [106] Khan M. F. Shahil and Alexander A. Balandin. Graphene multilayer graphene nanocomposites as highly efficient thermal interface materials. *Nano Letters*, 12(2):861–867, 2012.
- [107] Matt Law, Joshua Goldberger, and Peidong Yang. Semiconductor Nanowires and Nanotubes. *Annual Review of Materials Research*, 34(1):83–122, August 2004.
- [108] J. C. Maxwell. *Electricity and Magnetism* (Clarendon Press, Oxford, 1873). 1873.
- [109] A. N. Norris, P. Sheng, and A. J. Callegari. Effective-medium theories for two-phase dielectric media. *Journal of Applied Physics*, 57(6):1990, 1985.

- [110] Hiroshi Hatta and Minoru Taya. Thermal conductivity of coated filler composites. *Journal of Applied Physics*, 59(6):1851, 1986.
- [111] Y. Benveniste. Effective thermal conductivity of composites with a thermal contact resistance between the constituents: Nondilute case. *Journal of Applied Physics*, 61(8):2840, 1987.
- [112] Y. Benveniste and T. Miloh. On the effective thermal conductivity of coated short-fiber composites. *Journal of Applied Physics*, 69(3):1337, 1991.
- [113] D.P.H. Hasselman and L. F. Johnson. Effective Thermal Conductivity of Composites with Interfacial Thermal Barrier Resistance. *Journal of Composite Materials*, 21(6):508–515, January 1987.
- [114] A.G. Every, Y. Tzou, D.P.H. Hasselman, and R. Raj. The effect of particle size on the thermal conductivity of ZnS/diamond composites. *Acta Metallurgica et Materialia*, 40(1):123–129, January 1992.
- [115] Ce-Wen Nan, R. Birringer, David R. Clarke, and H. Gleiter. Effective thermal conductivity of particulate composites with interfacial thermal resistance. *Journal of Applied Physics*, 81(10):6692, 1997.
- [116] H. Duan, B. Karihaloo, J. Wang, and X. Yi. Compatible composition profiles and critical sizes of alloyed quantum dots. *Physical Review B*, 74(19):195328, November 2006.
- [117] H. Duan and B. Karihaloo. Effective thermal conductivities of heterogeneous media containing multiple imperfectly bonded inclusions. *Physical Review B*, 75(6):064206, February 2007.
- [118] Ronggui Yang, Gang Chen, and Mildred Dresselhaus. Thermal conductivity of simple and tubular nanowire composites in the longitudinal direction. *Physical Review B*, 72(12):125418, September 2005.
- [119] Weixue Tian and Ronggui Yang. Thermal conductivity modeling of compacted nanowire composites. *Journal of Applied Physics*, 101(5):054320, 2007.
- [120] Weixue Tian and Ronggui Yang. Effect of interface scattering on phonon thermal conductivity percolation in random nanowire composites. *Applied Physics Letters*, 90(26):263105, 2007.
- [121] Ravi Prasher. Thermal conductivity of composites of aligned nanoscale and microscale wires and pores. *Journal of Applied Physics*, 100(3):034307, 2006.
- [122] Austin Minnich and Gang Chen. Modified effective medium formulation for the thermal conductivity of nanocomposites. *Applied Physics Letters*, 91(7):073105, 2007.
- [123] E. S. Landry and a. J. H. McGaughey. Effect of film thickness on the thermal resistance of confined semiconductor thin films. *Journal of Applied Physics*, 107(1):013521, 2010.
- [124] A. J. Minnich, G. Chen, S. Mansoor, and B. S. Yilbas. Quasiballistic heat transfer studied using the frequency-dependent boltzmann transport equation. *Phys. Rev. B*, 84:235207, Dec 2011.

- [125] Mark D. Losego, Martha E. Grady, Nancy R. Sottos, David G. Cahill, and Paul V. Braun. Effects of chemical bonding on heat transport across interfaces. *Nature Materials*, 11, 2012.
- [126] Robert Y. Wang, Rachel A. Segalman, and Arun Majumdar. Room temperature thermal conductance of alkanedithiol self-assembled monolayers. *Applied Physics Letters*, 89(17):173113, 2006.
- [127] Dvira Segal, Abraham Nitzan, and Peter Hanggi. Thermal conductance through molecular wires. *The Journal of Chemical Physics*, 119(13):6840, 2003.
- [128] Asegun Henry and Gang Chen. High Thermal Conductivity of Single Polyethylene Chains Using Molecular Dynamics Simulations. *Physical Review Letters*, 101(23):235502, December 2008.
- [129] Zhibin Lin, Leonid V. Zhigilei, and Vittorio Celli. Electron-phonon coupling and electron heat capacity of metals under conditions of strong electron-phonon nonequilibrium. *Phys. Rev. B*, 77:075133, Feb 2008.
- [130] John C Duda, Christopher B Saltonstall, Pamela M Norris, and Patrick E Hopkins. Assessment and prediction of thermal transport at solid-self-assembled monolayer junctions. *The Journal of chemical physics*, 134(9):094704, March 2011.
- [131] Aydin Nabovati, Daniel P. Sellan, and Cristina H. Amon. On the lattice Boltzmann method for phonon transport. *Journal of Computational Physics*, 230(15):5864–5876, July 2011.
- [132] Xuewang Wu, Jeff Walter, Tianli Feng, Jie Zhu, Hong Zheng, John F. Mitchell, Neven Bikup, Maria Varela, Xiulin Ruan, Chris Leighton, and Xiaojia Wang. Glass-like through-plane thermal conductivity induced by oxygen vacancies in nanoscale epitaxial $\text{La}_{0.5}\text{Sr}_{0.5}\text{CoO}_3$. *Advanced Functional Materials*, 2017.
- [133] T Zeng and G Chen. Nonequilibrium phonon and electron transport in heterostructures and superlattices. *Microscale Thermophysical Engineering*, 5(2):71–88, 2001.
- [134] A. Bulusu and D. G. Walker. One-dimensional thin-film phonon transport with generation. *Microelectronics Journal*, 39, Dec 2008.
- [135] L. Koči, E. Bringa, D. Ivanov, J. Hawreliak, J. McNaney, a. Higginbotham, L. Zhigilei, a. Belonoshko, B. Remington, and R. Ahuja. Simulation of shock-induced melting of Ni using molecular dynamics coupled to a two-temperature model. *Physical Review B*, 74(1):012101, July 2006.
- [136] Sridhar Sadasivam, Umesh V. Waghmare, and Timothy S. Fisher. Electron-phonon coupling and thermal conductance at a metal-semiconductor interface: First-principles analysis. *Journal of Applied Physics*, 117(13):134502, April 2015.
- [137] A. Sergeev. Electronic Kapitza conductance due to inelastic electron-boundary scattering. *Physical Review B*, 58(16):R10199–R10202, October 1998.
- [138] A Sergeev. Inelastic electronboundary scattering in thin films. *Physica B: Condensed Matter*, 263-264:217–219, March 1999.

- [139] Liang Guo, Stephen L. Hodson, Timothy S. Fisher, and Xianfan Xu. Heat Transfer Across Metal-Dielectric Interfaces During Ultrafast-Laser Heating. *Journal of Heat Transfer*, 134(4):042402, 2012.
- [140] N Driza, S Blanco-Canosa, M Bakr, S Soltan, M Khalid, L Mustafa, K Kawashima, G Christiani, H-U Habermeier, G Khaliullin, C Ulrich, M Le Tacon, and B Keimer. Long-range transfer of electron-phonon coupling in oxide superlattices. *Nature materials*, 11(8):675–81, August 2012.
- [141] Reese E Jones, Jeremy A Templeton, Gregory J Wagner, David Olmsted, and Nomand A Modine. Electron transport enhanced molecular dynamics for metals and semi-metals . *International Journal for Numerical Methods in Engineering*, (March):940–967, 2010.
- [142] Seungha Shin, Massoud Kaviany, Tapan Desai, and Richard Bonner. Roles of atomic restructuring in interfacial phonon transport. *Physical Review B*, 82(8):081302, August 2010.
- [143] Jingjing Shi, Yalin Dong, Timothy Fisher, and Xiulin Ruan. Thermal transport across carbon nanotube-graphene covalent and van der waals junctions. *Journal of Applied Physics*, 118(4):–, 2015.
- [144] J. Tersoff. New empirical approach for the structure and energy of covalent systems. *Phys. Rev. B*, 37:6991–7000, Apr 1988.
- [145] S. M. Foiles, M. I. Baskes, and M. S. Daw. Embedded-atom-method functions for the fcc metals cu, ag, au, ni, pd, pt, and their alloys. *Phys. Rev. B*, 33:7983–7991, Jun 1986.
- [146] Shun-Fa Hwang, Yi-Hung Li, and Zheng-Han Hong. Molecular dynamic simulation for Cu cluster deposition on Si substrate. *Computational Materials Science*, 56:85–94, April 2012.
- [147] Shuichi Nose. A unified formulation of the constant temperature molecular dynamics methods. *The Journal of Chemical Physics*, 81(1):511, 1984.
- [148] G. L. Eesley. Generation of nonequilibrium electron and lattice temperatures in copper by picosecond laser pulses. *Phys. Rev. B*, 33:2144–2151, Feb 1986.
- [149] Eric Pop, Robert W. Dutton, and Kenneth E. Goodson. Analytic band Monte Carlo model for electron transport in Si including acoustic and optical phonon dispersion. *Journal of Applied Physics*, 96(9):4998, 2004.
- [150] Tianli Feng and Xiulin Ruan. Prediction of Spectral Phonon Mean Free Path and Thermal Conductivity with Applications to Thermoelectrics and Thermal Management: A Review. *Journal of Nanomaterials*, 2014:1–25, 2014.
- [151] Philip B. Allen. Theory of thermal relaxation of electrons in metals. *Phys. Rev. Lett.*, 59:1460–1463, Sep 1987.
- [152] Tue Gunst, Troels Markussen, Kurt Stokbro, and Mads Brandbyge. First-principles method for electron-phonon coupling and electron mobility: Applications to two-dimensional materials. *Phys. Rev. B*, 93:035414, Jan 2016.

- [153] Feliciano Giustino. Electron-phonon interactions from first principles. *Rev. Mod. Phys.*, 89:015003, Feb 2017.
- [154] M. Hengsberger, D. Purdie, P. Segovia, M. Garnier, and Y. Baer. Photoemission Study of a Strongly Coupled Electron-Phonon System. *Physical Review Letters*, 83(0001):592–595, 1999.
- [155] D.-A. Luh, T. Miller, J. J. Paggel, and T.-C. Chiang. Large electron-phonon coupling at an interface. *Phys. Rev. Lett.*, 88:256802, Jun 2002.
- [156] Patrick E. Hopkins. Thermorefectance dependence on fermi surface electron number density perturbations. *Applied Physics Letters*, 96(4):041901, 2010.
- [157] Pengfei Ji and Yuwen Zhang. Ab initio determination of effective electron-phonon coupling factor in copper. *Physics Letters A*, 380(17):1551–1555, 2016.
- [158] F. Marsiglio and J. P. Carbotte. *Electron-Phonon Superconductivity*, pages 73–162. Springer Berlin Heidelberg, Berlin, Heidelberg, 2008.
- [159] J. P. Perdew and Alex Zunger. Self-interaction correction to density-functional approximations for many-electron systems. *Phys. Rev. B*, 23:5048–5079, May 1981.
- [160] Yan Wang, Zexi Lu, and Xiulin Ruan. First principles calculation of lattice thermal conductivity of metals considering phonon-phonon and phonon-electron scattering. *Journal of Applied Physics*, 119(22):225109, 2016.
- [161] Jiawei Zhou, Hangtian Zhu, Te-Huan Liu, Qichen Song, Ran He, Jun Mao, Zihang Liu, Wuyang Ren, Bolin Liao, David J. Singh, Zhifeng Ren, and Gang Chen. Large thermoelectric power factor from crystal symmetry-protected non-bonding orbital in half-heuslers. *Nature Communications*, 9(1721), Apr 2018.
- [162] S.-S. Wellershoff, J. Hohlfeld, J. GÜdde, and E. Matthias. The role of electron-phonon coupling in femtosecond laser damage of metals. *Applied Physics A*, 69(1):S99–S107, Dec 1999.
- [163] Lan Jiang and Hai-Lung Tsai. Improved two-temperature model and its application in ultrashort laser heating of metal films. *Journal of Heat Transfer*, 127(10):1167–1173, Jun 2005.
- [164] Jin-Wu Jiang and Jian-Sheng Wang. Joule heating and thermoelectric properties in short single-walled carbon nanotubes: Electron-phonon interaction effect. *Journal of Applied Physics*, 110(12):124319, 2011.
- [165] Ankit Jain and Alan J. H. McGaughey. Thermal transport by phonons and electrons in aluminum, silver, and gold from first principles. *Phys. Rev. B*, 93:081206, Feb 2016.
- [166] Te-Huan Liu, Jiawei Zhou, Bolin Liao, David J. Singh, and Gang Chen. First-principles mode-by-mode analysis for electron-phonon scattering channels and mean free path spectra in gaas. *Phys. Rev. B*, 95:075206, Feb 2017.
- [167] Stefano Baroni, Stefano de Gironcoli, Andrea Dal Corso, and Paolo Giannozzi. Phonons and related crystal properties from density-functional perturbation theory. *Rev. Mod. Phys.*, 73:515–562, Jul 2001.

- [168] Gui Qin Huang. Electronic structures, surface phonons, and electron-phonon interactions of Al(100) and Al(111) thin films from density functional perturbation theory. *Physical Review B*, 78(21):214514, December 2008.
- [169] Paolo Giannozzi, Stefano Baroni, Nicola Bonini, Matteo Calandra, Roberto Car, Carlo Cavazzoni, Davide Ceresoli, Guido L Chiarotti, Matteo Cococcioni, Ismaila Dabo, Andrea Dal Corso, Stefano de Gironcoli, Stefano Fabris, Guido Fratesi, Ralph Gebauer, Uwe Gerstmann, Christos Gougoussis, Anton Kokalj, Michele Lazzeri, Layla Martin-Samos, Nicola Marzari, Francesco Mauri, Riccardo Mazzarello, Stefano Paolini, Alfredo Pasquarello, Lorenzo Paulatto, Carlo Sbraccia, Sandro Scandolo, Gabriele Sclauzero, Ari P Seitsonen, Alexander Smogunov, Paolo Umari, and Renata M Wentzcovitch. Quantum espresso: a modular and open-source software project for quantum simulations of materials. *Journal of Physics: Condensed Matter*, 21(39):395502, 2009.
- [170] M. Methfessel and A. T. Paxton. High-precision sampling for brillouin-zone integration in metals. *Phys. Rev. B*, 40:3616–3621, Aug 1989.
- [171] Jesse Noffsinger, Feliciano Giustino, Brad D. Malone, Cheol-Hwan Park, Steven G. Louie, and Marvin L. Cohen. Epw: A program for calculating the electronphonon coupling using maximally localized wannier functions. *Computer Physics Communications*, 181(12):2140 – 2148, 2010.
- [172] Z. Tang and N. Aluru. Calculation of thermodynamic and mechanical properties of silicon nanostructures using the local phonon density of states. *Physical Review B*, 74(23):235441, 2006.
- [173] X. Y. Wang, D. M. Riffe, Y.-S. Lee, and M. C. Downer. Time-resolved electron-temperature measurement in a highly excited gold target using femtosecond thermionic emission. *Phys. Rev. B*, 50:8016–8019, Sep 1994.
- [174] Ruxandra M. Costescu, Marcel A. Wall, and David G. Cahill. Thermal conductance of epitaxial interfaces. *Phys. Rev. B*, 67:054302, Feb 2003.
- [175] Anshu Pandey and Philippe Guyot-Sionnest. Slow electron cooling in colloidal quantum dots. *Science*, 322(5903):929–932, 2008.
- [176] Jun Zhou, Nianbei Li, and Ronggui Yang. An electrohydrodynamics model for non-equilibrium electron and phonon transport in metal films after ultra-short pulse laser heating. *The European Physical Journal B*, 88(6):156, Jun 2015.
- [177] Eric Pop, Vikas Varshney, and Ajit K. Roy. Thermal properties of graphene: Fundamentals and applications. *MRS Bulletin*, 37(12):12731281, 2012.
- [178] Yan Wang, Ajit K. Vallabhaneni, Bo Qiu, and Xiulin Ruan. Two-dimensional thermal transport in graphene: A review of numerical modeling studies. *Nanoscale and Microscale Thermophysical Engineering*, 18(2):155–182, 2014.
- [179] Jingjing Shi, Yang Zhong, Timothy S. Fisher, and Xiulin Ruan. Decomposition of the thermal boundary resistance across carbon nanotubegraphene junctions to different mechanisms. *ACS Applied Materials & Interfaces*, 10(17):15226–15231, 2018.

- [180] Zhun-Yong Ong, Bo Qiu, Shanglong Xu, Xiulin Ruan, and Eric Pop. Flexural resonance mechanism of thermal transport across graphene-sio2 interfaces. *Journal of Applied Physics*, 123(11):115107, 2018.
- [181] Yujie Wei and Ronggui Yang. Nanomechanics of graphene. *National Science Review*, page nwy067, 2018.
- [182] Wonjun Park, Jiuning Hu, Luis A. Jauregui, Xiulin Ruan, and Yong P. Chen. Electrical and thermal conductivities of reduced graphene oxide/polystyrene composites. *Applied Physics Letters*, 104(11):113101, 2014.
- [183] Xufei Wu, Vikas Varshney, Jonghoon Lee, Teng Zhang, Jennifer L. Wohlwend, Ajit K. Roy, and Tengfei Luo. Hydrogenation of penta-graphene leads to unexpected large improvement in thermal conductivity. *Nano Letters*, 16(6):3925–3935, 2016.
- [184] Zhuonan Lin, Wei Qin, Jiang Zeng, Wei Chen, Ping Cui, Jun-Hyung Cho, Zhenhua Qiao, and Zhenyu Zhang. Competing gap opening mechanisms of monolayer graphene and graphene nanoribbons on strong topological insulators. *Nano Letters*, 17(7):4013–4018, 2017.
- [185] Ke Xu, Hao Lu, Erich W. Kinder, Alan Seabaugh, and Susan K. Fullerton-Shirey. Monolayer solid-state electrolyte for electric double layer gating of graphene field-effect transistors. *ACS Nano*, 11(6):5453–5464, 2017.
- [186] Jingjing Shi, Jonghoon Lee, Yalin Dong, Ajit Roy, Timothy S. Fisher, and Xiulin Ruan. Dominant phonon polarization conversion across dimensionally mismatched interfaces: Carbon-nanotube-graphene junction. *Phys. Rev. B*, 97:134309, Apr 2018.
- [187] Chun Hung Lui, Kin Fai Mak, Jie Shan, and Tony F. Heinz. Ultrafast photoluminescence from graphene. *Phys. Rev. Lett.*, 105:127404, Sep 2010.
- [188] Yee Kan Koh, Myung-Ho Bae, David G. Cahill, and Eric Pop. Heat conduction across monolayer and few-layer graphenes. *Nano Letters*, 10(11):4363–4368, 2010.
- [189] Arthur J Nozik. Spectroscopy and hot electron relaxation dynamics in semiconductor quantum wells and quantum dots. *Annual Review of Physical Chemistry*, 52(1):193–231, 2001.
- [190] Liangliang Chen, Hua Bao, Taizhi Tan, Oleg V. Prezhdo, and Xiulin Ruan. Shape and temperature dependence of hot carrier relaxation dynamics in spherical and elongated cdse quantum dots. *The Journal of Physical Chemistry C*, 115(23):11400–11406, 2011.

VITA

VITA

Zexi Lu was born in Shenyang, Liaoning Province, China in 1989. He obtained his Bachelor of Science degree in Engineering in 2012 from Department of Precision Instruments and Measurement at Tsinghua University in Beijing, China. He then moved on to pursue his direct-PhD degree in Department of Mechanical Engineering at Purdue University, West Lafayette, Indiana, USA. He joined the Nanoscale Energy Transport and Conversion Laboratory directed by Prof. Xiulin Ruan in 2012. He expects to be granted his Doctor of Philosophy degree from School of Engineering at Purdue University by December 2018.